CENTER FOR PHYSICAL SCIENCES AND TECHNOLOGY
VILNIUS UNIVERSITY

Simonas Indrišiūnas

FORMATION OF LIGHT HARVESTING STRUCTURES FOR PHOTOVOLTAICS USING LASER INTERFERENCE ABLATION

Doctoral dissertation
Technological Sciences, Materials Engineering (08T)

Vilnius, 2018

The research was performed in 2013-2017 in the Department of Laser Technologies of the Center for Physical Sciences and Technology.

Scientific supervisor:

Dr. Gediminas Račiukaitis (Center for Physical Sciences and Technology, Technological Sciences, Material Engineering – 08T).

FIZINIŲ IR TECHNOLOGIJOS MOKSLŲ CENTRAS
VILNIAUS UNIVERSITETAS

Simonas Indrišiūnas

ŠVIESOS PAGAVIMO STRUKTŪRŲ FORMAVIMAS FOTOVOLTINIAMS ELEMENTAMS, NAUDOJANT LAZERINĘ INTERFERENCINĘ ABLIACIJĄ

Daktaro disertacija
Technologijos mokslai, Medžiagų inžinerija (08T)

Vilnius, 2018

Disertacija rengta 2013-2017 metais valstybinio mokslinių tyrimų instituto Fizinių ir technologijos mokslų centro Lazerinių technologijų skyriuje.

Mokslinis vadovas:

Dr. Gediminas Račiukaitis (Fizinių ir technologijos mokslų centras, technologijos mokslai, medžiagų inžinerija - 08T).

Table of Contents

Acknowledgements

I am grateful for my scientific supervisor Dr. G. Račiukaitis for his support and advice.

Thanks to my colleagues Dr. Mindaugas Gedvilas and Dr. Evaldas Stankevičius and, especially, to Dr. Bogdan Voisiat for advice and valuable discussions.

Thanks to Dr. A. Pūgžlys, Prof. A. Baltuška and their group at Photonic Institute of Vienna University for access to their equipment.

Thanks to Dr. V.Strazdienė, Dr. A. Rėza, Dr. A. Selskis, Dr. M. Gavutis, Dr. T. Rakickas, A. Žukauskas and other colleagues from FTMC for their help in particular part of the experiments.

I also express my thanks to Dr. P. Gečys, Dr. R. Trusovas, Dr. V. Stankevič, E. Markauskas, K. Ratautas, J. Dudutis, A. Žemaitis, E. Daugnoraitė and other colleagues from the Department of Laser Technologies for a friendly atmosphere in the laboratory.

Part of this work was supported by the Research Council of Lithuania under the project ATE-11/2012 and EUROSTARS 2 programme under the project SLAM-HELP (E!10217 SLAM-HELP).

List of Abbreviations

List of acronyms

AFM	Atomic Force Microscope
a-Si:H	Hydrogenated amorphous silicon
μc-Si:H	Microcrystalline hydrogenated silicon
a. u.	arbitrary units
DOE	Diffractive Optical Element
DLIP	Direct Laser Interference Patterning
EDS	Energy-dispersive X-ray spectroscopy
FF	Fill Factor
FROG	Frequency-Resolved Optical Gating
HIT	Heterojunction with an Intrinsic Thin layer
PECVD	Plasma Enhanced Chemical Vapour Deposition
PERC	Passivated Emitter and Rear Cells
PERL	Passivated Emitter and Rear Local diffusion
PV	Photovoltaic
RIE	Reactive Ion Etching
SEM	Scanning Electron Microscope
SPP	Surface Plasmon Polariton

List of symbols

C_p	specific heat capacity
$\mathbf{E}$	electric field vector
E_p	laser pulse energy
F_0	peak fluence
G	generation rate
I_{SC}	short-circuit current
I	radiation intensity
i	integer denoting SPP resonance mode

j	integer denoting SPP resonance mode
J	current density
J_{SC}	short-circuit current density
J_0	dark saturation current density
k	Boltzmann's constant
k	wave vector
L_{th}	thermal penetration depth
L_m	the latent heat of melting
L_v	the latent heat of vaporisation
N	number of the interfering beams
n	refractive index
P_{max}	maximum power
Q	absorbed laser power per unit volume
q	electron charge
r	radius vector
R_λ	reflectivity
T	temperature
T_v	boiling temperature
t	time
V	voltage
V_{OC}	open circuit voltage
w_0	laser beam spot radius
x_C^{RS}	crystalline silicon fraction

List of Greek symbols

α absorption coefficient

γ angle between the projection of the electric field vector **E** to the XY-plane and the x-direction of the coordinate system

Δ_m temperature parameter

Δ_v temperature parameter

ε_d dielectric relative permittivity

ε_m metal relative permittivity

η solar cell energy conversion efficiency

Θ_2 half-angle between laser beams

κ thermal conductivity

Λ pattern period

ξ angle between the projections of the **k** and **E** vectors in the XY-plane

ρ material density

τ_p laser pulse duration

φ phase of the electromagnetic wave

ϖ angular frequency of the electromagnetic wave

1 Introduction

One of the challenges in the photovoltaic technology is to become competitive with other, traditional, energy sources. The attractiveness of the solar energy to customers can be increased by efficiency improvement and cost reduction of the solar cells. Light harvesting plays an essential role in further progress to the high-efficient solar cells. Light harvesting structures are needed to increase part of the light reaching the photovoltaic element that is absorbed in its active layer. This is achieved by reducing light reflection from the front side of the element and increasing the distance, which light travels inside the element to be absorbed.

In the currently most commercially successful silicon solar cells, light harvesting is achieved using antireflective front surface layers and wet chemical etching to form surface structures. There are many other possible approaches described in the scientific literature, including patterning of the front contact or passivation layer [1-3], fabrication of the plasmonic structures [4, 5], texturing of the substrate of the thin film photovoltaic cell [6].

Fast and cost-effective fabrication of such structures has to be considered. Laser micro-fabrication is among the considered fabrication methods due to no need for consumable materials, masks or moulds and high patterning flexibility. However, fast fabrication of micrometre-size structures is a challenge. The solution is to use some kind of parallel processing. One of the parallel processing methods is the direct laser beam interference patterning (DLIP) technique. DLIP utilises several interfering laser beams to obtain a spatially-modulated intensity distribution [7, 8]. Irradiation with interference pattern allows direct ablation of periodical structures with sub-wavelength features. DLIP offers fabrication speed advantage over the conventional single-beam direct laser writing.

Silicon remains the main material used in the solar cell production, because of its low cost, abundance in nature and well-established processing technologies. In this work, DLIP technique was tested for the fabrication of various light harvesting textures for the silicon solar cells. In the first part of this thesis (Chapter 4), the formation of the texture in the passivating antireflective silicon nitride layer is discussed. In Chapters 5 and 6, fabrication of surface textures in silicon using DLIP and wet chemical etching is presented. Chapter 7 is dedicated to the DLIP fabrication of plasmonic metal structures. A large part of this chapter is committed to the improvements of the DLIP method. New means to achieve uniform large-area patterning and increase the flexibility of the DLIP patterning are presented.

1.1 The aim of the research

1. To investigate the feasibility of DLIP patterning of the antireflective layer of the complete silicon solar cell as a tool to improve solar cell performance.
2. To find optimal laser fabrication parameters for manufacturing of periodical surface textures in monocrystalline and multicrystalline silicon wafers using DLIP technique and to investigate antireflective/light trapping function of these textures.
3. To improve DLIP patterning apparatus for better fulfilment of the industrial requirements.

1.2 Practical value and novelty

1.2.1 The novelty of the thesis

1. Spatially-selective conversion of the silicon nitride thin film to the SiO_xN_y under the 4-beam DLIP patterning was demonstrated. The periodical grating of SiO_xN_y in the antireflective silicon nitride layer of

the silicon solar cell was formed, and its impact on the optical and photo-electrical characteristics of the solar cell was investigated.

2. Effect of the silicon oxide layer, formed due to the irradiation with the interference intensity distribution, to the fabrication of inverted pyramid pattern in crystalline silicon, using DLIP patterning and anisotropic wet chemical etching was evaluated.
3. Motorised optical setup for the polarisation control of the each of the interfering beams was created. Effect of the angle between the interfering beams on the interference pattern, produced using beam polarisation control in the interference setup, was investigated.

1.2.2 The practical value of this thesis

1. An optimal laser fabrication condition for fabrication of antireflective texture on multicrystalline silicon wafers by DLIP was found. Such process can be used to improve the performance of the multicrystalline silicon solar cells.
2. Influence of a laser formed an oxide layer in the fabrication of inverted pyramid pattern by combined DLIP, and anisotropic wet chemical etching process was assessed. This fabrication method can be used to simplify anisotropic silicon texturing process.
3. Improvements to the DLIP technique (an increase of the uniform patterning area and control of the structure shape) can be adapted to build the commercial DLIP patterning machine.

1.3 Statements to defend

1. Passivating and antireflective silicon nitride layer on silicon can be locally converted to SiN_xO_y by irradiating it with the interference-modulated laser beam when fluence in the intensity maxima is below the ablation threshold. Such process results in the

formation of periodical refractive index grating in the antireflective silicon nitride layer diffracting solar light.

2. DLIP patterning of silicon in ambient air results in the formation of the silicon oxide layer between the intensity maxima. Such layer acts as an etching mask for the anisotropic wet chemical etching process and can be utilised in the fabrication of the inverted pyramid pattern in monocrystalline silicon.
3. Periodical dimple array fabricated in the multicrystalline silicon using DLIP with the sub-nanosecond laser pulses, and wet chemical etching provides the best antireflective properties in the visible and near-infrared spectrum when the period of the structure is larger than one micrometre. Further reduction of the pattern period results in a shallow or irregular texture due to the melt formation and flow.
4. When the angle between the intersecting beams becomes sufficiently large (larger than 13°), the vertical component of an electric field should be taken into account. The presence of the vertical electric field component results in the modifications in the interference patterns when the angle between the intersecting beams (pattern period) is varied.

1.4 Approbation

Results of the research presented in this thesis were published in 5 peer-reviewed scientific papers [A1-A5] and, together with co-authors, were presented in 13 contributions to conferences [C1-C13]. 10 of the contributions were presented personally by the author.

1.4.1 Scientific papers

Related to the topic of this thesis (ISI WoS – with Conference Proceedings)

[A1] A. Vinčiūnas, **S. Indrišiūnas**, B. Voisiat, G. Račiukaitis, I. Šimkienė, R. Suzanovičienė, A. Rėza and R. Mažeikienė, Effect of Laser Patterning on Properties of Crystalline Si Photovoltaic Cells and Substrates. *J. Laser Micro/Nanoeng* 8(3), 244-252 (2013).

[A2] B. Voisiat, **S. Indrišiūnas**, G. Račiukaitis, I. Šimkienė, A. Rėza and R. Suzanovičienė, Application of Laser Texturing in Silicon Solar Cell Technology. *Matter. Sci. (Medžiagotyra)* **20**(2), 157-159 (2014).

[A3] S. Indrišiūnas, B. Voisiat, A. Rėza, I. Šimkienė, R. Mažeikienė, A. Selskis and G. Račiukaitis, Effect of laser-induced conversion of silicon nitride to silicon oxy-nitride on antireflective properties of the passivation layer in polysilicon solar cells. *Opt. Mater. Express* **5**, 1532-1542 (2015).

[A4] S. Indrišiūnas, B. Voisiat, M. Gedvilas and G. Račiukaitis, New opportunities for custom-shape patterning using polarisation control in confocal laser beam interference setup. *J. Laser Appl*. **29**, 011501 (2017).

[A5] M. Gedvilas, **S. Indrisiunas**, B. Voisiat, E. Stankevicius, A. Selskis, G. Raciukaitis, Nanoscale thermal diffusion during the laser interference ablation using femto-, pico-, and nanosecond pulses in silicon. Phys. Chem. Chem. Phys **20**(17), 12166-12174 (2018).

[A6] S. Indrisiunas, B. Voisiat, A. Žukauskas and G. Račiukaitis, Direct laser beam interference patterning technique for fast high aspect ratio surface structuring. *Proc. SPIE* **9350**, 935003-935003-7 (2015)

[A7] S. Indrišiūnas, B. Voisiat, A. Rėza, I. Šimkienė, R. Mažeikienė, A. Selskis, and G. Račiukaitis, Influence of surface modification by laser beam interference ablation on characteristics of p-Si solar cells, *Proc. SPIE* **9180**, 918007 (2014).

[A8] B. Voisiat, **S. Indrišiūnas**, R. Suzanovičienė, I. Šimkienė and G. Račiukaitis, Formation of periodic structures on silicon by laser beam interference ablation technique for light control in solar cells. *Proc. SPIE* **9180**, 918009 (2014).

Not directly related to this thesis (ISI WoS – with Conference Proceedings)

[A9] L. Minkevičius, **S. Indrišiūnas**, R. Šniaukas, B. Voisiat, V. Janonis, V. Tamošiūnas, I. Kašalynas, G. Račiukaitis and G. Valušis, Terahertz multilevel phase Fresnel lenses fabricated by laser patterning of silicon. *Opt. Lett.* **42**, 1875-1878 (2017).

[A10] B. Voisiat, **S. Indrišiūnas**, R. Šniaukas, L. Minkevičius, I. Kašalynas and G. Račiukaitis, Laser processing for precise fabrication of the THz optics. *Proc. SPIE* **10091**, 100910F-100910F-10 (2017).

[A11] M. Gedvilas, B. Voisiat, **S. Indrišiūnas**, G. Račiukaitis, V. Veiko, R. Zakoldaev, D. Sinev and E. Shakhno, Thermo-chemical microstructuring of thin metal films using multi-beam interference by short (nano- & picosecond) laser pulses. *Thin Solid Films*, **634**, 134-140 (2017).

1.4.2 Conference presentations

Directly related to the topic of this thesis

[C1] S. Indrišiūnas and G. Račiukaitis, *Modelling of periodical surface structures in silicon for efficient light absorption*, "Lazeriai ir optinis netiesiškumas" XX Lietuvos ir Baltarusijos seminaras, Vilnius, Lithuania, November 21–22, 2013.

[C2] S. Indrišiūnas, B.Voisiat, A. Rėza, I. Šimkienė, R. Mažeikienė, A. Selskis and G. Račiukaitis, *Influence of Surface Modification by Laser Beam Interference Ablation on Characteristics of p-Si Solar Cells*, LPM2014, The

15th International Symposium on Laser Precision Microfabrication, Vilnius, Lithuania, June 17–21, 2014.

[C3] B. Voisiat, **S. Indrišiūnas**, R. Suzanovičienė, I. Šimkienė, and G. Račiukaitis, *Formation of Periodic Structures on Silicon by Laser Beam Interference Ablation Technique for Light Control in Solar Cells*, SPIE Solar Energy + Technology, San Diego, USA, August 20 – 21, 2014.

[C4] S. Indrišiūnas, B. Voisiat, A. Rėza, I. Šimkienė, R. Mažeikienė, A. Selskis and G. Račiukaitis, *Influence of Surface Modification by Laser Beam Interference Ablation on Characteristics of p-Si Solar Cells*, SPIE Solar Energy + Technology, San Diego, USA, August 20 – 21, 2014.

[C5] S. Indrišiūnas, B.Voisiat, A. Rėza, I. Šimkienė, R. Mažeikienė, A. Selskis and G. Račiukaitis, *New Approaches for Texturing of Silicon Solar Cells Using Laser Beam Interference*, „29th European PV Solar Energy Conference and Exhibition" (EU PVSEC 2014), Amsterdam, The Netherlands, September 22–26, 2014.

[C6] S. Indrišiūnas, B. Voisiat, A. Rėza, I. Šimkienė, R. Mažeikienė, A. Selskis and G. Račiukaitis, *Light-harvesting structures for photovoltaic elements using laser beam interference*, Laser Processing in Photovoltaics, Leipzig, Germany, November 27–28, 2014.

[C7] S. Indrišiūnas, B. Voisiat, A. Žukauskas and G. Račiukaitis, *Direct laser beam interference patterning technique for fast high aspect ratio surface structuring*, Laser Applications in Microelectronic and Optoelectronic Manufacturing (LAMOM) XIX, San Francisco, USA, February 7-12, 2015.

[C8] R. Mažeikienė, G. Niaura, B. Voisiat, **S. Indrišiūnas** and G. Račiukaitis, *Lazeriu tekstūruotų Si Saulės elementų tyrimas Ramano spektroskopijos metodu*, 41-oji Lietuvos Nacionalinė Fizikos Konferencija (LNFK-41), Vilnius, Lithuania, June 17–19, 2015.

[C9] S. Indrišiūnas, B. Voisiat and G. Račiukaitis, *Direct laser beam interference patterning for fabrication of plasmonic hole arrays*, Lasers in Manufacturing (LiM2015), Munich, Germany, June 22-25, 2015.

[C10] S. Indrišiūnas, B.Voisiat, A. Rėza, I. Šimkienė, R. Mažeikienė, A. Selskis, and G. Račiukaitis, *Direct Laser Beam Interference patterning combined with wet chemical etching as a tool to control surface morphology of multicrystalline silicon*, „30th European PV Solar Energy Conference and Exhibition" (EU PVSEC 2015), Hamburg, Germany, September 14 – 18, 2015.

[C11] B. Voisiat, **S. Indrišiūnas**, M. Gedvilas and G. Račiukaitis, *Direct Laser Interference Patterning of Thin Metal Films to Control the Flow of Electromagnetic Radiation*, International High Power Laser Ablation & Directed Energy Symposium (HPLA/DE), Santa Fe, USA, April 4–7, 2016.

[C12] S. Indrišiūnas, B. Voisiat, A. Žukauskas, V. Strazdienė, I. Šimkienė, A. Rėza, M. Gavutis, T. Rakickas and G. Račiukaitis, *Fabrication of periodic structures on silicon using direct laser interference ablation and wet chemical etching*, The 17th International Symposium on Laser Precision Microfabrication (LPM 2016), Xi'an, China, May 23–27, 2016 (**Outstanding Student Paper Award (Oral)**).

[C13] S. Indrišiūnas, B. Voisiat, M. Gedvilas and G. Račiukaitis, *Polarisation Control in Direct Laser Interference Ablation Setup for Flexible Generation of Periodic Patterns,* The 18th International Symposium on Laser Precision Microfabrication (LPM 2017), Toyama, Japan, June 5–8, 2017.

Contribution to other presentations at conferences (not directly related to this thesis)

[C14] M. Gedvilas, B. Voisiat, **S. Indrišiūnas**, G. Račiukaitis, V. Veiko, R. Zakoldaev, D. Sinev and E. Shakhno, *Thermochemical recording of interference patterns on thin Cr-films by picosecond laser pulse irradiation - experimental realization & theoretical modelling*, 13th International Seminar „Mathematical Models & Modelling in Laser Plasma Processes & Advanced Science Technologies" Petrovac, Montenegro, May 30 – June 6, 2015.

[C15] V. Markovic, O. Černašėjus, G. Vaitkūnaite, Z. A. Mierzejewska, R. Lukauskaite and **S. Indrišiūnas**, *Investigation of the laser beam influence on the parts built by SLS*, Mechatronic Systems and Materials (MSM 2015), Kaunas, Lithuania, July 7–9, 2015.

[C16] M. Treideris, V. Strazdienė, I. Šimkienė, V. Bukauskas, A. Rėza, **S. Indrišiūnas**, M. Kamarauskas and A. Šetkus, *Optical Reflection Spectra of Silicon Surface with Nanowires Produced by Special Electrochemical Etching*, „32th European PV Solar Energy Conference and Exhibition" (EU PVSEC 2016), Munich, Germany, June 20–24, 2016.

1.4.3 Authors contribution

The author of the thesis made the main theoretical and experimental work of this study. His contribution includes:

- Development and assembly of the experimental setups.
- Experimental DLIP patterning work.
- Experimental work to improve DLIP technique.
- Development of computer software required for the experiments.
- Characterization of the fabricated structures using SEM, AFM techniques, Raman spectroscopy, EDS spectroscopy, I-V characteristics measurement setup.
- Theoretical simulation of light harvesting in the periodic gratings in silicon.
- Simulation of the interference intensity distributions under various conditions.
- Visualization, modelling, interpretation and preparation for publication of the experimental results.
- Writing scientific publications and presentation of the results at scientific conferences.

1.4.4 Co-authors contribution

The idea of this work was conceived, and the work was supervised by Dr Gediminas Račiukaitis and Dr. Irena Šimkienė. Solar cell antireflective layer patterning experiments and measurement of electric characteristics was done in collaboration with Dr. Bogdan Voisiat. Raman spectroscopy measurements for the Chapter 4 were performed by Dr. Regina Mažeikienė. XPS and high-resolution SEM measurements were provided by Dr. Algirdas Selskis. Reflectance measurements for Chapters 4 and 6 were performed by Dr. Alfonsas Rėza. Wet chemical etching for the process described in Chapter 5 was performed partially by Dr. Martynas Gavutis. Part of the DLIP patterning experiments for Chapter 5 was performed by bachelor student Airidas Žukauskas under supervision by Dr. Bogdan Voisiat. High-resolution AFM imaging for Chapters 5 and 6 was made by Tomas Rakickas. Wet chemical etching for the process described in Chapter 6 was performed by Dr. Viktorija Strazdienė. Modelling of the temperature distributions during the irradiation with the interference field was done by Dr. Mindaugas Gedvilas. Reflectance measurement in Chapter 7 was provided by Dr. Irmantas Kašalynas. Polarisation control apparatus for Chapter 7 was constructed together with Dr. Bogdan Voisiat. FROG measurements for Chapter 7 were done by Dr. Edgar Kaksis from Vienna University of Technology.

2 Literature Review

2.1 Photovoltaics in the Global Energy Market

Renewable energy sources amount to about 22% of the World net electricity generation (Fig. 1) [9] with 1849 GW power capacity in 2015 [10]. The share of the renewable energy sources in the global electricity supply continues to grow with an estimated rate of 2.9% per year. Solar energy share among the renewable energy sources is still small. However, solar energy is the fastest growing branch of the renewable energy sources with average estimated yearly generation increase by 8.3% [9]. In 2015, solar electricity generation totalled in about 227 GW [10]. Solar energy production is getting increased attention due to its cleanliness. Furthermore, it allows getting import-independent energy for the countries with low amounts of available fossil fuels.

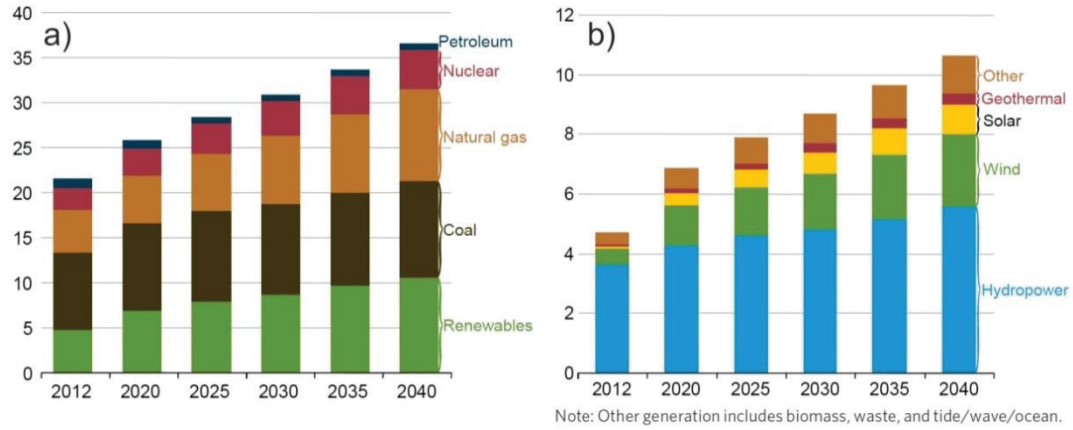

Fig. 1. World total electricity generation in trillion kilowatt-hours by energy source (a). World total renewable electricity generation in trillion kilowatt-hours by energy source (b) [9].

Growing production of PV (Photovoltaic) energy systems leads to the decrease in price per watt. This decrease may be attributed to the increase in the production scale, reduction of the amount of energy required to produce the defined amount of devices and increased efficiency of the whole production process. One more reason is an increased conversion efficiency (and/or reduced consumption of raw materials) of the PV devices. In the past, the main part of the PV energy system was the price of the PV modules. Now, expenses shifted to the parts that do not produce energy, such as cabling, racking,

inventers and maintenance. Therefore, high conversion efficiency resulted not only in the reduced consumption of raw materials but also in reduced costs for other equipment, since high conversion allows getting the same amount of energy using less solar modules [1]. The price of the PV module decreased sharply over time. From 2006 to 2011 production of PV modules underwent a boost with average growth of 78% per year, followed by an almost triple decrease in the price per watt (Fig.2). However, from 2011 to 2013 production growth was only 4% per year. Production capabilities became significantly larger than the demand for the PV modules. This led to the bankruptcy, downsizing or consolidation of a number of solar companies [9].

Some experts claim that failure of the part of solar companies may have a positive effect in the long run. Decreased supply would lead to increased profits that would allow investments in innovations and new equipment, although this process was hindered by financial help for non-competitive companies from the governments, especially in China, which is the largest world's PV modules manufacturer [11]. The decline in prices slowed down between 2013 and 2015 [12]. However, PV industry still suffers from the oversupply and dropping prices that are feared to be too close to manufacturing costs [13].

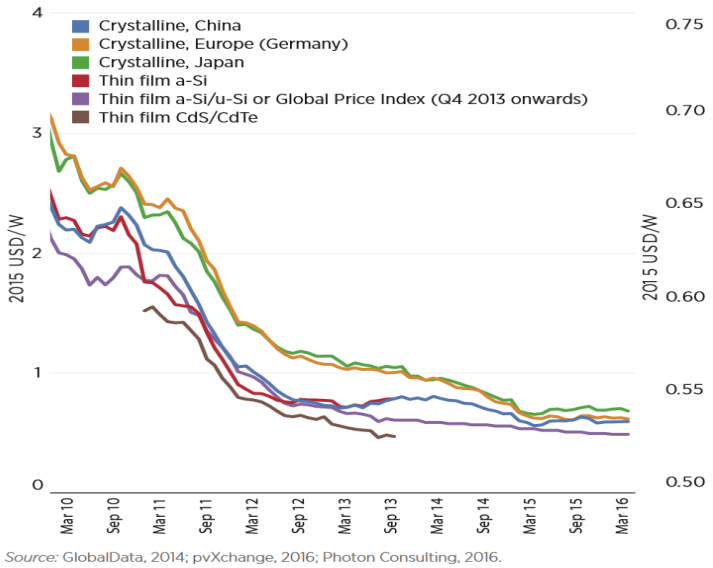

Fig.2. Global PV module price trends in 2010–2016 [12].

2.2 Overview of the Solar Cell Technology

2.2.1 Operation of a solar cell

A solar cell is a device that uses light to produce voltage and current for electric power generation. To implement such process, almost exclusively semiconductor materials forming a p-n junction are used. In the suitable material, the incoming photon is absorbed by the electron, which jumps from the valence to the conduction band. This process might be depicted as the generation of the electron-hole pair. The electron-hole system is not stable, and recombination occurs after some time that is defined as a minority carrier lifetime. To utilize solar cell for electric power generation, carriers have to be spatially separated. This is achieved in the p-n junction. If n-doped and p-doped materials are joined together, electrons diffuse from the n-type material into the p-type material (and holes vice versa) due to the significant difference in electron concentration in n- and p-type materials. Depletion zone with no charge carriers is formed. In this zone, an electric field (built-in electric field) directed from the depleted n-type to the depleted p-type region is created (Fig. 3a). Due to the existence of the built-in electric field, some electrons flow in the opposite direction to the diffusion current. Eventually, net electron (hole) flow across the p-n junction becomes zero. When the light shines on the solar cell, some of the semiconductor electrons are excited. Due to the pre-existing electric field in the junction, electrons are forced to go to the n-type and holes to the p-type material.

This causes reduction of the electric field strength across the junction and, as a result, leads to increase in the diffusion current due to electron diffusion from n-type material into p-type and vice versa for holes (forward bias current). If the circuit is open, forward bias current increases until it balances light generated current and the net current is zero (Fig. 3b). The voltage required to cause these two currents to balance is called the open-circuit voltage V_{OC}. If the solar cell is short-circuited, the photo-generated carriers flow into the external circuit and diffusion current decreases.

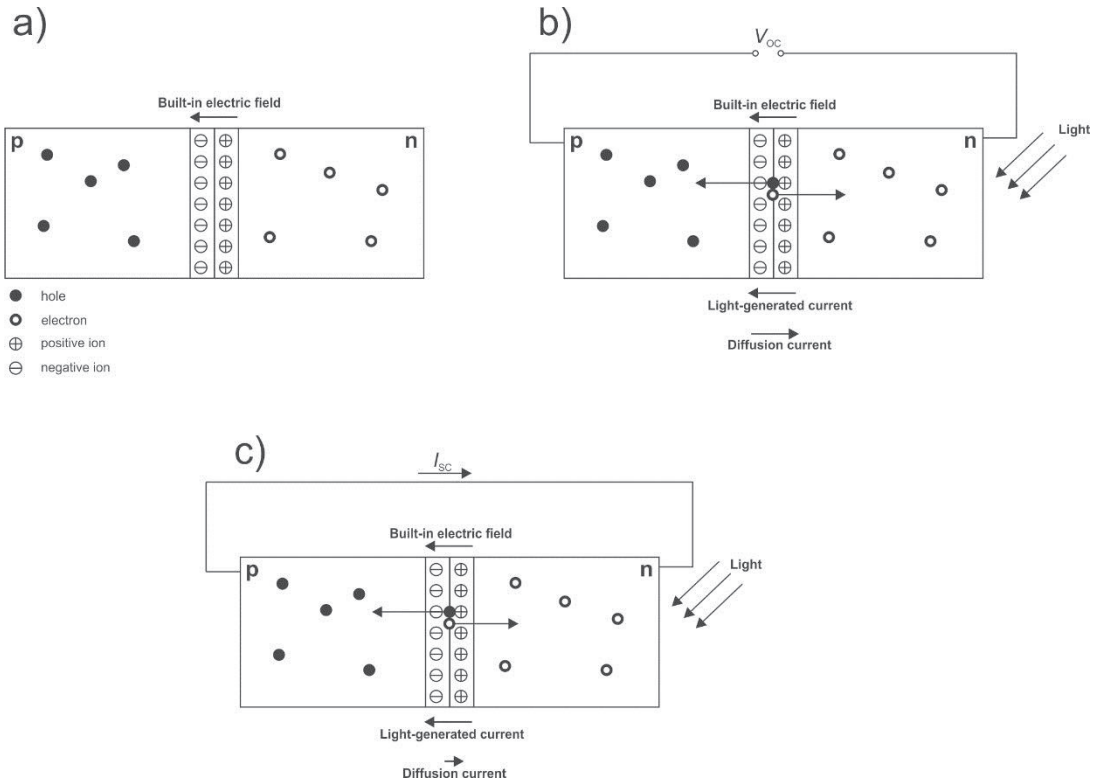

Fig. 3. Operation of the solar cell.

The current flowing through the solar cell when it is short-circuited (so the voltage across it is equal to zero) is called the short-circuit current I_{SC} (Fig. 3c). For the ideal solar cell, this current is equal to the light-generated current. It is the largest current that can be drawn from a cell [14, 15]. Fig. 4 shows an example of the I-V graph of the solar cell. The maximum generated power P_{max} is achieved at the voltage V_m and current I_m: $P_{max}=V_m I_m$. It is convenient to define the Fill Factor *FF* [15]:

$$FF = \frac{I_m V_m}{I_{SC} V_{OC}} = \frac{P_{max}}{I_{SC} V_{OC}}. \qquad (1)$$

FF along with V_{OC} and I_{SC} determines the maximum power available to extract from a solar cell. Graphically, the FF is a measure of the "squareness" of the solar cell I-V curve, and it also represents the area of the largest rectangle that can fit under the I-V curve.

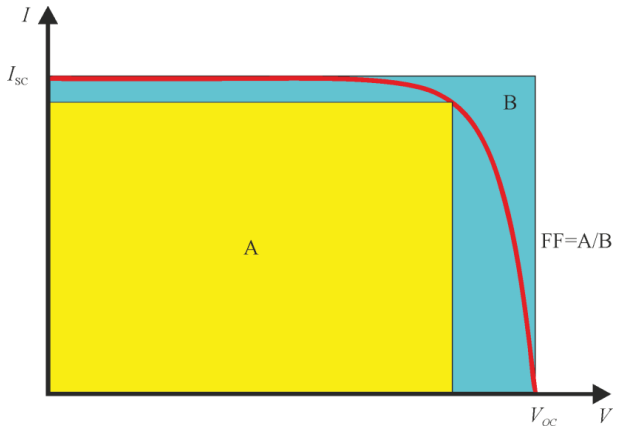

Fig. 4. Example of a solar cell IV graph.

The solar cell energy conversion efficiency η can be defined as:

$$\eta = \frac{V_{OC} I_{SC} \mathrm{FF}}{P_{in}}, \tag{2}$$

here P_{in} is the power of the light incoming to the solar cell [16].

Solar cells are often characterised using widely known equation [17]:

$$J = J_{SC} - J_0 \left(\exp\left(\frac{V}{kT/q} \right) - 1 \right), \tag{3}$$

where J is the current density, J_{SC} is the short-circuit current density, J_0 – the "dark saturation current density", the diode leakage current density in the absence of light, V is the voltage across the solar cell, k is the Boltzmann's constant and T is the (absolute) temperature. Considering this equation, current generation in the solar cell can be thought as a sum of short-circuit current, which is proportional to the photo-generation rate, and recombination losses due to the forward biased voltage, which develops across the solar cell diode. So, recombination losses lead to reduced J_{SC} and V_{OC}.

There are several sources and paths of recombination of the photo-exited electrons in the solar cell. Radiative recombination is a reverse process of photon absorption. It plays an important role only in direct bandgap semiconductors. Shockley–Read–Hall (SRH) recombination is assisted by impurities or crystal defects. Defects introduce energy levels within a forbidden band gap. This recombination process is dominant in semiconductors

under operation conditions. Auger recombination process is more critical in indirect bandgap semiconductors such as silicon. In this process, electron (hole) in the conduction (valence) band recombines by transferring its energy and momentum to the other conduction (valence) band electron (hole). Newly exited particle loses the excess energy to the lattice vibrations. The probability of the Auger recombination increases with charge carrier concentration. Therefore, it is more important in highly doped materials [14].

Surface recombination plays a crucial role in the semiconductor devices. Many valence electrons at the surface cannot form a covalent bond and remain as the so-called “dangling bonds”. Such bonds are defects that induce SHR recombination. The surface recombination rate can be reduced by deposition of the passivating layer. Free silicon valence electrons can participate in a covalent bond with the atoms of this layer. Silicon oxide and silicon nitride are widely used materials for the passivation. Another way, which is utilised in PERL (Passivated Emitter and Rear Local diffusion) cells, is to create a layer with high dopant concentration under the surface. Shockley recombination requires the presence of both an electron and a hole. If the concentration of one carrier type is significantly reduced, recombination rate also drops. The concentration of one carrier type can be reduced by creating an electric field. This can be done by creating a doping gradient below the silicon surface [18]. Such layer acts as a barrier for minority carriers, thus reducing recombination rate [14].

The shape of the surface also is essential. Fabrication of the light trapping or antireflective structures may increase the surface recombination rate. For a start, textured surface has a larger area than planar. Therefore, surface recombination for a textured surface is also larger. For example, commonly used in industry upright pyramid texture in monocrystalline silicon increases surface area by 1.73. Recombination rate can also be increased due to the exposition of different crystal orientation surfaces. The silicon (111) surface is known to provide more dangling bonds than the (100) surface [19].

2.2.2 Types of solar cells

Silicon solar cells remain dominant solar cell type on the market. They can be grouped according to the crystalline properties of the silicon from which they are made. **Monocrystalline** silicon solar cells are made from the crystalline silicon wafers that are cut from the ingot grown using the Czochralski method. They provide relatively high efficiency: theoretical efficiency of the monocrystalline silicon solar cell is 29% [20]. The current record for the actual solar cell is 26.7% [21]. However, most monocrystalline solar cells available on the market exhibit more humble efficiencies of 16–19% [22]. The most widespread manufacturing technology is the so-called "screen printing". Screen printing is a relatively simple method to make front contacts, but numerous design compromises are made to reduce costs [22]. **Multicrystalline** silicon wafers are cheaper than monocrystalline because they are cut from the silicon ingot that was cast into the mould from liquid silicon. They are usually made from cheaper "solar grade" material. The casting process is also less time and resources consuming than crystal growing [16].

The efficiency of the **PERC** (Passivated Emitter and Rear Cells) solar cells were improved by introducing better light trapping in the cell and providing better passivation for reducing recombination losses. In PERC cells, a thin dielectric layer is added between the back side of the cell and metal contact. This layer is perforated by tiny holes to ensure contact between the metal and silicon. Perforated dielectric layer reduces carrier recombination and parasitic light absorption in the back contact. At the same time, radiation incoming from the front side of the cell is deflected at various angles thus increasing light path. Additionally, excellent antireflective properties are achieved using inverted pyramid front pattern. Therefore, PERC cells have better absorption in the 1000–1200 nm spectral range than conventional monocrystalline silicon cells [22, 23]. **PERL** (Passivated Emitter and Rear Local diffusion) cells have a design similar to PERC. The differences are that PERL cells have boron doped volumes above the back contact to reduce recombination further. These

volumes create a potential barrier, preventing diffusion of holes in the region near the back contact. Recombination at the front surface is reduced by adding a high-quality oxide layer on the top of the inverted pyramid texture [16, 22]. In the **HIT** (Heterojunction with Intrinsic Thin layer) technology, developed by Panasonic, the monocrystalline wafer is surrounded by the very thin amorphous silicon layers, thus providing a high degree of passivation [16]. In most silicon solar cell technologies dielectric passivation layers are used for avoiding surface recombination. However, the recombination in the metal contacts still remains an important factor. In PERC and PERL cells, this effect is reduced by decreasing the direct contact area between metal contacts and silicon. Another solution is to use passivating contacts which work as both the electric conductor and passivation layer [24]. In HIT solar cells intrinsic and doped a-Si:H (Hydrogenated amorphous silicon) layers are deposited on both surfaces of the n-type monocrystalline silicon wafer. Intrinsic type a-Si:H layer between the wafer and p-doped a-Si:H emitter provides good passivation of dangling silicon surface bonds. Transparent conductors with the metal grid are used as the electrodes. In 2014, HIT cells beat the long-standing silicon solar cell record of 25% efficiency held by the PERL type cells by increasing efficiency to 25.6% [25]. In 2017, the efficiency was further improved to 26.7% [21].

High-efficiency solar cells must have diffusion lengths of minority carriers several times larger than the material thickness for all photocarriers to be collected. This requirement can be fulfilled in the thin film solar cells [4]. The important outcome of the usage of thin films is that role of the bulk recombination becomes less important. This lowers the requirements for the material quality [26]. An additional benefit from reduced bulk recombination is an increase of the V_{OC}: for example, the limiting value increases from 750 mV for a 300 μm thick cell to 830 mV for a one μm thick cell [27]. In thin-film solar cells, thin material layers are deposited on glass, stainless steel or polymer substrate (so flexible solar cells are feasible). The active

semiconductor layer is deposited between the front transparent electrode and the back electrode. The thickness of the active layer is in the range of micrometre. Therefore, back reflectors and other light trapping schemes are usually implemented in the thin film devices.

Thin film silicon solar cells have lower efficiencies than other thin film devices. On the other hand, they do not require rare or hazardous elements such as cadmium or lead. Also, the efficiency drop at high operating temperatures is quite low. Non-pure silicon films (a-Si:H or μc-Si:H (microcrystalline hydrogenated silicon)) deposited by PECVD (Plasma Enhanced Chemical Vapour Deposition) from a mixture of silane (SiH_4) and hydrogen are preferable to the pure amorphous or multicrystalline silicon films because hydrogen passivates dangling silicon bonds [28]. 9.6% efficiency was reported for amorphous silicon [29], 11.0% for multicrystalline silicon [6] and 11.9% for a tandem a-Si:H/μc-Si:H devices [29].

Perovskite solar cells recently got a new wave of interest. They are easy to manufacture and strongly absorb sunlight**.** However, all reported high-efficiency Perovskites include lead. Also, they are susceptible to degradation when exposed to moisture or UV radiation. Perovskites can be described by formula ABX_3, where X is an anion, A is a large cation and B is a smaller cation. In the Perovskites that are promising in photovoltaics, the X is usually I (but can be Cl or Br), A is methyl-ammonium ion (CH_3NH_3), and B is Pb [30]. The Perovskite solar cell consists of the following layers: fluorine-doped tin oxide (FTO) coated glass substrate, a porous layer of a nanocrystalline metal oxide, sunlight-absorbing Perovskite layer and a hole-transporting material. 20.1% efficiency was reported in 2013 [31]

Silicon solar cells are reaching their theoretical efficiency value. The next step would be to combine silicon solar cell with a low-cost wide bandgap cell in the tandem cell configuration. Perovskite materials are promising for tandem applications due to the steep absorption edge, low absorption below the bandgap and tuneable between 0.56–0.83 μm bandgap [32].

$CuInGaSe_2$ (CIGS) and **CdTe** solar cells are often classified as chalcogenide, as they contain chemical elements included in the chalcogenide group of the periodic table (O, S, Se, Te, Po)**.** On the laboratory scale, the record cell efficiencies for the CIGS can reach up to around 22% [33, 34]. Commercial module efficiency, however, is close to 15%. CIGS material is deposited between Mo back contact (which in turn lies on the glass, metal foil or polymer substrate) and transparent front contact. $MoSe_2$ layer forms between the Mo and CIGS during the CIGS growth process. Additional layers are deposited between the CIGS and front contact [35].

2.3 Light Management in the Solar Cells

There are several sources of efficiency losses in the photovoltaic cells. For example, silicon exhibits quite a high reflection (over 30% in the visible range) due to high refractive index contrast comparing to air. Another problem is how to ensure absorption of photons in the thin layers of materials for thin film solar cells. Even in the relatively thick conventional silicon solar cells low energy photons are not efficiently absorbed in the single pass through the silicon wafer (Fig. 5). Absorption of low energy photons is preferable because it causes less heating in the solar cell. When a photon with energy much larger than bandgap is absorbed, “hot” carrier is generated, that gives its energy to surrounding medium through the thermalisation process [36].

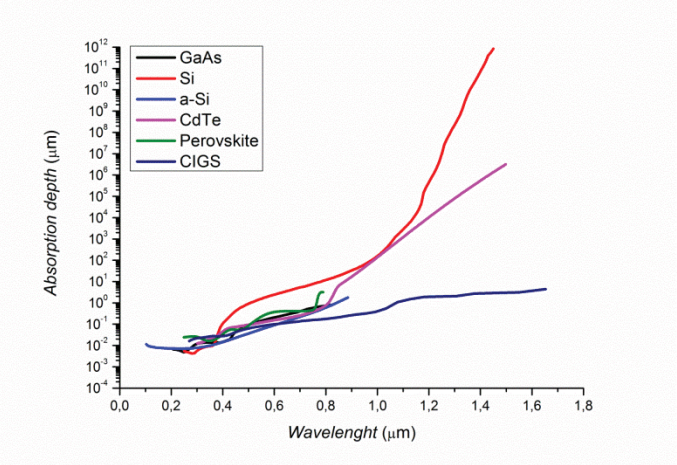

Fig. 5. Absorption depth for several solar cell materials across the spectrum. Data were taken from [37-42]

2.3.1 Antireflective coatings

Antireflective coatings are thin dielectric layers designed in such way that irradiation reflected from the coating top layer and coating-substrate interface interfere destructively thus reducing reflection from the front surface of the device. For silicon solar cells, silicon nitride with a thickness of about 70 nm is usually used to provide reflection minimum at the 600 nm wavelength. Planar antireflective coatings are simple and suitable for large-scale industrial manufacturing. However, they have some drawbacks. Firstly, a single-layer antireflective coating provides minimal reflection for the specific wavelength and angle of incidence only. Secondly, such layers act as an antireflective for the light coming from the bulk of the PV cell also: light reflected from the back surface of the active layer will pass through such layer unscathed. Therefore, antireflective coatings provide no light trapping [43]. Advanced antireflective coating designs such as moth-eye structures are under consideration. Sub-wavelength conical texture provides gradual refractive index change in the antireflection layer [44]. Such structures could provide not only very efficient light absorption but also ensure the unhindered performance of the device in humid conditions due to superhydrophobic properties of the texture [45].

2.3.2 Light harvesting using supra-wavelength structures

In thick silicon solar cells, light harvesting is ensured using structured front surface, which provides antireflective properties, optical path enhancement and light trapping properties due to total internal reflection inside the silicon wafer. In monocrystalline silicon solar cells, the most widely used front-side structure is upright random pyramid structure [46], obtained using anisotropic wet chemical etching (Fig. 6b).

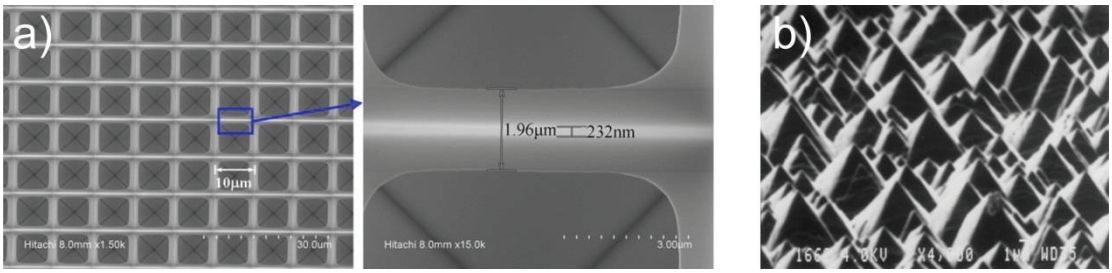

Fig. 6. Pyramid patterns in crystalline silicon. a) inverted pyramid pattern [47]; b) random upright pyramid pattern [48].

Usually, low concentration KOH or NaOH solutions in water with the addition of isopropyl alcohol are used. [49]. Another well-known structure is inverted pyramid structure (Fig. 6a) [46] also obtained by anisotropic etching but, in this case, using a mask to obtain highly regular structure [47]. Inverted pyramid structure is very efficient for light trapping through total internal reflection: the optical thickness of the silicon wafer can be enhanced up to 40 times using this structure [50]. Such structures provide the antireflective effect because light rays that are reflected from the side walls will hit silicon surface again one or more times. In the regular upright pyramid structure, 83% of incoming light rays experience double bounce and 11% triple bounce from the surface. In random upright pyramid pattern, about 70% of light rays are bounced twice. Percentage of rays that encounter three bounces depends on whether there is an overlap between pyramids and ranges between 19–26% (the rest of the rays bounce 4 or more times). Regular inverted pyramid pattern (providing there is no flat area between the pyramids) provides about 42% rays with three bounces. This is significant superiority over the upright pyramid

patterns. About 97% of photons, which bounces from the silicon surface three times, will be absorbed. [51]. Inverted pyramids also provide light trapping capability: lower energy photons that are not absorbed in the bulk of the silicon are reflected back toward the front surface. There is the probability that they will hit the surface texture at such angles that will result in the reflection back to the silicon. Finally, photons enter silicon obliquely, and this increases the probability for them to be absorbed closer to the p-n junction. It is crucial if the carrier diffusion length is comparable to the cell thickness [52].

In the multicrystalline silicon, anisotropic wet chemical etching cannot be successfully applied due to random orientation of the silicon crystallites. In some locations, the (100) crystal surface (preferable for etching) will be facing the exterior. In the other locations, the (111) surface will be in place. Therefore, the alkaline etched wafer will have some distribution of low and high reflectance areas. Although alkaline etching of multi-crystalline silicon wafer can reduce overall reflectance, it will be quite close to the reflectance of the uniformly polished wafer [53]. Furthermore, gaps or steps between the crystal grains may be produced using alkaline etching [52]. They result in lowered V_{OC} and FF parameters of the solar cell [54]. Isotropic acid etching using solutions containing HF /HNO_3 allows obtaining irregular groove structure [53]. To get non-planar surface after the isotropic etching step, some irregularities must be present on the surface. Usually, the fresh wafer already has an irregular surface, produced during the cutting process. Isotropic etching is used for this so-called saw damage removal, to eliminate surface layer with abundant defects. In the same process, a surface that has some antireflective and light trapping properties are made. [52]. RIE (Reactive Ion Etching) technique for the fabrication of light management texture was also extensively investigated. It was shown that RIE texturing provides lower reflectance than acid etching [52, 55]. However, RIE process induces defect formation in silicon. Therefore, an additional wet chemical etching step is needed to remove this damage. However, additional etching lowers sample reflectance [56].

Nevertheless, increased conversion efficiency due to increased absorption in the <600 nm wavelength region was demonstrated using RIE etched and post-processed in acid solution silicon [55].

Acid etching through the mask can be used to obtain a structure similar to the inverted pyramid pattern. By etching through hexagonal oxide mask hemispheric shaped wells can be fabricated. 1.6% efficiency increase compared to conventional multicrystalline silicon wafer was demonstrated [50].

Direct laser writing (DLW) was also investigated as a method for fabrication of textures for light management. Ablation of grooves [57] and pits [58], followed by wet chemical etching reduces the reflectance of the wafer (Fig. 7). The etching step is required to remove surface layer with abundant laser-induced defects. Nanosecond UV pulses cause reduction of minority carrier lifetime to 4 μs [58], that is much lower than usual minority carrier lifetimes which can vary from about 20 μs to 100 μs, depending on the wafer quality [59]. Reflectances of the textures, produced in the multicrystalline silicon using various methods, are compared in Fig. 7.

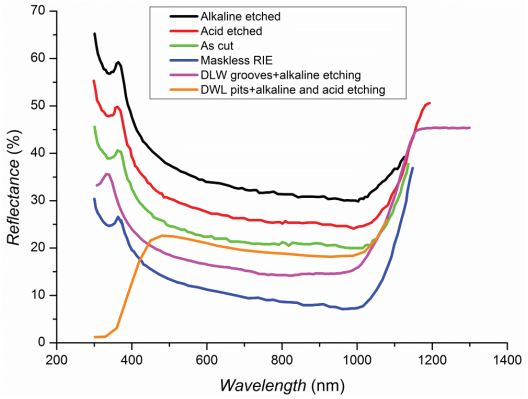

Fig. 7. Reflectance curves of multicrystalline silicon wafers with surface textures. Green line - wafer with saw damage [52], black line - alkaline etched [52], red – acid etched [52], blue - maskless RIE textured [52], magenta – grooves formed using direct laser writing and wet chemical etching [57], orange pits formed by DLW and wet chemical etching [58].

2.3.3 Diffractive/sub-wavelength light-harvesting structures

Despite the industrial suitability and fair performance of the supra-wavelength structures, there is a need for improvement. Conventional pyramid structures are not suitable for thin film solar cells due to their relatively large height. Furthermore, they cannot be used for other materials, lacking crystal structure compatible with anisotropic etching. Finally, they are not perfect light scatterers. The optical thickness of the silicon wafer can be enhanced up to 40 times using inverted pyramid texture. In silicon, perfect light scatterer could produce optical path enhancement by the factor of 50. Such ideal scatterer is called Lambertian scatterer. Lambertian scatterer is an ideally rough surface, ensuring the same light brightness in all scatter directions. Therefore, part of the light that propagates obliquely to the front surface is increased. If there is an ideal reflector on the back surface of the wafer, the optical path enhancement, compared to the wafer with the flat front surface, reaches $4n^{2,}$ where n is the refractive index of the material. Such enhancement is called Lambertian or Yablonovitch limit. If Yablonovitch limit were reached in silicon, several micrometer thick wafers would be sufficient for efficient absorption of solar light [60, 61]. It was shown that, in some cases, optical path enhancement could exceed $4n^2$ [60]. Nevertheless, Yablonovitch limit is often used as a mark against which light trapping approaches can be compared.

Various structures were proposed to overcome these problems. Numerical investigations concerning various microstructure gratings can be found in the literature. It was shown that breaking of symmetry could help to improve the performance of the pyramid array [60]. Also, the two-dimensional gratings are preferable to one-dimensional grating due to the increased number of diffraction orders. Maximal absorption is provided when the period of the structure is slightly smaller than the wavelength [62]. Tapering of the grating helps to reduce reflection from the structure due to the smooth transition between different refractive index mediums. Among the other investigated structures, an array of non-symmetric rods with pyramidal points was found to

be very close to the Lambertian scatterer, and even surpass it in some wavelength ranges [60]. However, application of such structures is questionable due to difficulties to passivate high-aspect-ratio or sharp surface features. It was shown that wafer surface roughness denoted as a number of "turning points" (number of hills and valleys on the etched wafer) significantly influences passivation quality. The largest number of turning points results in a minimum of effective minority carrier lifetime of passivated wafers. Irregular deposition of silicon atoms and variation of film thickness in the valleys and peaks of the pyramidal structure was found to be responsible for that [49].

Nevertheless, silicon, processed using various methods to produce a broad range of sub-wavelength surface structures (black silicon), is widely investigated as a light-harvesting structure, due to its outstanding antireflective properties. Black silicon encompasses a number of different structures, fabricated using various methods. For example, needle-like structures can be formed using deep RIE or metal-assisted wet chemical etching. Porous surface can be produced using wet chemical etching in HF/HNO_3. Using laser processing in a gas environment, high aspect ratio spikes can be fabricated [63]. Absorption of silicon with such textures is very high. It surpasses absorption of the inverted pyramid texture and can reach over 99% in the visible spectral range. However, there is a trade-off between good antireflective properties in the visible range and light trapping of the infrared wavelengths: black silicon structures, exhibiting very high absorption in the visible range, act as poorer light trapping structures for the infrared, compared to the inverted pyramid pattern, and vice versa. Nevertheless, black silicon offers a way to increase light harvesting. It is also very attractive for usage in thin-film solar cells. The issues, concerning surface passivation and deposition of metal contacts, are among the most important downsides of the black silicon PV technology. Black silicon structure has a huge surface area, which needs to be passivated. At the same time, passivation is hard to achieve, due to the narrow and deep features of the black silicon texture. Al_2O_3 coatings are

among the most promising passivation materials [64]. Due to these issues, the electrical characteristics of the black silicon solar cells are poorer, compared to the conventional silicon solar cells. Current black silicon solar cell efficiency record is 22.1% [65].

One more class of the light management structures investigated in literature is periodic structures in the top contact or passivation layer of solar cell device. Increased absorption was observed in the a-Si:H thin-film solar cell with a periodic hole array in both a-Si:H and the top ITO electrode [1]. Sub-micrometre texturing of the photoresist deposited on the top of the GaAs solar cell using laser interference lithography provided over 2% increase in the cell efficiency [2]. Simulations and experimental results showed an increase in photo-electrical conversion efficiency of the photovoltaic element with nanohole patterned antireflective layer [3]. Usually, periodic arrays in the passivation layer are formed utilising interference lithography combined with the reactive-ion etching [3, 66].

Texturing of the substrate of thin film solar cells is also among the light harvesting enhancement methods provided in the literature [6, 7]. Some authors tried to model separate approaches for antireflection and light trapping using conical silicon structures. Simulations show that sub-wavelength period and high aspect ratio silicon cones on top of thin film silicon layer provides good antireflective properties. Conic sub-wavelength structure acts as a gradient refractive index layer for incoming light, thus reducing reflection. The light trapping cone structure positioned on the bottom of the cell increases absorption probability of long wavelength photons. The optimal period of the structure is close to the required wavelength (800–1100 nm for silicon) [67].

2.3.4 Plasmonic light trapping

There are several plasmonic light trapping concepts. One of them is to place small metal particles on the top of the PV element (Fig. 8a). If their properties are properly selected, such particles scatter the incoming light and act as

antireflective structure, because the preferential scattering direction is into the high refractive index substrate. Moreover, optical path length inside the active layer is increased due to the angular scattering [5]. Additionally, light reflected from the back reflector may reach particles from the substrate side, and in this case, it will also be scattered back to the high refractive index material [4]. In thin semiconductor layers, the scattered light may be coupled into the guided modes, propagating parallel to the surface. Another concept is to pattern the metal back contact (Fig. 8b). Then light not absorbed in the semiconductor layer interacts with the scattering substrate and is coupled into the guided modes or Surface Plasmon Polariton (SPP) modes [5]. The third way to utilise plasmonic structures is to take advantage of the strong electric field enhancement very close to the metal nanoparticles to increase absorption in the material surrounding a particle (Fig. 8c) [4].

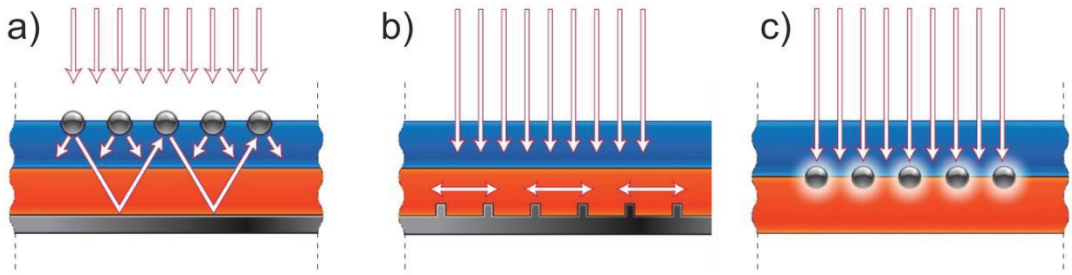

Fig. 8. Plasmonic light trapping concepts [4].

The size and shape of the particles have to be taken into consideration. In the relatively big particle, the phase of the impinging electric field is not constant across it. Therefore higher than dipolar plasmon modes are excited [43]. Small particles scatter light into the broader angular distribution than large particles. On the other hand, large particles exhibit stronger scattering intensity and lower absorption cross-section. In [68], authors advocate the use of nucleated particles consisting of a large core surrounded by 1/5 times smaller particles. The large core provides strong scattering in the long wavelength region, while small particles act as large angle scatterers in the short wavelength region.

Some plasmonic structures were tested experimentally. 60 nm wide Ag stripe array was shown to increase 40% in the photocurrent over the bare Si film. The non-periodic array provides enhancement of 55%. This grating efficiently couples the incident light to a waveguide mode supported by the Si layer when the reciprocal lattice vector of the grating matches to the propagation constant of the guided mode. Periodic array results in sharp features in spectral current density spectra whereas non-periodic distributes enhancement across the broad spectral range due to the existence of many periods [69]. Effect of the introduced randomness to the gold disk array on the glass substrate was investigated in [70]. In the random arrangement, each metal particle has a slightly different resonance wavelength. This results in broadening of the sum resonance. Such effect may be positive in the solar cell applications. Furthermore, fabrication of random structures in more suitable for industrial fabrication, for example, using chemical synthesis. In [71], the performance of the 450 nm period spheroidal particles deposited on the silicon nitride layer on the flat silicon wafer was investigated. Such array provided about 20% absorption enhancement in the long wavelength region. Authors claim that only 3% of the radiation is absorbed in the metal particles.

One of the questionable aspects of plasmonic structures in solar cells is extraordinary absorption in metals at the plasmon resonance wavelengths [72]. Simulations show that absorption in the active layer of the cell at plasmon resonance wavelength decreases due to excitation of surface plasmons in the nanoparticles [73]. On the other hand, large nanoparticles tend to act as reflectors for short wavelength irradiation [74].

2.4 Interaction of Laser Radiation with Material

Interaction of the high energy density laser beam with the material is a complex process and involves such effects as melting, nano/micro particle spallation, sublimation, amorphisation and crystallisation, the creation of the shock wave and even can result in bandgap modification through

crystallisation of material in confined volume [75]. Laser irradiation interaction with material depends on the bandgap of the material. In dielectrics, short wavelength (UV) laser can be used to induce single photon absorption. High intensity longer wavelength pulses allow multiphoton absorption. In metals, photons are absorbed by the free electrons. In the semiconductors, electron-hole pairs are created when electrons are excited to the conduction band through direct or indirect (involving emission and absorption of phonons) absorption. Free carriers further gain energy by absorption. Subsequently, hot electrons and holes are produced. Additionally, high energy carriers are provided by Auger recombination. High-energy electrons can increase the number of electrons in the conduction band by impact ionization. Eventually, thermal equilibrium between carriers will be reached through carrier collisions, production of plasmons, impact ionisation [76, 77]. Free carrier system in silicon is thermalised during the approximately 100 fs [77, 78]. The carrier energy is transferred to the lattice by the emission of phonons during the material specific electron-phonon relaxation time. For example, the silicon electron-phonon relaxation time is in the range of 200 – 240 fs [79, 80]. This time depends on the peak surface carrier density (irradiation fluence). When critical carrier density ($2 \cdot 10^{21}$ cm^{-3}[77] or approximately 0.08 J/cm^2 fluence for 800 nm wavelength 100 fs pulse duration pump beam [79]) is reached, electron-phonon relaxation time grows with the increasing carrier density [79]. Heating of the lattice results in melting, vaporisation, sublimation or spallation of the material followed by annealing and/or modification of surrounding material [81]. The outcome of the ablation process depends on the laser pulse duration.

During the ablation process with the femtosecond pulse, heat conduction into the sample can be neglected, because the lattice is heated on a (sub)picosecond time scale, and direct conversion to the vapour and plasma phases takes place. In such regime, the heated material volume, in theory, coincides with the removed material volume. Therefore, precise material removal and very small

thermal effect to the surrounding material can take place [82]. In metals, the thermal penetration depth L_{th} depends on the pulse duration τ_p and the thermal diffusivity $\kappa C_p/\rho$, where κ is thermal conductivity, C_p specific heat capacity and ρ is density [83]:

$$L_{th} = 2\sqrt{\frac{\kappa C_p}{\rho} \cdot \tau_p^{\,2}} \tag{4}$$

In the picosecond regime, vaporisation still is a critical factor. However, heating of the surrounding material and formation of the melt zone takes place. In the long pulse regime, heat diffuses relatively deeply into the material and conversion to vapour takes place only as a transition from liquid [82].

However, short pulse duration does not automatically ensure good quality of the ablated surface. It was shown, that there exists an optimal irradiation fluence for the specific material, which provides the lowest surface roughness and highest material removal rate [84]. Even when the fluence is optimal, the good quality regime may be lost due to heat accumulation from high repetition rate pulses [85].

2.5 Laser Interference Patterning

When several coherent laser beams intersect each other, their intensity is modulated due to interference. Interference patterning was tested with a broad range of materials, such as transparent conducting oxides [86], silicon [87], thin metal films [88], bulk metal surfaces [89], transparent materials[90] and various photoresists [91, 92]. Using the interference method, 2D surface structures and 3D polymer structures were demonstrated. It was shown, that shape of the 3D structure can be tuned using several exposures and selecting appropriate sample orientation concerning the direction of interfering beams for each exposure. In this way, patterns representing all fourteen Bravais lattices can be formed [93].

Intensity distributions of several interfering beams can be modelled using expression [94-96]

$$|\mathbf{E}|^2(x,y,z)=\frac{1}{2}\sum_{i=1}^{N}|\mathbf{E}_{i0}|^2+\sum_{j>1}^{N}\sum_{i=1}^{N}\mathbf{E}_{i0}\mathbf{E}_{j0}\cdot\cos\left(\left(\mathbf{k}_i-\mathbf{k}_j\right)\mathbf{r}+\varphi_i-\varphi_j\right) \quad (5)$$

In this expression, $\mathbf{E}_{i0}$ are the electrical field amplitudes, $\mathbf{k}_i$ are the wave vectors and φ_i is the phase of the i-th wave, $\mathbf{r}$ is the radius vector, N number of the beams. Interference intensity distributions simulated using this equation using Matlab are provided in Fig. 9.

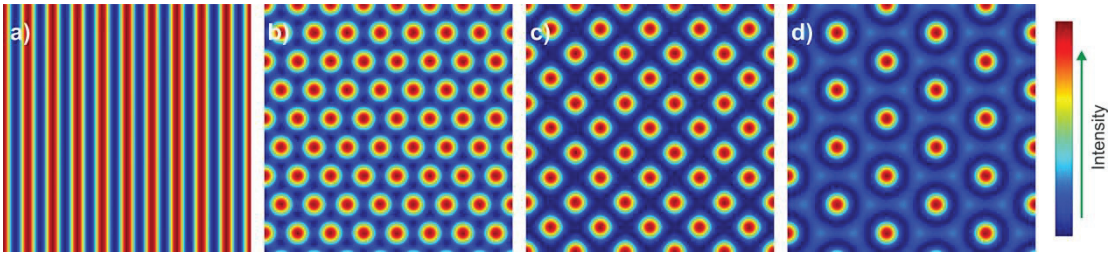

Fig. 9. Simulated interference intensity distributions. a) –2 beams; b) – 3 beams; c) – 4 beams; d) – 6 beams. Intensities, polarisation states and phases are equal for all beams.

2.5.1 Interference patterning setups

There is a number of optical setups, which can be used for interference patterning. The most commonly used include a beam splitter and mirror setup [97, 98], Lloyd's mirror [99] and diffractive optical element (DOE) combined with the confocal imaging setup using 4f lens arrangement [92, 100]. A setup consisting of DOE bi-prism and focusing optics can also be found in the literature [101].

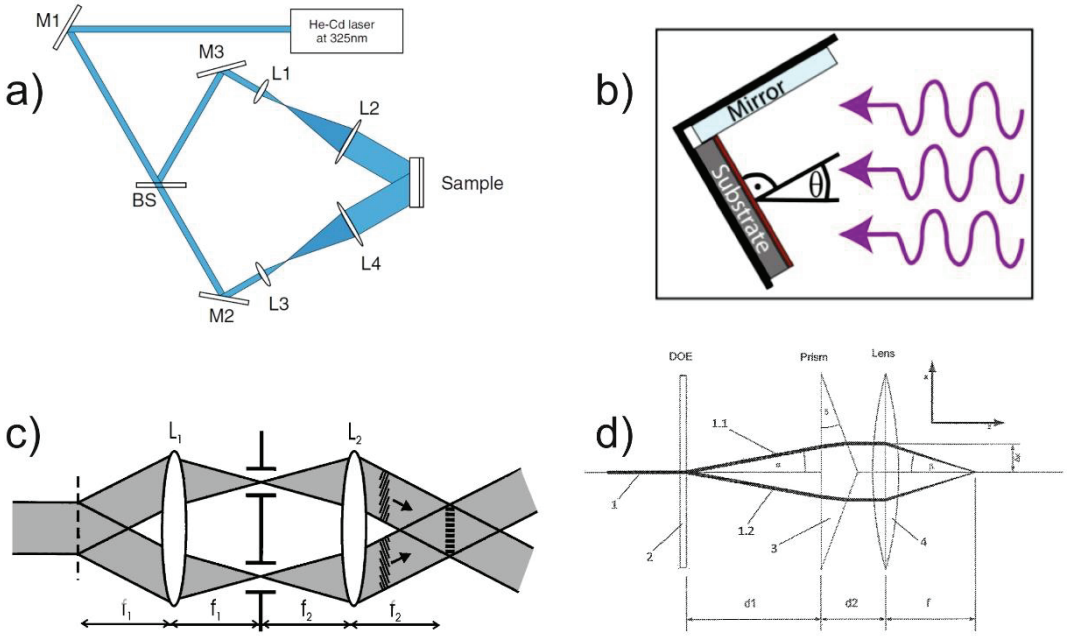

Fig. 10. Interference patterning setups. a) beamsplitter/mirror setup [102], b) Lloyd's mirror setup [99], c) confocal imaging setup [100], d) setup including DOE bi-prism and focusing objective [101].

Lloyd's mirror setup (Fig. 10b) is usually used for photolithography or some other process that requires low light intensity. It can be used to illuminate relatively large areas. Pattern period is changed by tilting Lloyd's mirror. In this way, the period can be changed continuously over the large range. The Lloyd's mirror setup is usually used for fabrication of line patterns with overlapping incident and reflected beams. More complex structures are obtained using sample rotation between several expositions. The Lloyd's mirror setup for 3-beam interference was also demonstrated [103].

The beam splitter and mirror setup (Fig. 10a) provides more flexibility in selecting the number of interfering beams. Such setup, in general, allows full control of the angle between the beams (pattern period). However, with the increased angle, the shape of the overlapping beams becomes more and more elliptical. Therefore, interference occurs only in the central region of the beams. Furthermore, such setup is not feasible to use with ultrashort pulse lasers. To get interference the difference of the optical paths between the beams has to be smaller than the spatial length of a laser pulse. For a

femtosecond pulse, the optical path difference should be less than 100 μm. Furthermore, optical setup for a large number of beams becomes quite complicated.

In the confocal imaging setup laser beam is split using diffractive optical element (DOE). Image from the DOE is transferred to the sample plane using two convex lenses (Fig. 10c). This setup provides a simple way to use ultrashort laser pulses with the interference technique [100]. On the downside, in practice, the 4f system cannot be implemented to obtain extreme angles between the beams (very small pattern periods). The angle between the interfering beams in such setup depends on the 4f system magnification. In practice, magnification up to 7 is feasible, and pattern periods up to 400 nm can be obtained using the 355 nm wavelength. Furthermore, the 4f system possesses aberrations, which grow with decreasing pattern period [104].

Setup, consisting of DOE, bi-prism and focusing objective was recently proposed (Fig. 10d). Such setup allows easy continuous adjustment of the pattern period. However, the presence of dispersive elements prevents successful usage of such setup with ultrashort laser pulses.

2.5.2 Control of the shape of the interference pattern

In the most mentioned in literature 2D patterning applications, the interference patterning was limited to obtaining the line or hole (column) patterns. Usually, a few (2, 3 or 4) beams with equal intensity and polarisation are used. In such conditions, the line intensity patterns can be generated using two interfering beams and square or hexagonal hole (column) patterns – by using 3, 4 or 6 beams. However, it would be desirable to obtain more complex shapes of patterns. For example, applications in metamaterials or metasurfaces require control over the pattern shape. To some degree, the pattern may be varied in thin-film ablation: selection of a ratio between irradiation fluence relative to

the ablation threshold provides an opportunity to obtain diverse patterns in thin films, using the same intensity distribution [94]. Formation of the ring-like, rectangular and other periodical patterns was demonstrated using the interference pattern scanning technique [94, 105]. However, the most promising opportunity to directly control the parameters of interfering beams. Interference intensity distribution depends on relative intensities of the beams, relative phase differences between the beams and beam polarisation orientations. Effects of phase and polarisation states on the intensity distribution were widely investigated using computer simulations [8, 95, 106, 107]. Experimental results were also provided in a few papers [8, 92, 94, 95, 106-108]. Several groups demonstrated that intensity patterns could be modified by inserting tiltable transparent plates in the beam path. Approach for the phase control in a 6-beam setup was demonstrated using a top-cut hexagonal prism to split the laser beam to the 6 beams (and additional central beam). The phase for each beam was changed, by placing oil layer on the prism surface, to induce a change in the beam optical path [109]. However, such methods are not suitable for large-area industrial patterning. Transparent plate causes a shift of beam position (and consequently a change of its elevation angle compared to the other beams). Therefore, spatial modulation in the interference intensity distribution arises [94]. This results in a gradual change from one pattern shape to another in the patterned surface area. So, uniform pattern area is limited to several tens of micrometres. Polarization control, on the other hand, can be achieved using conventional waveplates. No undesired spatial modulation across the interference spot arises using this approach if all waveplates are inserted perpendicularly to the beams. Moreover, the variety of interference pattern morphologies is larger when the polarisation of the beams is changed instead of a variation of the beams phases. For example, the phase shift in the 3-beam setup causes spatial translation of pattern. However, the shape of the pattern remains constant. In contrast, different intensity pattern shapes can be obtained using polarisation control in

the 3-beam setup [104]. So far, polarisation pattern control was implemented in 2-beam, 3 beam and 4-beam setups [96, 110, 111]. In all of these reports, beam splitters and mirrors were used to obtain several laser beams and combine them on the sample. However, in such setup, it is difficult to ensure that elevation angles of all beams are equal. Failure to do this results in spatial modulation of the interference pattern as well as in the case of phase control using tiltable glass plates. This modulation can be utilised to obtain combined large and small period pattern in one step. Non-symmetrical 6-beam setup was used to fabricate moth-eye structures [112]. Polarization control was also included in this configuration. However, it was used to provide the same polarisation states for all beams, but not for the pattern shape control.

A number of applications require micrometre size or sub-micrometre patterns, such as plasmonic colour surfaces [113] or plasmonic sensors [114]. Such patterns can be obtained by ensuring that the angle between the interfering beams is relatively large. For example, to get 1 – 0.5 μm period patterns using 532 nm laser wavelength, half angles between the interfering beams of 10 – 25 ° are required. In most experimental works on polarisation control in laser interference setups, relatively small, up to 10 °, half-angles between the beams were used [96, 110-112, 115].

When the angle between the interfering beams is sufficiently large, polarisation state affects modulation depth of the interference pattern. Influence of beam polarisations on the modulation depth on the two beam intensity pattern was investigated in [96]. The problem of pattern modulation depth for 2 and 3 beams was investigated in [116, 117] and the same problem for four interfering beams in [107] (for 30° incidence angle).

3 Experimental Setups and Procedures

3.1 Laser interference setups

Experimental setups for the interference patterning experiments are shown in Fig. 11. The laser beam was split into several beams using multi-spot DOE. These beams were collected on the sample surface using a confocal imaging system consisting of two objectives L1 and L2. In one instance, beams were collected using compact mirror arrangement. Each objective was composed of two plano-convex spherical lenses to reduce aberrations in the interference spot [104]. Central (zero order) beam and higher than first-order beams were blocked using an appropriate metal mask. Beam expander was used to provide required beam diameter on the DOE (Fig. 11e). In the polarisation control experiments, an additional module containing six half-wave plates was inserted between the objectives L1 and L2 Fig. 11d. Peak fluence in the interference-modulated Gaussian beam was calculated using the formula provided in Appendix B.

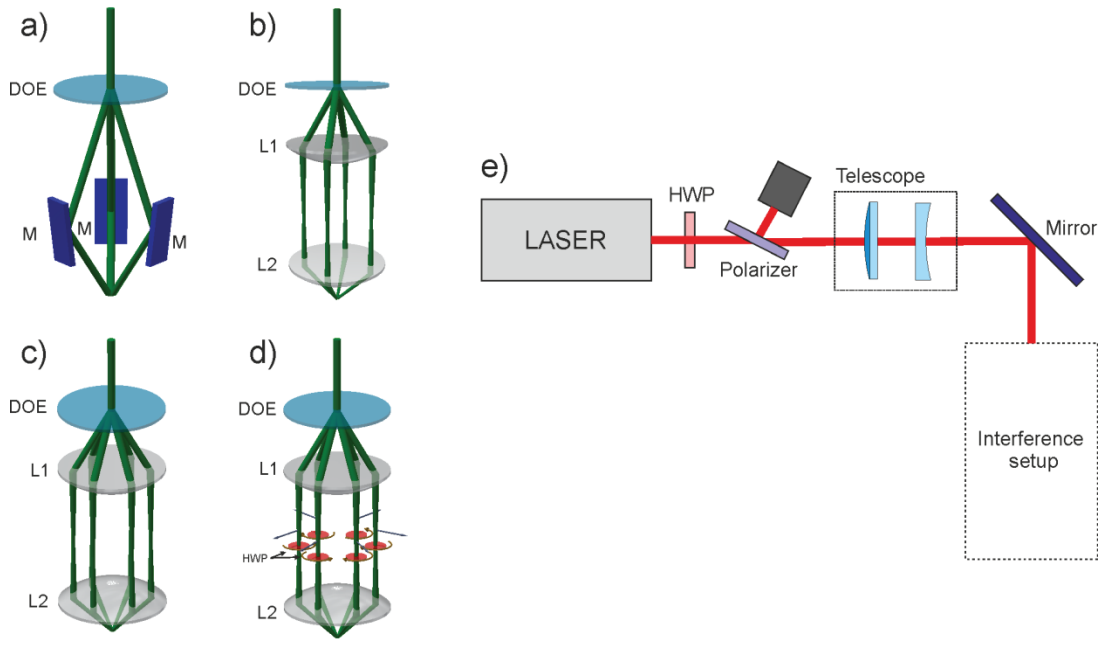

Fig. 11. Multi-beam interference patterning setups. a) – 3 beam interference patterning setup, b), c) – 4 and 6 beam interference setups utilising 4f lens systems, d) – 6 beam interference setup including polarisation control. e) – the laser beam delivery to the interference setup; M – mirror, DOE – diffractive optical element; L1 and L2 – lenses; HWP – half-wave plate.

In some experiments, patterning uniformity was increased using setups including top-hat beam shapers (Fig. 12a, b) and scanning of the interference pattern (Fig. 12c).

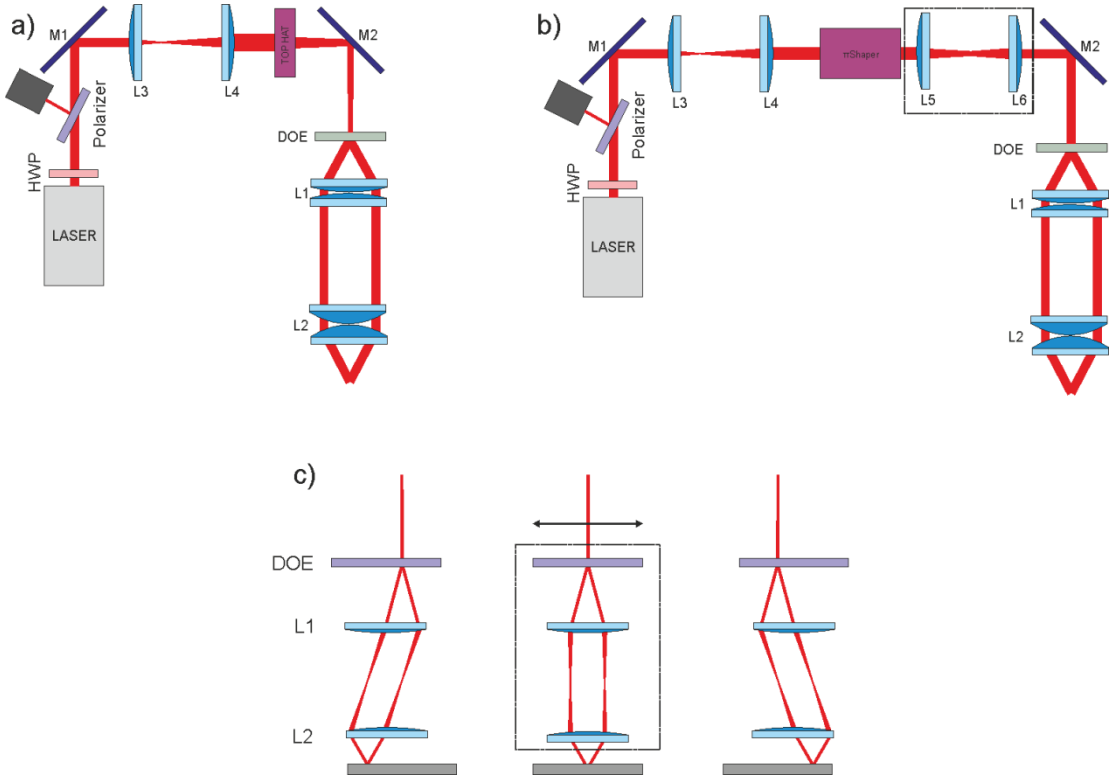

Fig. 12. Multi-beam interference patterning setups, used for increased patterning uniformity. a) – setup with Topag GTH-5-250-4 top-hat beam shaper; b) setup with πShaper 6_6_532 top-hat beam shaper; c) setup for scanning interference pattern across the sample.

Modification of the interference patterning setup shown in Fig. 11b was tested with high pulse energy (15 mJ@1030 nm), 200 fs pulse duration laser source provided by AmpLight KG. The laser beam was divided into 4 beams using Holo/Or MS-546-J-Y-A diffractive optical element. Beams were combined and transferred to the sample by the 4f lens system, consisting of 50.8 mm diameter +150 mm and +100 mm effective focal length objectives. Objectives were enclosed in the aluminium tube and acted as an input and output windows. 200 mBar vacuum was created in the tube to prevent plasma formation at the focal plane between the lenses. The optical setup and experiment arrangement are shown in Fig. 13.

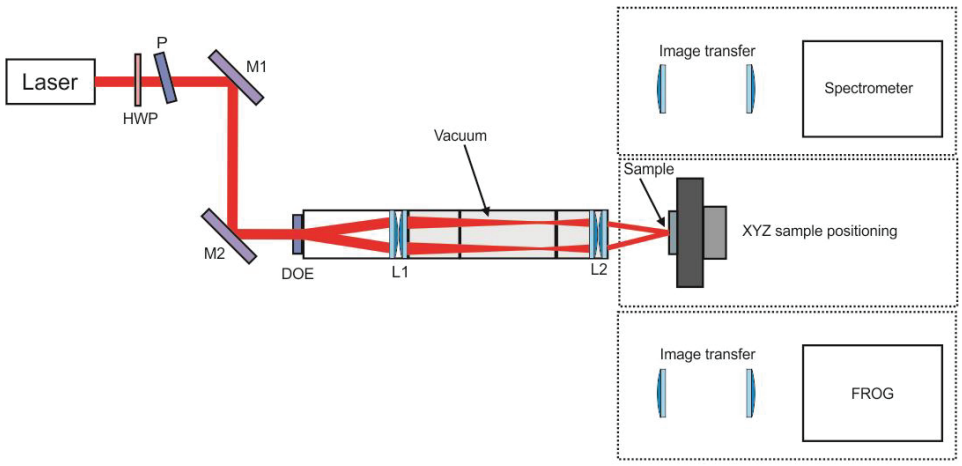

Fig. 13. Optical setup and experiment arrangement used for 4-beam interference ablation experiments with the high pulse energy femtosecond laser.

Parameters of the DOEs used in the experiments are given in Table 1.

Table 1. List of diffractive optical elements used in the experimental work.

DOE	# of beams	Wavelength	Manufacturer	Full angle
H4_532	4+1	532 nm	HOLOEYE Photonics AG	10 deg
H6_532	6+1	532 nm	HOLOEYE Photonics AG	10 deg
H4_355	4+1	355 nm	HOLOEYE Photonics AG	10 deg
MS-546-J-Y-A	4	1030 nm	HOLO/OR	7.71 deg

Several lasers were used in the experiments. Their parameters are provided in Table 2.

Table 2. Parameters of the laser sources used for interference patterning.

Laser	Wavelength (fundamental harmonic)	Pulse duration	Repetition rate	IH max. pulse energy	Available harmonics
NL220 (Ekspla)	1064	35 ns	0.5 kHz	1.2 mJ	IH, IIH
Atlantic HE (Ekspla)	1064	300 ps	1 kHz	2.7 mJ	IH, IIH, IIIH
Foxtrot (Ekspla)	1064	60 ps	4 kHz	1 mJ	IH, IIH
Pharos (Light Conversion)	1030	300 fs	10-500 kHz	0.2 mJ @1 0kHz	IH, IIH
Amplight high-pulse-energy femtosecond laser	1030	200 fs at optimal pulse compression	1000 Hz	15 mJ	IH

Laser-irradiated samples were investigated using optical and scanning electron microscopes. In some cases, interference intensity distribution was observed directly using a laser beam profiler camera.

3.2 Wet chemical etching

Isotropic and anisotropic silicon wet chemical etching processes were utilised for post-processing of the laser-textured samples. Anisotropic etching was implemented using 10% potassium hydroxide (KOH) solution at the room temperature.

Isotropic etching was performed using a mixture of nitric acid (HNO_3), hydrofluoric acid (HF) and acetic acid (CH_3COOH). Multicrystalline silicon wafers were etched 2 times: before the laser patterning and after laser patterning. For initial etching, two etchants were tested. Initial Etchant 1 (**IE1**) was 20% KOH solution in water. Etching duration 3 min, temperature 80 °C.

Initial Etchant 2 (**IE2**) was a mixture of HNO_3, HF and CH_3COOH (HNO_3:HF:CH_3COOH= (6:0,6:1,4)). Etching duration 6 min, temperature 22 °C. After the laser patterning, the etching was performed using HNO_3, HF and CH_3COOH mixture (**E3**) (HF:HNO_3:CH_3COOH:H_2O= 3.42/11/3.75/5.83 (ml)). Etching duration was varied. The temperature was 6 °C. A final short (10–15 s) etching in 3% KOH solution was used to clean the residue.

3.3 Reflectance measurement

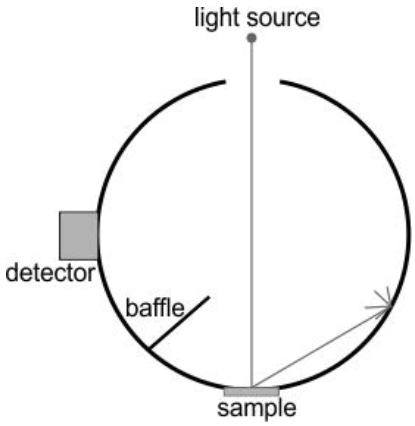

Fig. 14. Reflectance measurement using an integrating sphere.

Measurements were performed using the Shimadzu UV-VIS-NIR spectrophotometer UV-3600 coupled with the MPC-3100 unit with integrating sphere. The working principle of the integrating sphere is illustrated in Fig. 14.

3.4 Electrical measurements of solar cell characteristics

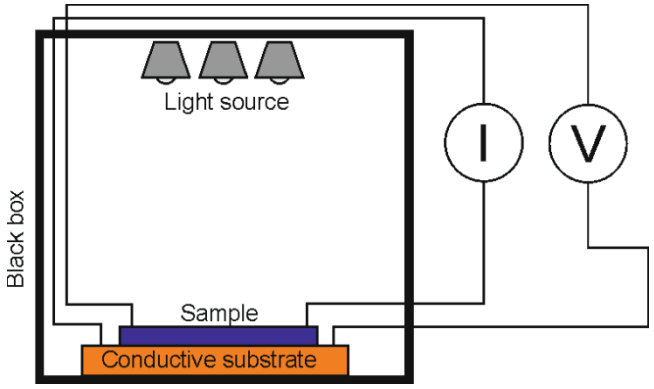

Fig. 15. Setup for electrical measurements.

Volt-Ampere characteristics of the solar cell samples were measured before and after the laser treatment using dual-channel system source Meter Keithley 2602A and a solar simulator consisting of the light source (halogen lamps), conductive substrate and an enclosure (black box). Setup is shown in Fig. 15.

The measurement error was found by measuring the I-V curve of the same solar cell sample several times. The electrical parameters of the solar cell (I_{SC}, V_{OC}, I_{max}, V_{max}, P_{max}, FF) were calculated, and measurement error was evaluated. In the following text, parameters of different solar cell samples are compared as ratios of the quantities of the same solar cell sample, before and after the texturing (for example, $I_{SC}T/I_{SC}NT$). Therefore, the measurement error is provided as the percentage of such ratio (Table 3).

Table 3. Measurement error of the solar simulator.

Parameter	Error, %
$I_{SC}T/I_{SC}NT$	0.2
$V_{OC}T/V_{OC}NT$	0.3
$I_{max}T/I_{max}NT$	0.3
$V_{max}T/V_{max}NT$	0.3
$P_{max}T/P_{max}NT$	0.5
FF T/FF NT	0.5
$\eta T/\eta NT$	0.6

3.5 Morphology, depth and element analysis

Morphology of the laser-patterned samples was investigated using an optical microscope, the scanning electron microscope (JSM-6490LV JEOL), optical

and stylus profilers and atomic force microscope (AFM). Elemental composition was investigated using EDS (energy-dispersive X-ray spectroscopy) and XPS (X-ray photoelectron spectroscopy) analysis.

3.6 Raman spectra acquisition

Raman spectroscopy can be invoked to identify materials, analyse crystalline structure and stresses in a particular material. In Raman spectroscopy, a local bonding between atoms is investigated by analysing non-elastically scattered light from the sample. In a crystalline structure, local bonds have well-defined energies. Therefore, Raman resonance peaks have narrow line-widths. In disordered or amorphous structures, bonding energies vary, and Raman peaks are broadened and usually shifted. The crystalline silicon phase is attributed to the Raman lines at 520 and 500 cm^{-1}. The amorphous phase is attributed to the 480 cm^{-1}. Crystalline silicon fraction x_C^{RS} can be evaluated by calculating intensity ratio between crystalline and amorphous silicon Raman bands [28]:

$$x_C^{RS} = \frac{I_{520}}{I_{480} + I_{520}} \tag{6}$$

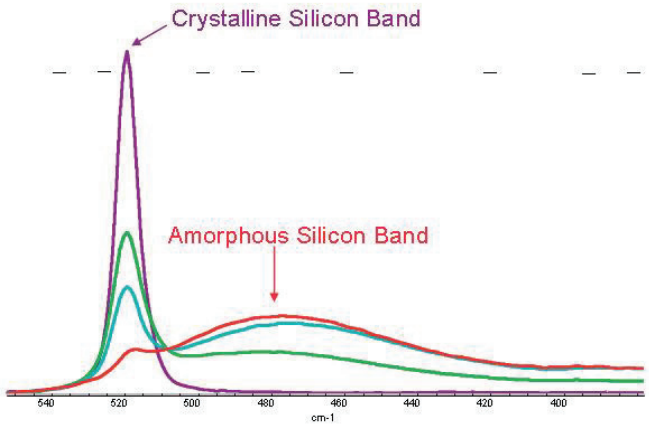

Fig. 16. Typical spectra of silicon ranging from pure crystalline to amorphous [118].

Characterization of material modifications was carried out by a micro-Raman microscope (nVia Renishaw) equipped with 633 nm and 532 nm lasers. The laser spot size was estimated to be about 2 μm. Laser power was set to 1 mW.

4 Periodic Patterning of Antireflective SiN_x Layer in Polycrystalline Silicon Solar Cells

The material, related to this chapter was published in [A1], [A2], [A3], [A7], [C2], [C4], [C6], [C8].

In this chapter, use of the direct laser interference patterning method for the structuring of SiN_x passivation layer of polycrystalline silicon solar cells was investigated. The high-pulse-energy laser source provided sufficient energy to remove or modify the material for the creation of the desired pattern without additional manufacturing steps. Two interference patterning setups were employed for this purpose. The second harmonics (532 nm) of the picosecond laser Foxtrot was used with the optical system shown in Fig. 11b. The second harmonics (532 nm) of the nanosecond laser NL220 was used with the optical system described in Fig. 11c. These setups allowed the creation of periodical intensity modulations in the Gaussian laser beam. Period of the modulation was 2.5 μm in the picosecond setup. In the nanosecond setup, the period could be adjusted from 600 nm to 5 μm. The experiments were performed on the commercial polycrystalline silicon solar cells. The cell size was 15x15cm^2; an average PV efficiency was about 11%, the cell thickness 0.25 mm. Reflection and absorption were evaluated using diffuse reflectance (Fig. 14) measurements (there is no way to directly measure transmission since the thick silicon wafers efficiently absorb radiation in the relevant spectral region). Chemical and crystalline properties of the irradiated samples were studied using EDS, XPS and Raman analysis.

Raman spectra of the samples, patterned using DLIP technique with picosecond and nanosecond laser pulses, were measured. Fig. 17 shows Raman spectra of solar cell samples, patterned using picosecond and nanosecond setups. The intensity of the line at 520 cm^{-1} decreases with the increasing number of laser pulses. This shows that even the small number of pulses has a negative impact on the crystal structure of the silicon substrate. The emergence

of the line at 480 cm^{-1}, which corresponds to amorphous silicon, was also observed at large pulse numbers.

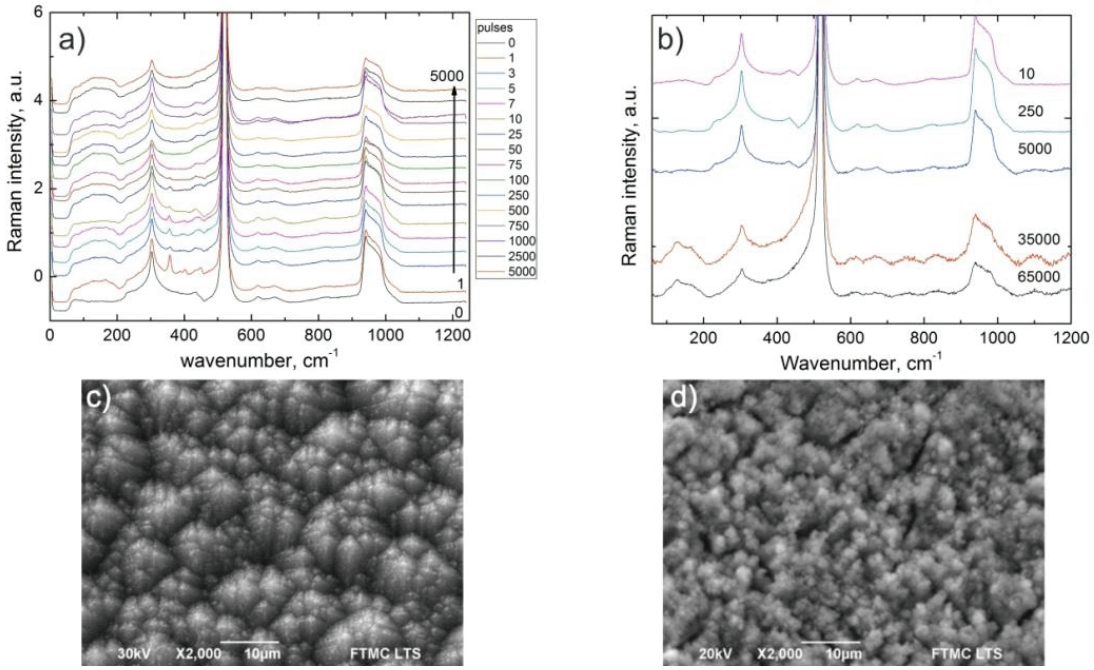

Fig. 17. Raman spectra of the laser patterned samples, using 60 ps (a)) and 35 ns (b)) pulses. Irradiation fluence in the interference maximum regions was 0.92 J/cm^2 for picosecond patterning and 0.84 J/cm^2 for nanosecond patterning. c) SEM image of solar cell textured using picosecond pulses, 1.26 J/cm^2, 500 pulses per spot. d) SEM image of solar cell textured using nanosecond pulses, 0.92 J/cm^2, 30000 pulses per spot.

Damage to the silicon substrate, caused by laser irradiation, was evaluated from Raman spectra. Samples textured using picosecond and nanosecond pulses using a various number of pulses per spot were analysed. Fig. 18 show ratio of the Raman line intensities at 520 and 480 cm^{-1}. It is evident that less than 100 pulses per spot do not change intensity ratio. Therefore, there is no major damage to the silicon substrate. Picosecond pulses produced less significant alteration on the Raman line intensity ratio than nanosecond pulses when laser fluencies and the pulse numbers were the same. This can be caused by greater thermal effect induced to the substrate by nanosecond pulses.

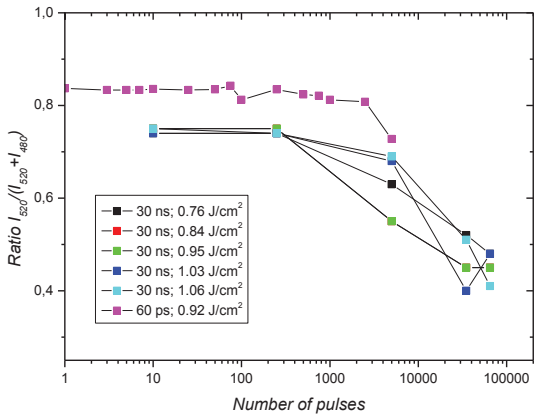

Fig. 18. Dependence of ratio of the integral intensity of the Raman lines at 520 and 480 cm^{-1}.

Next, I-V curves of the textured (using picosecond setup) solar cells were measured. Full solar cells were textured and measured using commercial solar imitator. Additionally, several solar cells were cut into smaller 60 x 40 mm^2 segments (retaining front and back contacts) to allow measurement in the setup constructed in the FTMC Department of Laser Technologies. This was required to obtain I-V curves immediately before and after laser texturing for process optimisation. In both cases, several lines were scanned between the contact grids to the pattern as large as the possible area of the passivation layer without damaging the contacts. Approximately, 70% of the area between the contact grid was patterned.

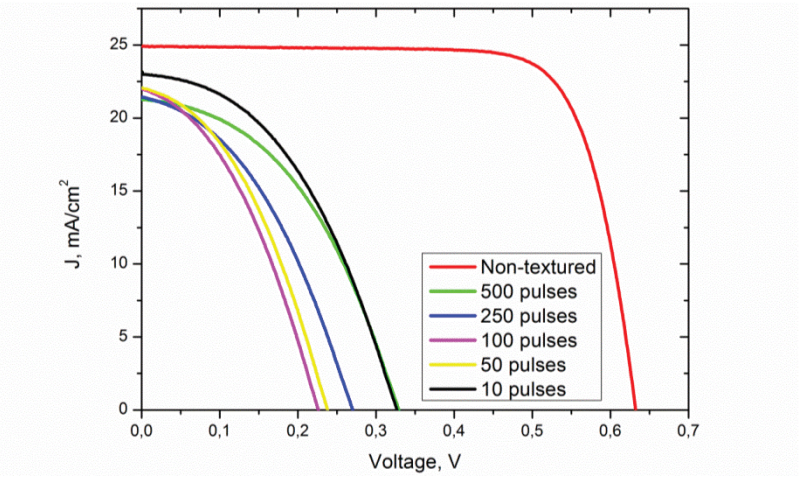

Fig. 19. Electrical characteristics of the full solar cell samples, textured using 2.5 µm 4-beam interference pattern with various pulse numbers. *J* is the current density. Irradiation fluence was 0.65 J/cm^2. The top curve corresponds to the non-textured sample.

All textured samples exhibited significantly reduced performance. About 50% drop of the V_{OC} values shows that surface recombination rate is significantly increased after the laser treatment. It may be caused by the removal of the passivating silicon nitride layer and defect formation in the silicon substrate. Therefore, comparison of Raman line intensities at 520 and 480 cm^{-1} does not unambiguously show laser-induced damage.

Further work was carried out using lower pulse energies, to avoid damaging silicon substrate below the SiN_x layer. Silicon nitride ablation threshold was measured using the Liu method [119]. The threshold fluence for ablation with the single 60 ps pulse was 0.34 J/cm^2. Fluencies close to this value were used in these experiments. The I-V characteristics of 60 x 40 mm^2 solar cell samples were measured before and after laser texturing. Ratios of the important parameters taken from the IV curves are provided in Table 4.

Table 4. Ratios of the parameters of 60 x 40 mm^2 solar cells after and before laser texturing. Letters T and NT denote textured and non-textured sample respectively.

Fluence, J/cm^2	Number of pulses	I_{sc}T/ I_{sc}NT	V_{OC}T/ V_{OC}NT	I_mT/ I_mNT	V_mT/ V_mNT	P_{max}T/ P_{max}NT	FF T/ FF NT	ηT/ηNT· 100%
0,35	1	0,993	1,000	0,982	1,000	0,982	0,989	98,196
0,35	5	0,995	0,890	0,840	0,788	0,662	0,748	66,245
0,35	10	0,997	0,801	0,805	0,679	0,546	0,684	54,649
0,24	10	1,011	0,997	0,999	1,007	1,006	0,998	100,583
0,24	25	0,994	0,967	0,958	0,921	0,883	0,919	88,295
0,14	25	1,008	1,004	1,004	1,007	1,011	0,999	101,137
0,14	100	0,999	1,000	0,990	1,007	0,997	0,999	99,734

Texturing with laser pulse energies not exceeding 0.34 J/cm^2 at interference intensity maxima did not result in a strong increase of carrier recombination. In several samples, short circuit current increased after laser texturing. This may

indicate increased light absorption due to laser irradiation. Efficiency ratios were calculated using the expression:

$$\frac{\eta_{textured}}{\eta_{non-textured}} = \frac{V_{OC}textured \cdot I_{SC}textured \cdot FFtextured}{V_{OC}non-textured \cdot I_{SC}non-textured \cdot FFnon-textured} \quad (7)$$

About 1.14% efficiency increase was obtained in the case of texturing with 0.14 J/cm^2 and 25 pulses. I-V graphs of several relevant samples are provided in Fig. 20.

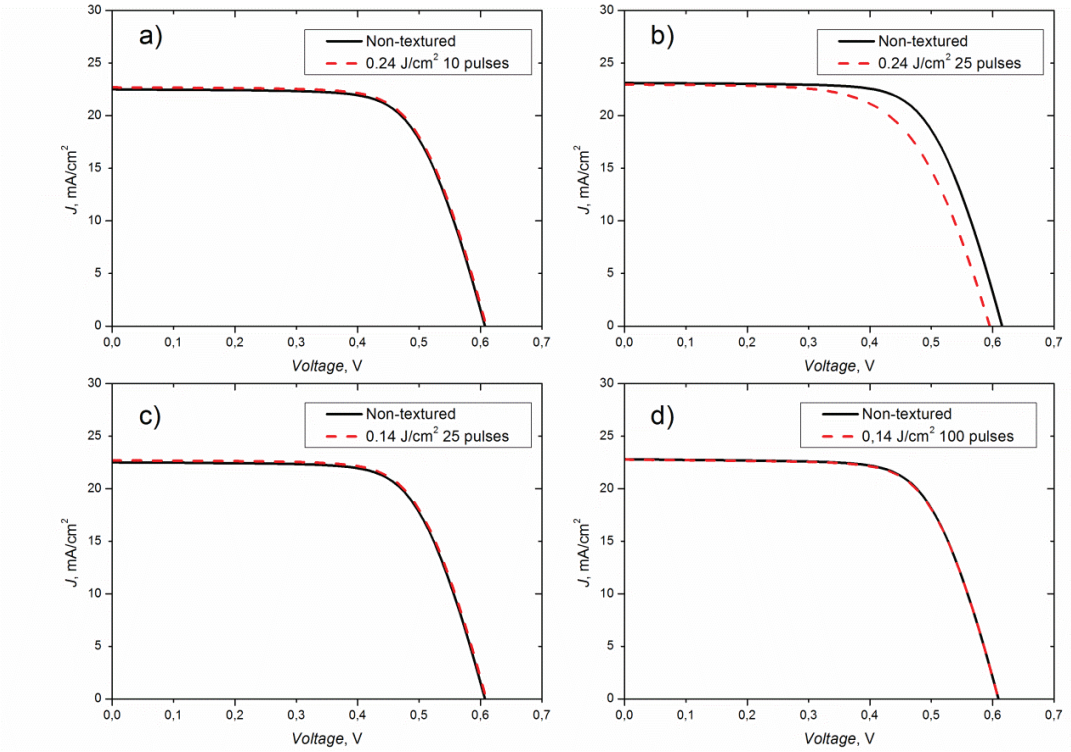

Fig. 20. I-V characteristics of full solar cell samples textured using 2.5 µm period 4-beam interference pattern with different pulse numbers and irradiation fluencies. Solid curve corresponds to the non-textured sample, dashed curve to the textured sample.

SEM images of the spots irradiated using different fluencies and pulse numbers per spot are provided in Fig. 21. Efficiency increase was found in the samples irradiated using low fluence. In those samples, no morphology change was detected in SEM images (Fig. 21e).

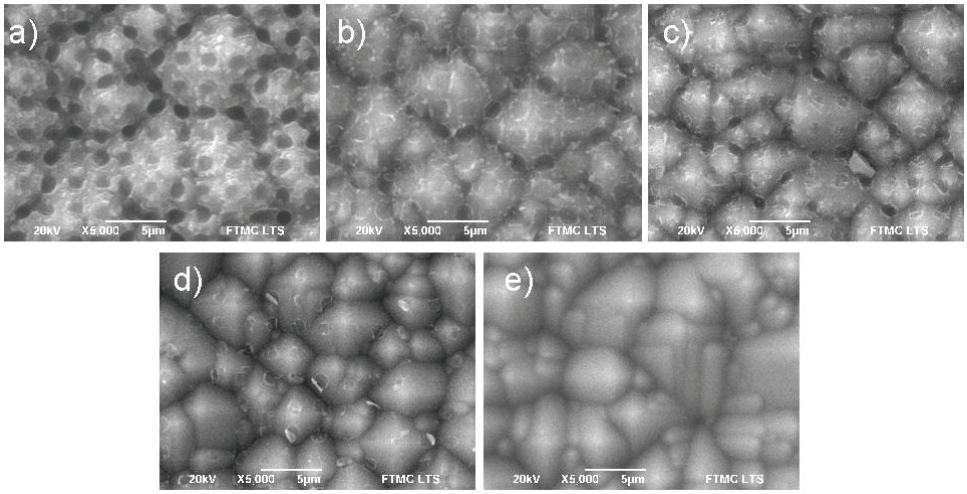

Fig. 21. SEM images of solar cell samples textured using 4-beam DLIP. a) – 1.5 J/cm^2 4 pulses; b) – 1.5 J/cm^2 1 pulse; c) – 0.65 J/cm^2 3 pulses; d) – 0.65 J/cm^2 1 pulse; e) – 0.14 J/cm^2 100 pulses.

However, the content of oxygen and nitrogen in the samples increased after irradiation with the low-energy laser pulses.

The EDS chemical element maps show that nitrogen and oxygen are distributed almost uniformly in the control sample (with no laser treatment). There are only some irregularities that can be explained by the geometry of the pyramidal surface. However, EDS analysis of the laser-irradiated sample shows locally increased oxygen concentration after the irradiation (Fig. 22a)). Periodic oxygen distribution with the same period as the interference pattern was obtained (Fig. 22d). Therefore, the conclusion can be made that silicon nitride layer was oxidised in the regions with the highest laser irradiation intensity. In the nitrogen EDS map, more regions with low nitrogen content can be observed compared to the untreated sample. However, no evident correlation between interference intensity pattern and nitrogen distribution is apparent. XPS analysis of the samples treated using various pulse energies shows that oxygen and nitrogen content decreases for the high-pulse-energy (150 μJ) patterning regime when the passivation layer is ablated at the intensity peak regions. For lower pulse energies, when no visible damage to the passivation layer takes place, relative oxygen content O/Si is increased, and relative content of nitrogen N/Si remains similar as in the untreated sample.

This suggests that low energy pulse induces oxidation process but does not ablate the material.

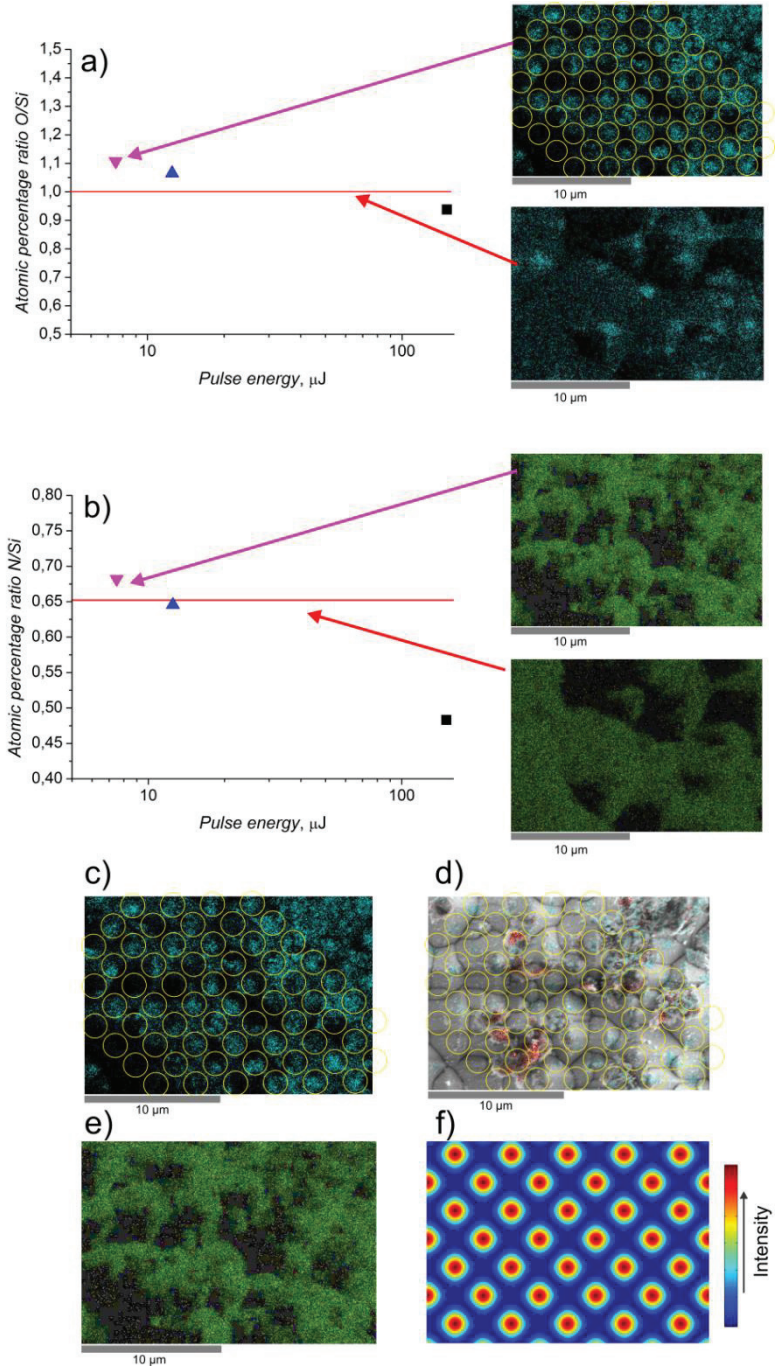

Fig. 22. EDS and XPS data of untreated and laser-irradiated polycrystalline silicon solar cell samples. The ratio of atomic percentage of silicon to oxygen (a) and silicon to nitrogen (b) on the peak laser fluence, measured by XPS. c) and d) show EDS oxygen map and EDS oxygen map overlaid on the SEM image (sample irradiated with 0.14 J/cm^2, 1 pulse). e) EDS nitrogen map of the sample irradiated with 0.14 J/cm^2, 1 pulse f) – simulated intensity distribution of the 4-beam interference pattern.

Formation of oxide after the laser irradiation can also be seen in the Raman spectra (Fig. 21). Raman peak between 400 and 500 cm^{-1} corresponds to the Si-N bond [120]. It is strong in the non-patterned sample and in the sample irradiated using a low number of pulses, but the peak is reduced when silicon nitride layer is ablated with a large number of pulses. The Raman peak at 356 cm^{-1} may be attributed to the silicon dioxide [121]. Its intensity is also the largest after irradiation with a single pulse (Fig. 17a).

Diffuse reflectance spectra are provided in Fig. 23. Quantity *K,* proportional to the absorption coefficient, was obtained from the diffuse reflectance spectra using Kubelka-Munk transform [122]:

$$K = \frac{(1 - R_d)^2}{2R_d} \tag{8}$$

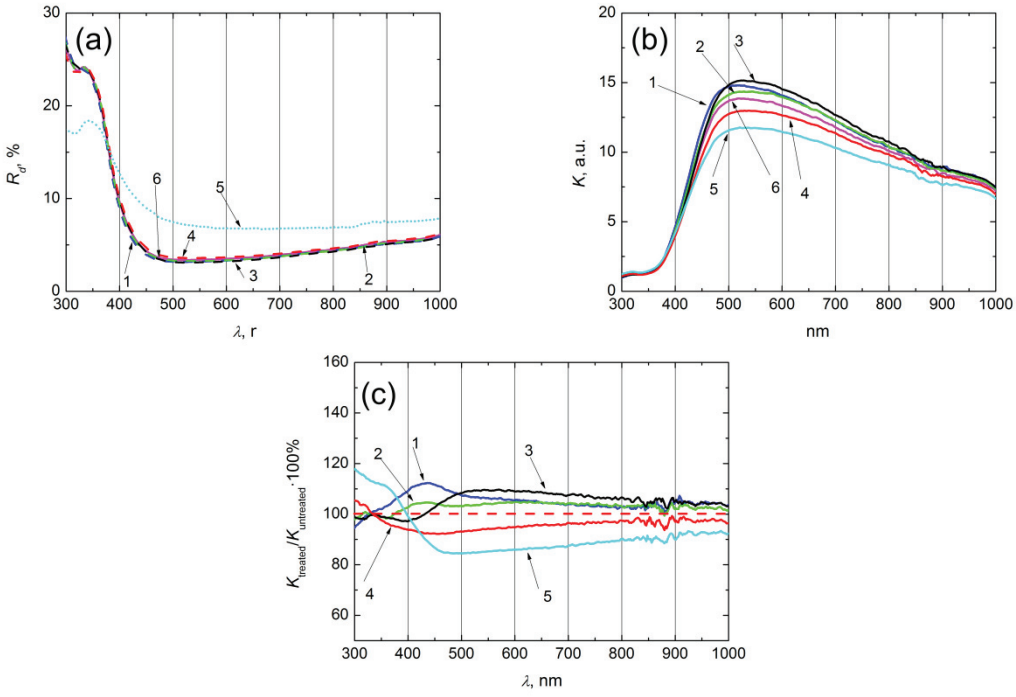

Fig. 23. Dependence of the reflection coefficient R_d (a), and absorption coefficient K (in arbitrary units) (b) on the wavelength λ. Laser treated (1 – 5) and untreated (6) samples are compared. Comparison of absorption coefficients K of the laser treated and untreated (100%) samples in the 300 – 1000 nm spectral range (c). Laser irradiation fluence: 1 – 0.08 J/cm^2; 2 – 0.14 J/cm^2; 3 – 0.28 J/cm^2; 4 – 0.57 J/cm^2; 5 – 0.84 J/cm^2; 6 – no laser treatment. All samples were patterned with one laser pulse.

In the optical properties measurements, two modification regimes are apparent. For low laser fluencies, the reflectivity decreased, and absorption increased in the 400 – 1000 nm region almost uniformly. For higher fluencies, the reflectivity reduction in the 300 – 400 nm region and its increase in the remaining region was observed.

Increased absorption may be a result of the periodical refractive index modification (SiO_x/SiN_xO_y grating), induced by the irradiation with a modulated laser beam. Fig. 24 shows a simulation of the reflectance from periodic (4 µm period) pyramid structure with SiO_x/SiN_xO_y grating. The simulation shows reduced reflectance in the 0.3 – 0.55 µm region, due to the grating. This result is not completely in agreement with the experimental results. However, it shows that periodical SiO_x/SiN_xO_y grating at least partially is responsible for the increased absorption in the samples prepared using low laser fluence.

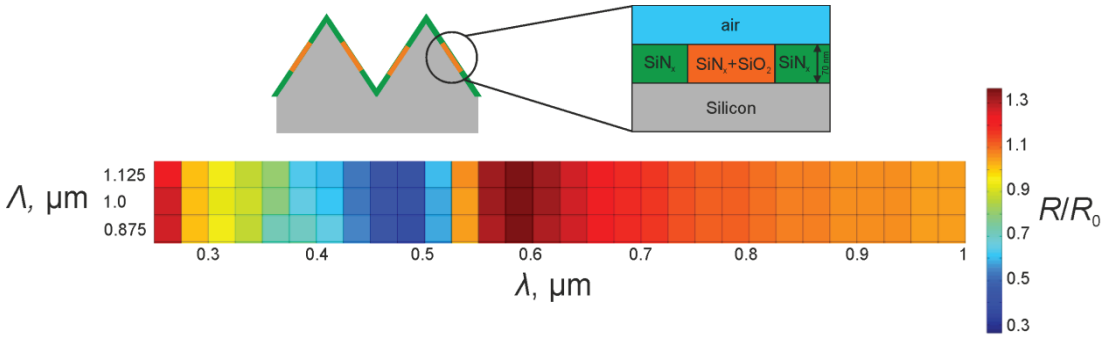

Fig. 24. The ratio of the reflectance from periodic pyramid structure with silicon nitride/ oxynitride grating *R* with the reflectance from the silicon pyramids with the uniform silicon nitride layer R_0.

Modification of the silicon nitride layer is preferable to the ablation. Laser ablation of silicon nitride layer affects the lifetime of minority carriers. Ablation with nanosecond pulses was shown to reduce carrier lifetime [123]. However, femtosecond pulse irradiation provided no significant impact on the lifetime [124]. Modification using fluence values below the threshold allows minimising any damage to the silicon layer.

4.1 Conclusions

- DLIP processing using laser irradiation fluence in the interference intensity maxima below the silicon nitride ablation threshold induces periodically arranged silicon oxide/ oxy-nitride islands in the passivating silicon nitride layer.
- Silicon oxide/ oxy-nitride islands act as a refractive grating, and it facilitates light absorption in the solar cell.
- The efficiency of the laser processed solar cells was increased by 1±0.6%.

5 Formation of Inverted Pyramids in Monocrystalline Silicon Using Laser Interference Patterning and Anisotropic Wet Chemical Etching

The material, related to this chapter was published in [A8], [C3], [C5], [C12].

In the monocrystalline silicon solar cells, the light losses due to reflection can be significantly reduced, and the light optical path in the cell increased using inverted pyramid patterns [125]. Fabrication of such patterns is usually performed utilising anisotropic chemical etching through the mask. DLW and DLIP followed by etching in KOH solution could have an advantage of being mask-less methods and were demonstrated as a viable method for inverted pyramid pattern fabrication in silicon [126, 127]. In this chapter, the influence of irradiation fluence and wavelength on the depth and morphology of inverted pyramid structure is discussed. The role of amorphous silicon and silicon oxide layers, formed due to the effect of laser irradiation, is analysed.

The periodic structure of inverted pyramids was formed using 2 μm period DLIP to pattern the surface of the crystalline (100) silicon wafer. Patterned wafer was chemically etched using an anisotropic etchant. The silicon surface was ablated using the second and third harmonics (532 nm and 355 nm) of the Atlantic HE sub-nanosecond laser. DLIP system is shown in Fig. 11b. All experiments were performed in air. The ablation with various pulse energies and pulse numbers per spot was performed. After the laser processing, samples were immersed in 10% potassium hydroxide (KOH) solution for 3 hours at the room temperature (Fig. 25).

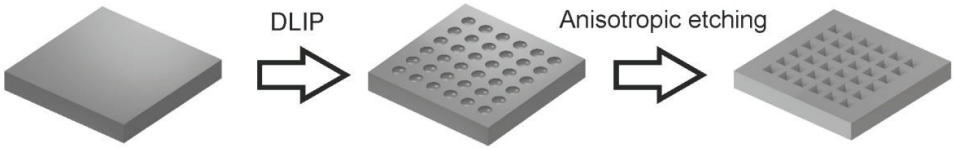

Fig. 25. Fabrication steps for the inverted pyramid structure.

Morphology of the resulting inverted pyramid pattern was investigated using scanning electron microscopy (SEM) and atomic force microscopy (AFM). Changes in the crystalline structure were analysed using Raman spectroscopy. Elemental analysis of the sample was performed using the EDS technique.

The angle between the silicon surface and wall of the pyramid is determined by the angle between silicon (100) and (111) planes and is 54.7 °. Therefore, for a specific pyramid base width, maximal depth of the pyramid is:

$$Depth = \frac{Width}{2}\tan(54.7) \tag{9}$$

5.1.1 532 nm irradiation

SEM images of the silicon samples irradiated using the 4-beam interference intensity distribution with the 532 nm wavelength before and after the etching process are provided in Fig. 26. Samples were patterned using a single laser pulse and various fluence values.

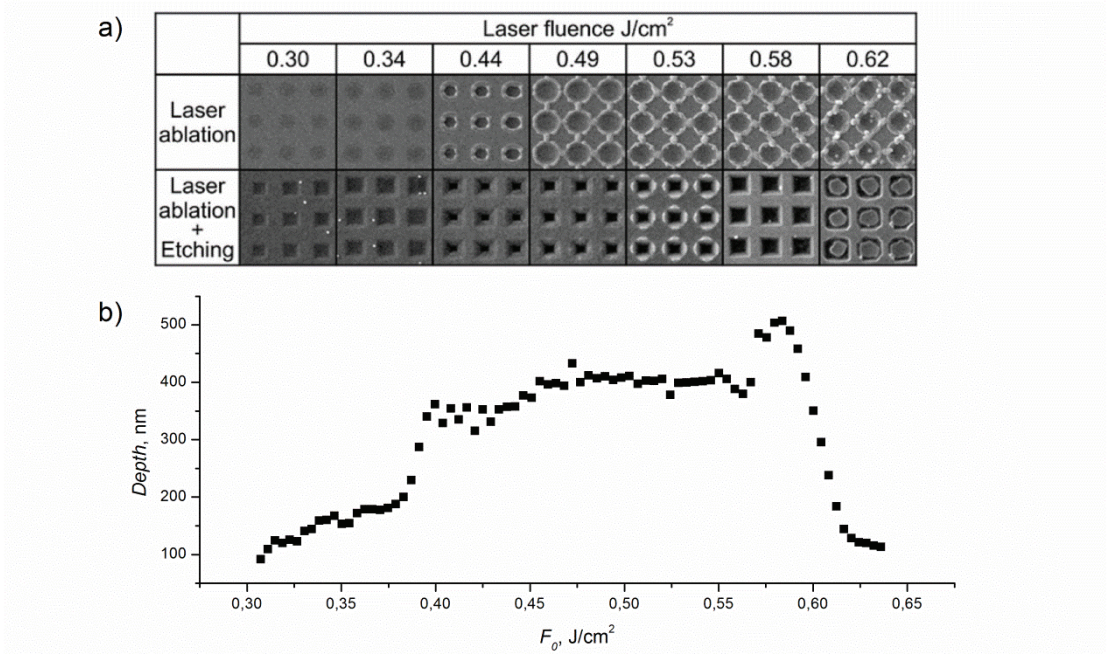

Fig. 26. a) SEM images of the interference-patterned silicon before and after the KOH etching (patterning was performed with a single laser pulse, using the 532 nm wavelength); b) dependence of the final structure depth on the irradiation fluence.

The round shaped periodically distributed pits ablated using DLIP with 532 nm wavelength were transformed into the square-shaped pits after the etching

process. The depth of the structure was measured using AFM. The structure depth strongly depended on the irradiation fluence and reached its maximum value at a relatively narrow fluence range around 0.58 J/cm^2. The height differences between the top and bottom pyramid surfaces for various fluencies are provided in Fig. 26b. The depth of the structure increases with growing fluence and reaches a maximum value at 0.58 J/cm^2. When the laser fluence becomes higher than 0.6 J/cm^2, the centre of the pyramid area is etched slower than the outer area. This resulted in a hill formed in the pyramid centre. Additional investigation shows that etching occurs not only at the maximum irradiation spots but also between the pyramids. Fig. 27a provides a comparison of the heights of the zones between the pyramids and at the bottom of pyramids. The surface between the pyramids is practically at the constant level until fluence reaches 0.58 J/cm^2 value. When fluence increases above this value, the etching rate drastically decreases (height of the surface between the pyramids grows by 200 nm). This result leads to the conclusion that when the laser fluence is high enough (> 0.58 J/cm^2), the material between interference maxima is modified in the way that slows down the etching.

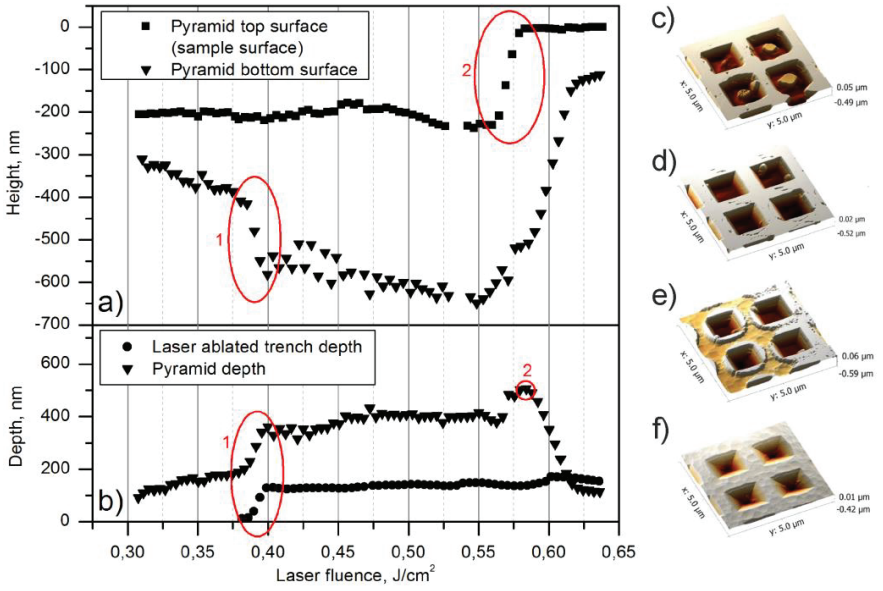

Fig. 27. a) Heights of the surface between the pyramids and pyramid bottom surface; b) comparison of laser ablated structure depth and depth of the same structure after the etching; c) – f) – AFM measured pyramid topographies at different laser fluencies (c) –0.61 J/cm^2, d) – 0.58 J/cm^2, e) – 0.56J/cm^2, f) – 0.4 J/cm^2).

Furthermore, when the fluence exceeds 0.58 J/cm^2, another modification, preventing the etching in the centre of the pyramid, occurs. These results suggest that some layer with a low etching rate in KOH solution is formed between the maximum irradiation spots when irradiation fluence is sufficiently high. Therefore, the formation of silicon oxide and amorphous silicon layers using 300 ps laser pulses was investigated. Both of these materials can be produced on the silicon surface using laser irradiation [128, 129]. Also, their etching rate in KOH solution is significantly lower than the crystalline silicon etching rate. The (100) silicon etching rate in 10% KOH solution at 20 °C is 1.49 μm/h [130]. SiO_2 etching rate in 20% KOH solution at 20 °C is 1 nm/h [130]. The amorphous silicon etching rate in 10% KOH solution was reported to be 30 times lower than that of (100) silicon [131]. Amorphous silicon content was evaluated using Raman spectroscopy. Both interference-formed microstructure samples and relatively large (about 0.5 mm spot diameter) areas irradiated with a single laser beam were investigated. Fig. 28 shows ratios of Raman line intensity at 520 and 480 cm^{-1} superimposed on the optical microscope images of irradiated areas. It is evident that light coloured zone in the optical microscope image corresponds to the amorphous silicon. The absence of such zones in the centres of the irradiation spots suggests that amorphous silicon is recrystallised [132] when irradiation fluence exceeds a certain threshold. Using the Liu method [119], the fluence thresholds for formation and elimination of amorphous silicon layer were evaluated: 0.19 J/cm^2 for the formation and 0.26 J/cm^2 for elimination, respectively. These values are in agreement with the silicon amorphisation and recrystallisation thresholds for the 532 nm picosecond laser pulses found in the literature [119, 128]. This result suggests that amorphous silicon formation does not affect the inverted pyramid fabrication process because formation/elimination threshold fluence is lower than 0.58 J/cm^2. This conclusion can be reasserted from the Raman spectra of the fabricated inverted pyramid arrays (Fig. 28d). There is no intensity increase of the 480 cm^{-1} line.

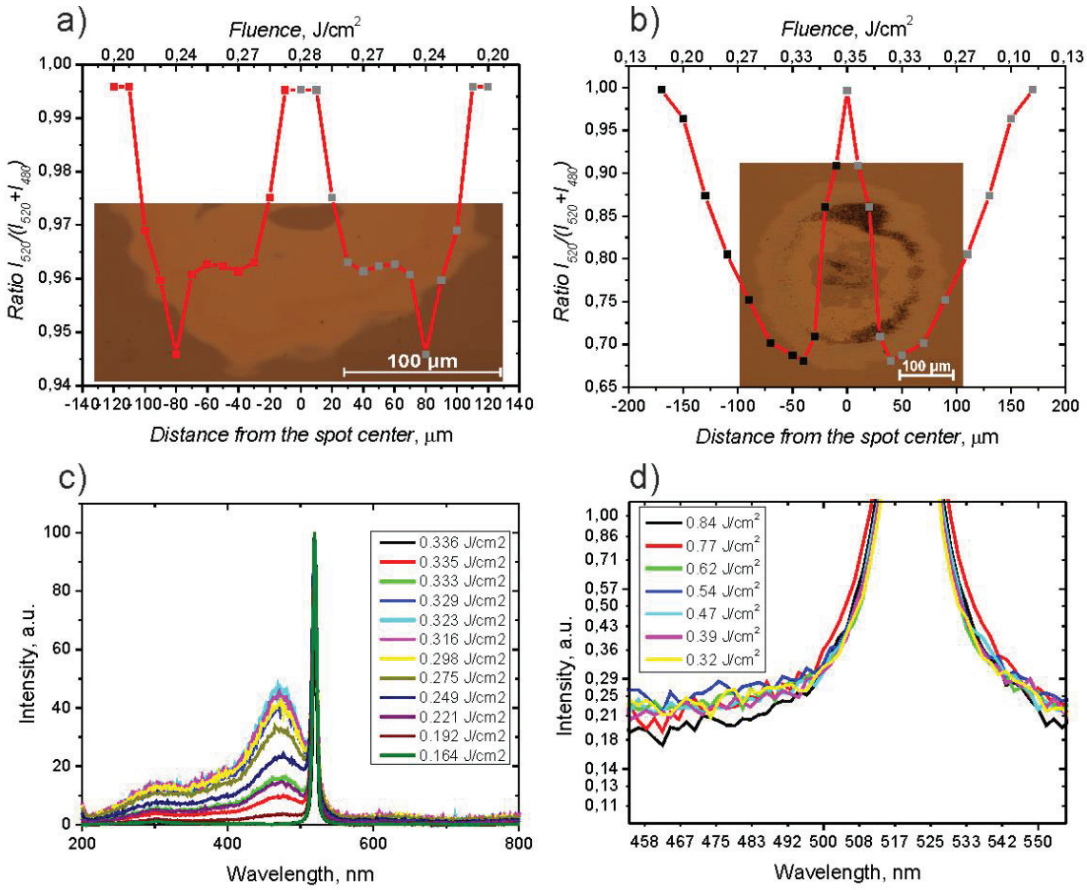

Fig. 28. a) Dependence of ratio of Raman line peak intensities at 520 and 480 cm^{-1} on irradiation fluence at spot irradiated with single laser beam, 3 pulses per spot; b) dependence of ratio of Raman line peak intensities at 520 and 480 cm^{-1} on irradiation fluence at spot irradiated with single laser beam, 25 pulses per spot; c) Raman spectra of single beam irradiated areas at different fluencies, 25 pulses per spot; d) Raman spectra of 4-beam interference irradiated areas at different fluencies, 1 pulse per spot

Silicon oxide content in the laser-irradiated samples was investigated using the EDS spectroscopy. Results are provided in Fig. 29. For the 532 nm irradiation wavelength oxygen content significantly increases in $0.4 - 0.6$ J/cm^2 fluence range (Fig. 29a). This is in agreement with AFM measurements, that showed starting fluence for the etch-resistant layer formation to be at around 0.56 J/cm^2 (Fig. 27).

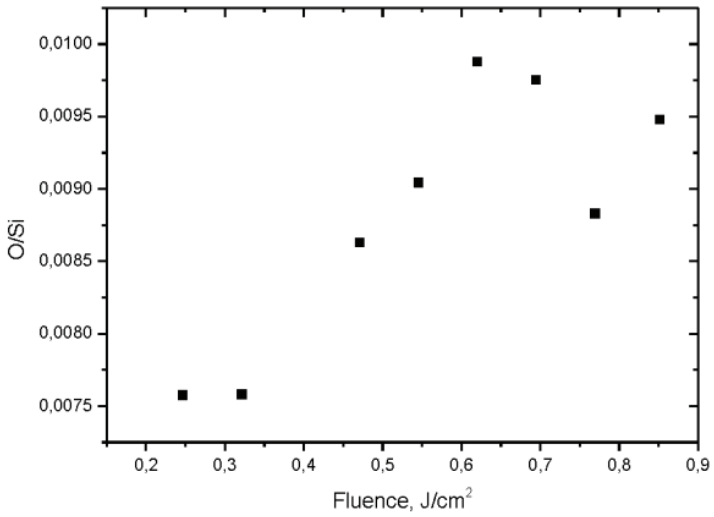

Fig. 29. Oxygen/Silicon content ratio in the interference-patterned and etched silicon samples (2 pulses per spot for the 532 nm irradiation wavelength).

Additionally, the impact of the pulse number per spot on the morphology of the fabricated pyramids was investigated. Increased pulse numbers led to the increased depth of the structures. Fig. 30 shows the dependence of the etched pyramid depth on the number of laser pulses.

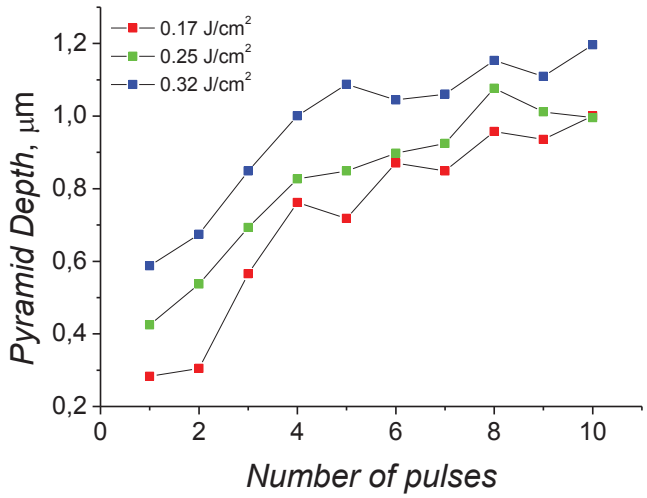

Fig. 30. Influence of a number of pulses on the etched pyramid depth. Irradiation wavelength was 532 nm.

5.1.2 355 nm irradiation

Ablation using DLIP with the 355 nm wavelength resulted in the pit structure, similar as for ablation with the 532 nm wavelength. Silicon samples were irradiated using 2 µm period 4-beam interference intensity distribution. Samples were etched for 300 s at room temperature. After the etching step, in the low fluence regime, shallower pyramids are formed than in the case of the 532 nm irradiation (Fig. 31c). However, when laser fluence used for patterning was increased, column structure was formed at the maximum intensity spots.

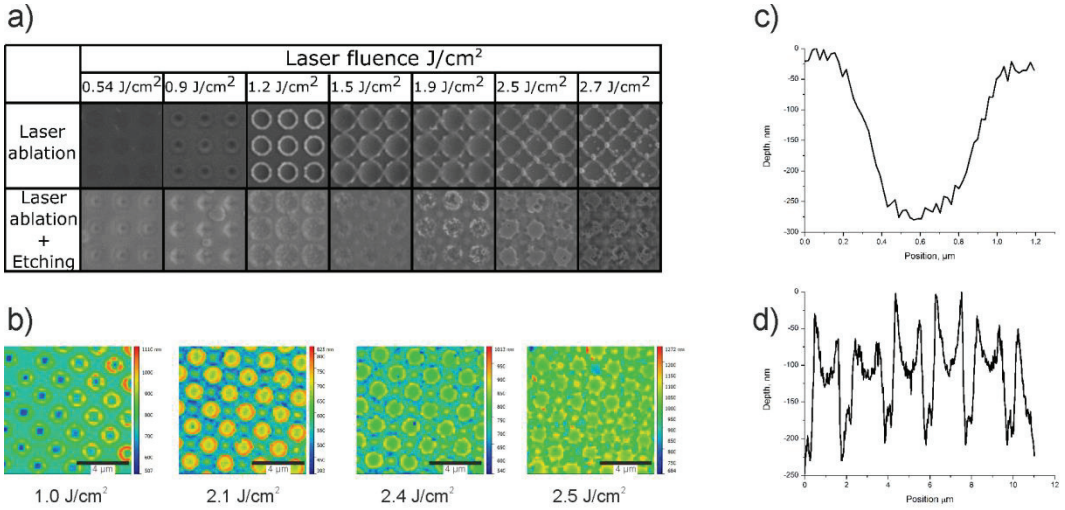

Fig. 31. a) SEM images of the interference-patterned silicon before and after the etching step; b) height maps obtained using AFM; c) a profile of the pyramid obtained using 1.0 J/cm^2 fluence; d) a profile of the column structure, obtained using 2.5 J/cm^2 fluence.

As in the case of the 532 nm irradiation, the pulse number per spot has a significant influence on the morphology of the etched structure. Using 10 pulses per spot, pyramids with a sharp profile and with the depth to width ratio close to the limit value (Eq. (9)) was obtained (Fig. 32).

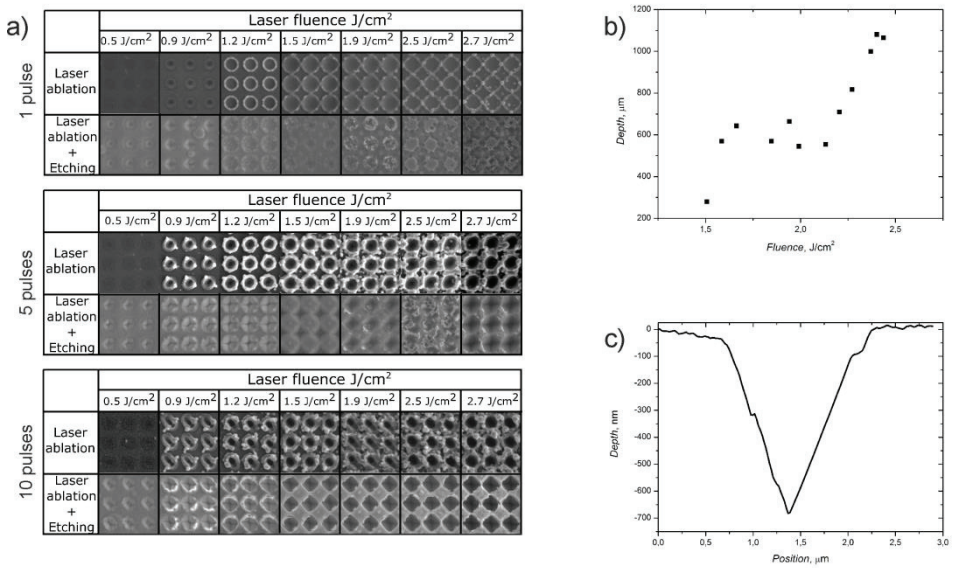

Fig. 32. a) Comparison of SEM images of structures obtained using different pulse numbers per spot; b) pyramid depth dependence on irradiation fluence (10 pulses per spot); c) profile of the pyramid fabricated using 1.9 J/cm^2 and 10 pulses per spot.

EDS analysis showed an increase of the O/Si ratio with the increasing pulse numbers (Fig. 33a). That increase may be attributed to the growth of the oxide layer between the maximum irradiation spots. As in experiment with the 532 nm wavelength, no significant change in the crystal structure of silicon was detected using Raman spectroscopy (Fig. 33b).

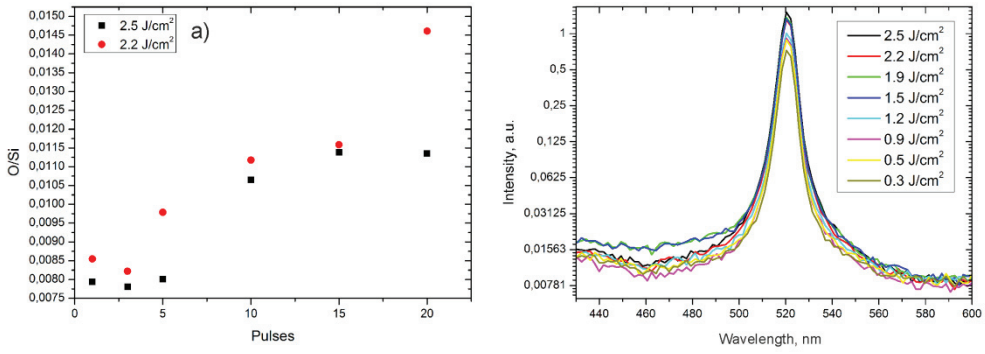

Fig. 33. a) Dependence of oxygen and silicon ratio on the number of pulses; b) Raman spectra of the inverted pyramid structure.

The depth-to-width ratios (Eq. (9)) of pyramids fabricated using various laser fabrication parameters are shown in Fig. 34. Using multi-pulse regime, the optimal depth-to-width ratio can be achieved.

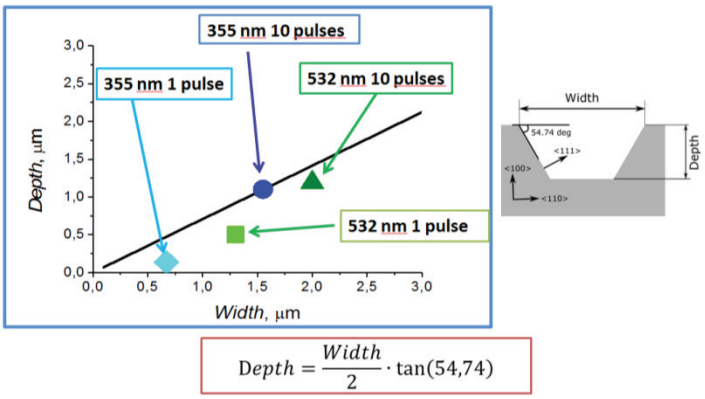

Fig. 34. Depth to width ration of inverted pyramids formed using the laser interference ablation and wet chemical etching. The solid line represents the optimal depth to width ratio.

Therefore, the inverted pyramid formation process with respect to the irradiation conditions for both wavelengths can be summarised as follows:

- When irradiation fluence is relatively low, shallow pyramids with the width to depth ratios far to the limit are formed (Fig. 35a).
- When the fluence increases, silicon oxide islands are produced in the maximum intensity spots (Fig. 35b).
- When the fluence further increases, silicon oxide layer in the maximum intensity spots is damaged, and oxidation starts to take place in the intensity minima (Fig. 35c).
- If several pulses per spot are applied, the silicon oxide layer at the maximum intensity spots is removed, but areas between the ablated craters are oxidised. In this case, oxide layer acts as an etching mask for the pyramids (Fig. 35d).

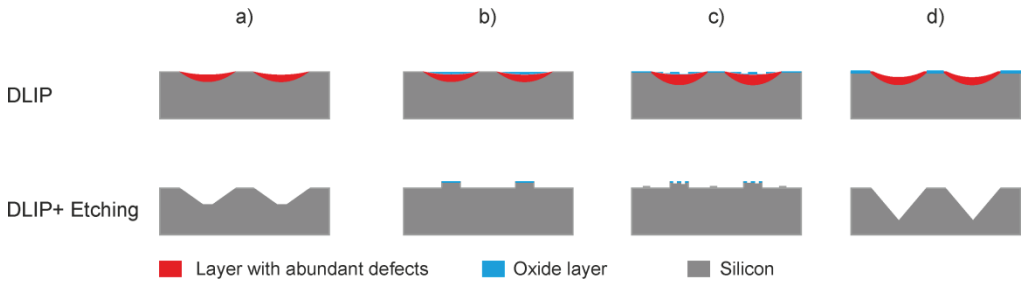

Fig. 35. Inverted pyramid formation using DLIP and wet chemical etching.

5.1.3 Conclusions

1. Using DLIP in the air and anisotropic wet chemical etching, the structure of periodically inverted pyramids can be fabricated in silicon. Oxidation of silicon surface due to laser irradiation is a crucial factor in the fabrication process.
2. Silicon oxide layer is formed on silicon due to the effect of laser interference irradiation. Depending on the irradiation conditions, this layer is created only at the maximum fluence regions or in the entire irradiated area including the minimum fluence regions. Certain irradiation conditions (multi-pulse regime) result in the absence of the oxide layer at the maximum fluence regions.
3. The oxide layer acts as an etching mask and positively affects the formation of inverted pyramid pattern if it is formed on the entire irradiated area except for the maximum fluence regions. A multi-pulse regime with no less than 10 pulses per spot was found to be the most suitable for the fabrication of inverted pyramid pattern.

6 Fabrication of Periodic Surface Structures in Multicrystalline Silicon Using Direct Interference Ablation and Isotropic Wet Chemical Etching

The material, related to this chapter was published in [A5], [A8], [C1], [C5], [C6], [C10], [C12].

6.1 Simulation of the 2D dimple gratings in silicon

Two-dimensional gratings in silicon were simulated using COMSOL Multiphysics modelling software. Modelling setup is provided in Fig. 36. The Floquet boundary conditions were used to describe periodicity of the structure. Electromagnetic wave was excited inside the modelling domain (port). Only the reflected wave reached the top part of the section, containing air. Geometry was closed using absorbing layers (perfectly matched layers (PMLs)) on both ends.

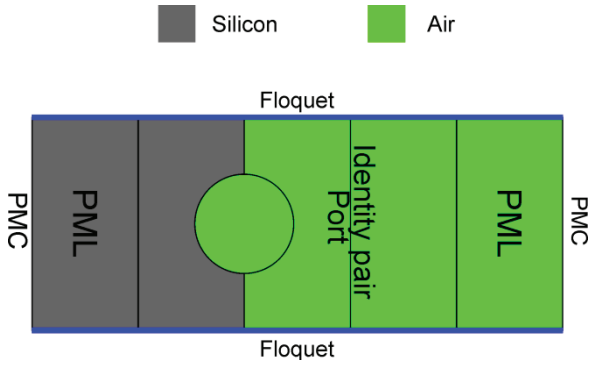

Fig. 36. Setup for COMSOL simulations.

Antireflective properties of elliptical cavities in silicon were evaluated for the p-polarized radiation. Influence of the cavity depth and width on the reflectance spectrum and angular reflectance spectrum was investigated (Fig. 37). Peaks and dips at the 0.95 – 1 μm and 0.6 – 0.7 μm wavelengths may be attributed to the Rayleigh-Wood anomaly. 2^{nd} to 3^{rd} order Rayleigh anomaly wavelengths for the 2 μm period grating at normal incidence are 1 μm and 0.66 μm, respectively [133].

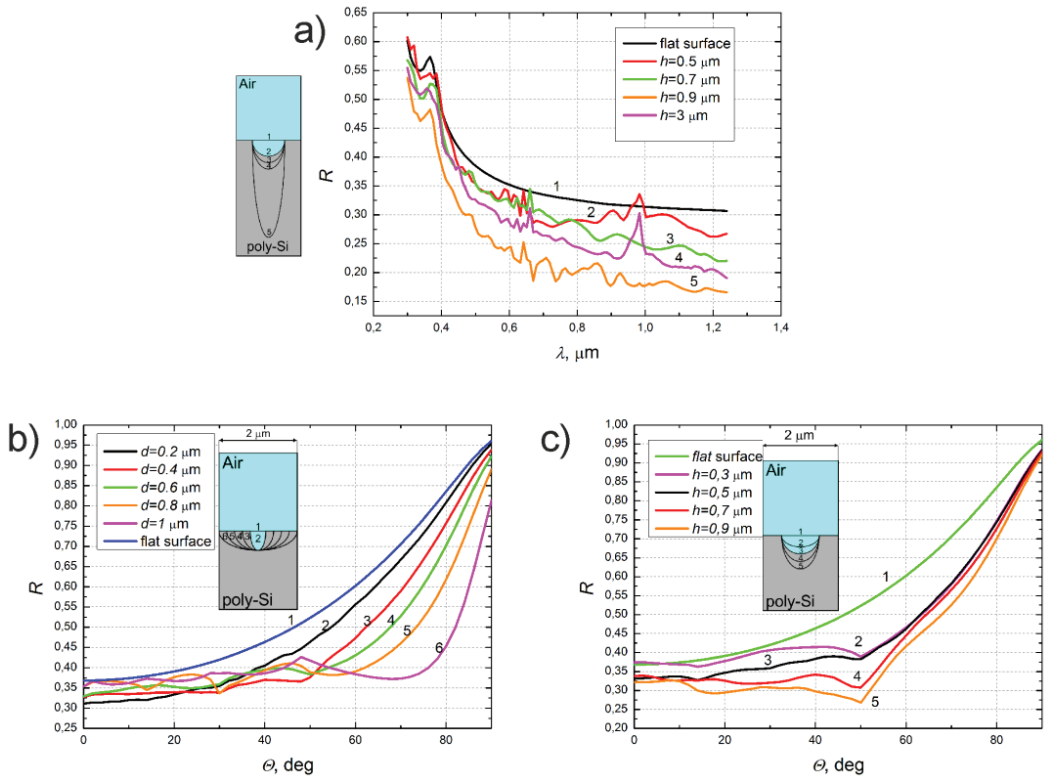

Fig. 37. Simulated reflectance dependencies on the radiation wavelength and angle of incidence for the 2 μm period structures. a) – reflectance dependence on the irradiation wavelength for various cavity depths h. Cavity width 1 μm, the radiation angle of incidence 0 deg; b) – reflectance dependence on the angle of incidence for different cavity widths d. The depth of the cavities 0.5 μm. Radiation wavelength 500 nm; c) – reflectance dependence on the angle of incidence for various cavity depths h. Cavity width 1 μm, radiation wavelength 500 nm.

Influence of the structure period on the reflectance was also investigated. Fig. 38 shows reflectance simulation (for the 500 nm wavelength) of the fixed depth (0.5 μm) structure for various periods and cavity widths.

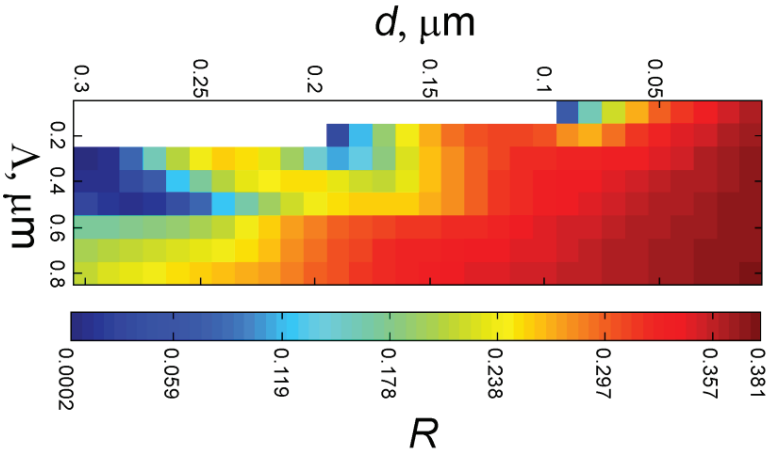

Fig. 38. Simulated dependence of the reflectance *R* on the structure period *Λ* and cavity width *d* for the 500 nm wavelength. Cavity depth is 0.5 μm, angle of incidence 0 deg.

From Fig. 37a and Fig. 38, it can be concluded that for the maximal antireflective effect, the width of the structure should be maximal for a given structure period and the depth/width ratio should be close to unity or higher. Reflectance at large irradiation angles is minimised when the width of the structure approaches the structure period value. Positive effect can be observed, when the period of the structure is smaller than the irradiation wavelength (Fig. 38).

6.2 Experiment

Multicrystalline silicon wafers were polished in KOH (IE1) or acid (IE2) solution to remove a surface layer, damaged during wafer cutting. Polished wafers were patterned using the 4-beam interference setup (Fig 6b Section 3.1). The second and third harmonics of the sub-nanosecond laser Atlantic HE were used. Most of the results were produced using the 2 μm pattern period. Additionally, structures with 1 μm, 0.6 μm and 0.4 μm periods were fabricated. The 2 μm, 1 μm and 0.6 μm period structures were fabricated using the 532 nm wavelength. The 0.4 μm period structure was fabricated using the 355 nm wavelength because shorter wavelength was needed to obtain such a small period. Additional chemical etching step using etchant E3 was applied to clean oxide, formed during the processing and to remove an upper surface layer, containing irradiation-induced defects. The etching parameters are described in more detail in Section 3.2.

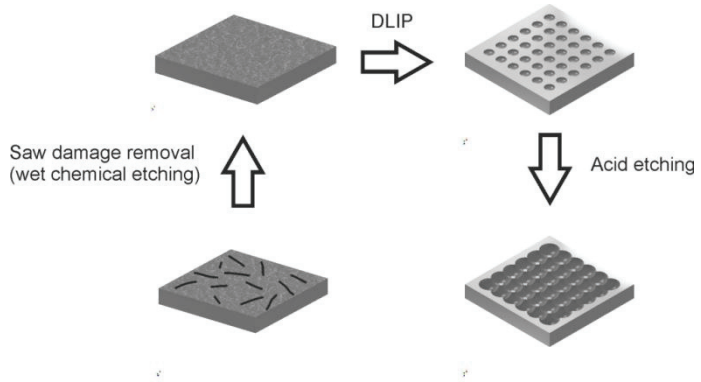

Fig. 39. Steps for periodic pit array fabrication using DLIP and wet chemical etching.

Impact of the pulse number per spot and etching duration on the reflectance of the patterned samples was studied. In Fig. 40, there are shown SEM images of samples patterned using the 2.67 J/cm^2 irradiation fluence and various numbers of pulses per spot.

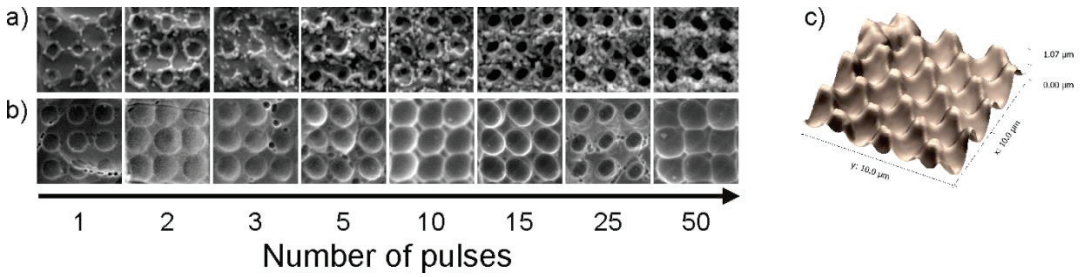

Fig. 40. SEM images of the interference-patterned multicrystalline silicon samples, before (a) and after (b) the final acid etching step (90 s etching duration); c) AFM profile of structure obtained using 10 pulses.

The depth of the fabricated pits was measured using a confocal optical profiler. The maximal depth of the ablated structure reached 1.1 μm (about 0.5 of the structure period) with the pulse numbers exceeding 25. The depth dependence on the pulse number for the etched samples remained similar. However, when pulse number was increased, the height of the walls between pits decreased compared to the non-etched sample (profile A in Fig. 41b). This is not preferable result because low sidewalls reduce the possibility for multiple reflections in the structure.

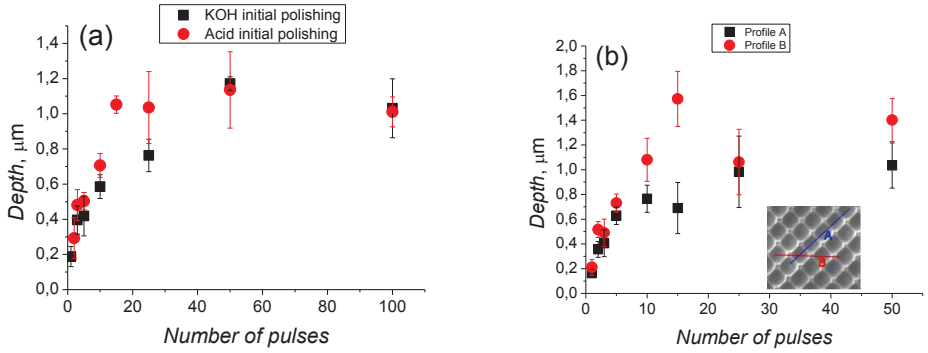

Fig. 41. Dependence of the structure depth on the number of laser pulses for laser patterned (a) and laser patterned and etched (b) multicrystalline silicon samples.

Influence of the etching duration on the depth of the structure was also investigated. Measured pit depths for various etching durations are provided in Fig. 42.

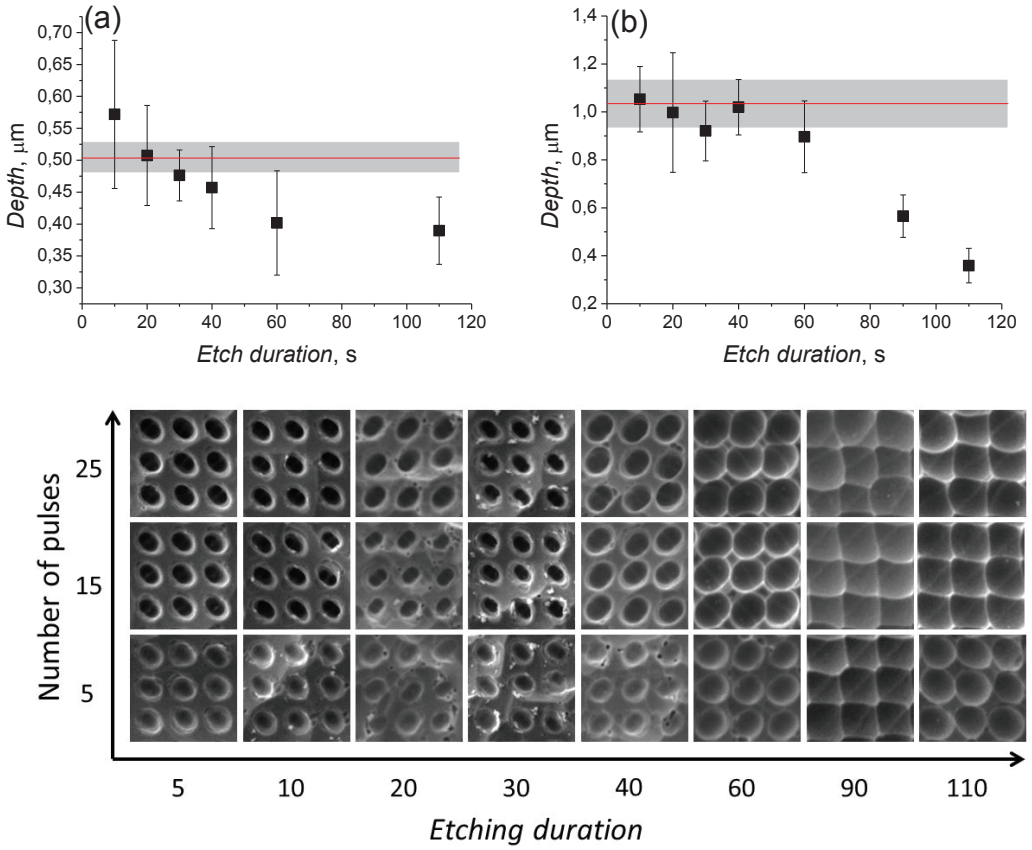

Fig. 42. Dependence of the structure depth on the etching duration. (a) Structure, fabricated using 5 pulses per spot; (b) – 25 pulses per spot. Red line shows the depth of the structure before the etching step (the grey band is measurement error).

When the etching time increases, the depth of the structure decreases. However, a non-useful planar area between pits also decreases. Therefore, there should exist an optimal etching duration for reflectance reduction.

To evaluate the anti-reflective performance of fabricated structures, reflectance spectra of the interference-patterned samples were compared with the reference pattern used in industrial multicrystalline solar cells. The reference sample was obtained by omitting laser patterning step in the fabrication process. The total reflectance (diffusive + specular) was measured using an integrating sphere (Section 3.3). The reflectance spectra of the samples prepared using various pulse numbers, and etching durations are provided in Fig. 43. For the constant

etching time, the lowest reflectance values were obtained using more than 25 pulses. That corresponds to the highest structure depths after the etching. For the fixed pulse number per spot, the lowest reflectance values were achieved for a moderate (40 – 60 s) etching time. Short etching durations provided deeper structure, but the considerable area between the pits remained planar. On the other hand, the long etching durations reduced the planar areas, but also reduced the wall height between the pits. Therefore, impinging light ray has a lower probability of experiencing multiple reflections from the structure. At the optimal etching duration, the reflectance as low as 17.5% was achieved in the 700 – 1000 nm spectral range.

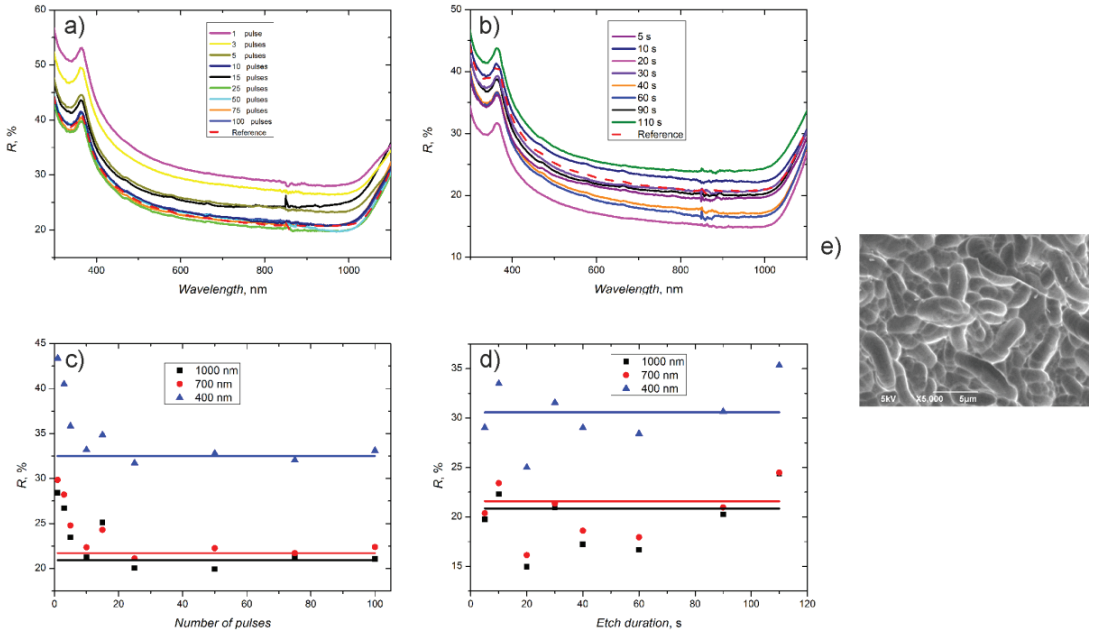

Fig. 43. The reflectance of multicrystalline silicon samples, patterned using DLIP and wet chemical etching. Irradiation fluence for all samples was 2.67 J/cm^2. a) dependence of reflectance on number of laser pulses per spot (etching duration 90 s); b) shows dependence of reflectance on etching duration (samples were fabricated using 25 pulses per spot); c) – reflectance dependence on the number of pulses for 400 nm, 700 nm and 1000 nm wavelengths; d) reflectance dependence on the etching duration for 400 nm, 700 nm and 1000 nm wavelengths. The reflectance of laser patterned samples is compared with the reference sample (dashed lines in a) and b) and solid lines in c) and d)); e) SEM image of the reference sample. During the reflectance measurements sample was oriented at 8 deg to irradiation direction.

As our simulations showed, the best antireflective properties can be obtained when the depth/width ratio of the structure is large, and the width of a pit is approaching the structure period. Experiments showed that the structure depth

was limited to about half of the period, and the optimal pit width was achieved by selecting an appropriate etching duration. Therefore, in further experiments, the influence of the pattern period on the reflectance was evaluated. Patterns with 1 µm, 0.6 µm and 0.4 µm periods were fabricated using various pulse numbers per spot and etching durations. The reflectance of these patterns was measured and compared with the reflectance of the 2 µm period structure. Results for several wavelengths are provided in Fig. 44.

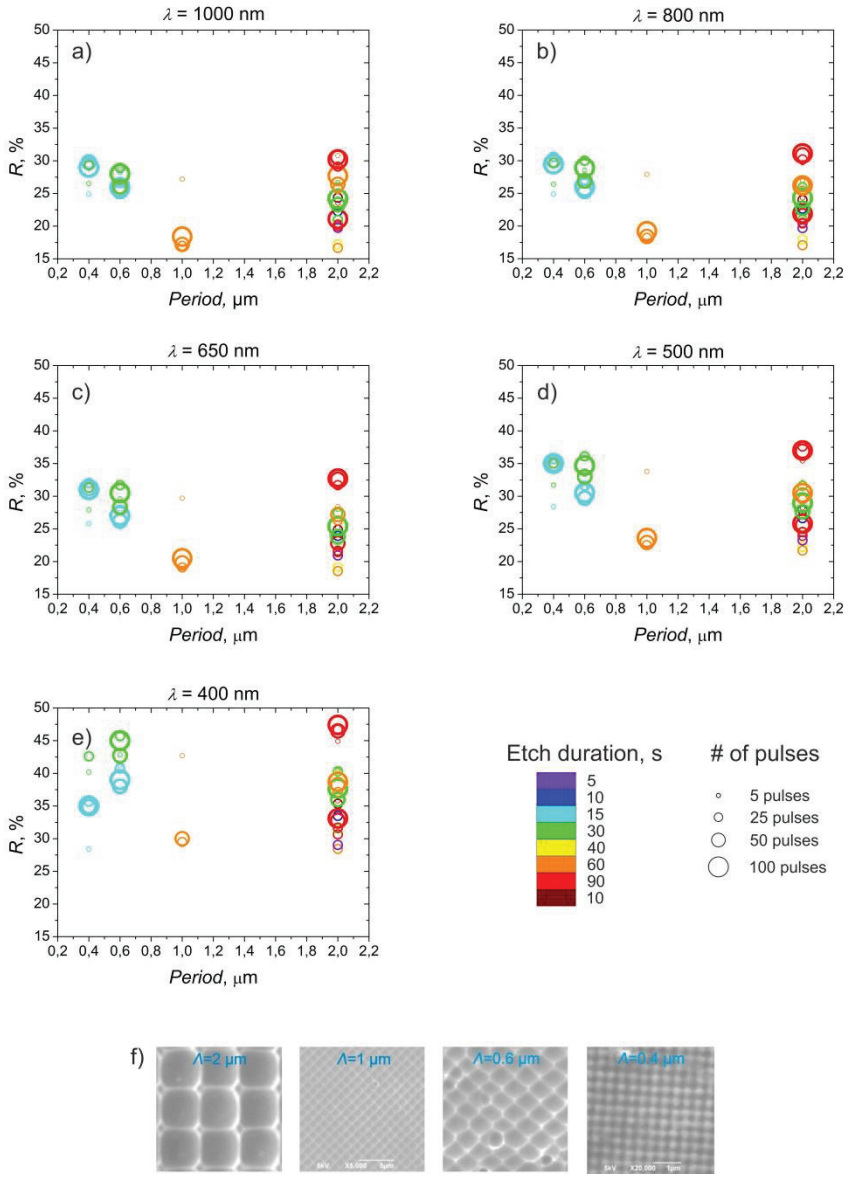

Fig. 44. Reflectance dependence on the structure period for 1000 nm (a), 800 nm (b), 650 nm (c), 500 nm(d), and 400 nm (e) wavelengths. f) SEM images of the structures with various periods.

From these results, it is evident, that the 2 µm and 1 µm period structures exhibit better antireflective properties than the 0.6 and 0.4 µm period structures in the entire spectrum up to 400 nm wavelength. This result is in contrast with the simulation. The poor performance of the small period structures could be caused by the thermal effects during the ablation. In Fig. 45, the reflectance spectra of the 2 µm period texture, obtained using the optimal irradiation and etching conditions is compared with the reflectance of various textures, reported in the literature. The performance of the DLIP -formed structure is similar to other laser fabrication methods.

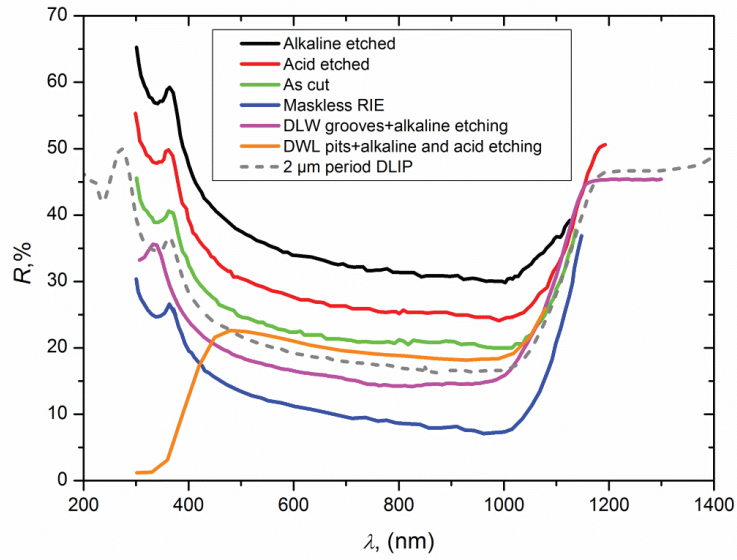

Fig. 45. Reflectance spectra of multicrystalline silicon textured using various methods. Green line – wafer with saw damage [52], black line – alkaline etched [52], red – acid etched [52], blue – mask-less RIE textured [52], magenta – grooves formed using direct laser writing and wet chemical etching [57], orange – pits formed by DLW and wet chemical etching [58]. Dashed grey line – result obtained using the 2 µm period DLIP and isotropic wet chemical etching.

6.3 Thermal Effects in Small-Period DLIP

When the period of the interference pattern is sufficiently small, the material between the intensity peaks may be heated to the temperatures exceeding the melting temperature. Fig. 46a shows SEM images of crystalline silicon irradiated using the 400 nm period 4-beam interference intensity distribution. Only narrow parameter set (top left corner in Fig. 46a) can be used to obtain a

regular texture. In other instances, melting of the silicon surface results in a disordered structure. Even when low fluence and a single laser pulse are used, the fabricated structure differs from the larger period structures. The structure depth and the period ratio were much smaller, for 400 nm period than for 2 μm period (0.5 and 0.08 respectively). Formation of the nanobumps was observed using various irradiation regimes. AFM profiles of the nanobump structures are provided in Fig. 46b-d. Formation of the bump structures may be caused by the surface tension forces in melted silicon layer [134].

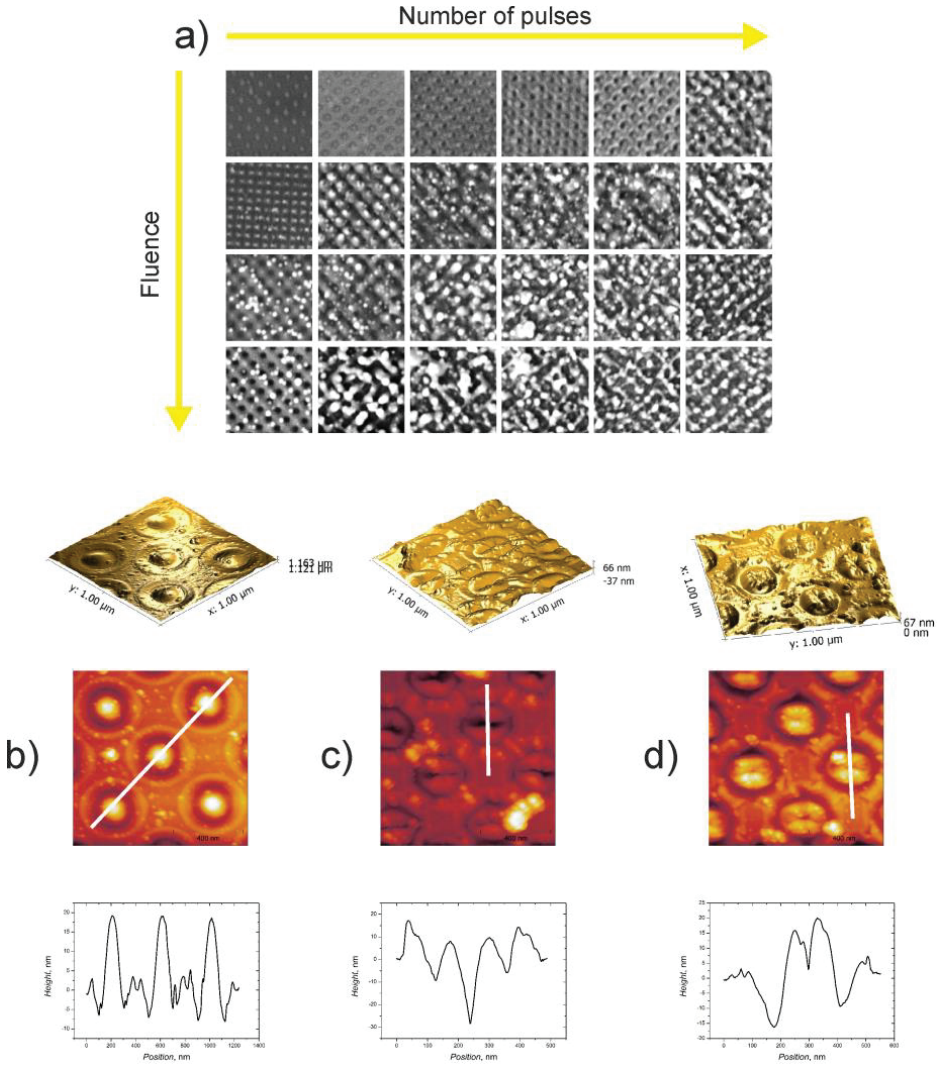

Fig. 46. SEM and AFM data of the 400 nm period structure on silicon obtained using the 4-beam DLIP with the 355 nm wavelength and 300 ps pulses. a) – SEM images of patterns obtained using various pulse number and fluence values; b) – AFM images and profile of the structure fabricated using 3 J/cm^2 and 1 pulse; c) AFM images and profile of the structure fabricated using 4.5 J/cm^2 and 1 pulse; d) AFM images and profile of the structure fabricated using 4.4 J/cm^2 and 1 pulse.

Such phenomena may be avoided using shorter laser pulses. Morphologies of the 600 nm period structures fabricated using the 4-beam DLIP, and 35 ns, 300 ps and 300 fs laser pulses were compared. Temperature distribution in the sample was simulated using COMSOL to numerically solve the heat transfer equation in a semi-infinite silicon slab. Simulation details are provided in the Appendix A. Fig. 47 shows SEM and AFM data obtained using different pulse durations and the corresponding simulated temperature distributions. In the experiment, various irradiation parameters were used, but for a final comparison, the regimes that provided equal dimple diameters for all pulse durations were selected. Ultrashort pulses provided not only smaller heat affected zone but also more efficient ablation. Femtosecond pulses ablated approximately 10 times deeper dimple than nanosecond pulses (Fig. 47d). The shallowness of the dimples fabricated using sub-nanosecond, and nanosecond pulses at least in part can be explained by refilling of the dimple with molten material. For such long pulses, a significant part of the material is in a liquid phase. Formation of nanobums in the dimples (Fig. 47b) suggests that liquid material flows back to the ablation zone (Marangoni effect).

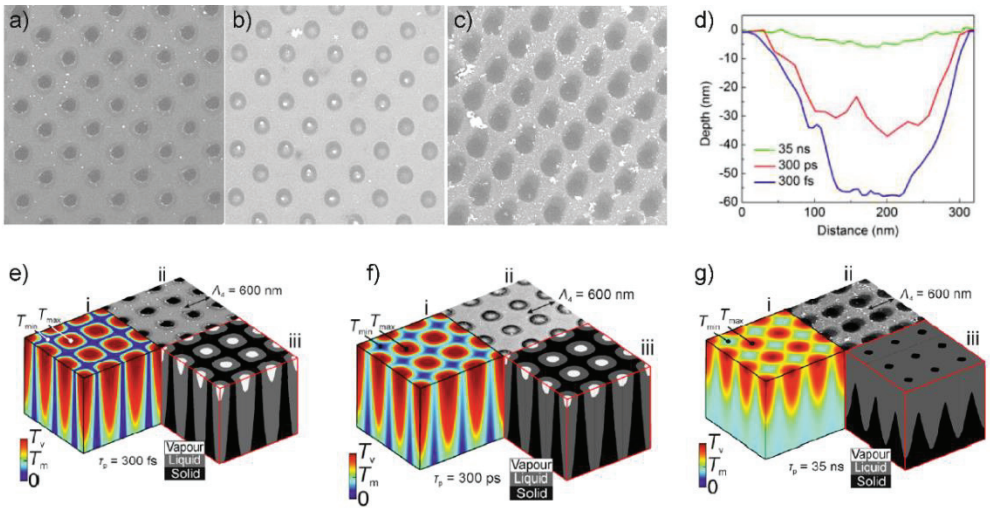

Fig. 47.Comparison of experiment and simulation of 600 nm period DLIP dimple ablation using 35 ns, 300 ps and 300 fs pulses. a) – SEM image of pattern ablated using 300 fs pulse duration; b) – 300 ps pulse duration; c) – 35 ns pulse duration; d) shows ablated dimples depth profiles for all three pulse durations; e) – g) shows simulated temperature distributions for 300 fs, 300 ps and 35 ns pulses respectively.

Therefore, the demonstrated silicon patterning method using the 300 ps pulse duration laser cannot be directly transferred to sub-micrometre periods due to different morphology of the ablated structure (nanobumps) and difficulties to obtain deep enough structures.

6.4 Conclusions

1. A dimple structure fabricated in the multicrystalline silicon using DLIP with 300 ps laser pulses and isotropic wet chemical etching allows obtaining as low as 17.5% reflectance in the 700 – 1000 nm spectral region.
2. Various period dimple structures were fabricated in the multicrystalline silicon using DLIP with 300 ps laser pulses. Sub-micrometre dimple structures provided higher reflectance than the 1 μm or 2 μm period structures. This result can be explained by the relatively small depth of the structure (when laser fabrication parameters still allow producing orderly periodic structure) caused by the formation of melt due to the relatively long duration (300 ps) of laser pulses.
3. Experiments and numerical simulations show that femtosecond or sub-picosecond pulses are required to increase the depth of the sub-micrometre periodic structure. The depth of the 600 nm period DLIP fabricated dimple structure (maintaining the same dimple diameter) can be increased 2 times if the pulse duration is reduced from 300 ps to 300 fs.

7 Adaptation of the DLIP Patterning Technique for the Fabrication of Uniform Periodic Structures in Thin Metal Films

The material, related to this chapter was published in [A4], [A6], [C7], [C9], [C11], [C13]

Plasmonic metamaterials – artificial materials consisting of subwavelength metallic elements – attract the attention of numerous researchers due to their unique abilities to manipulate light. Fabrication of even two-dimensional metasurfaces is challenging, since a high process throughput is needed, retaining low process cost and uncompromised pattern quality at the same time. Electron beam lithography (EBL) is commonly cited in the research papers considering metasurfaces [135]. EBL provides precise patterning. However, this technique is too slow for non-research purposes. High throughput techniques such as soft lithography techniques [136] or nanoimprint lithography [137] were also reported in the fabrication of metasurfaces. These methods allow large-scale fabrication. However, these techniques require a number of processing steps and masks or moulds prepared in advance. In some cases, the solution may be the laser interference patterning approach. The interference patterning allows distributing irradiation energy over large fabrication area and produces sub-wavelength features in this area with a single exposition.

7.1 DLIP Patterning Uniformity

One of the most difficult challenges in DLIP technology is ensuring pattern uniformity in areas larger than the quazi-uniform zone near the peak of the Gaussian laser beam. The problem of DLIP patterning uniformity can be divided into two aspects: uniformity across the single irradiation spot and uniformity in the overlapping of several irradiation spots. In this section,

results concerning the increase of patterning uniformity using beam shaping and beam scanning methods are described.

7.1.1 Beam shapers

Two beam shapers with different characteristics were tested.

GTH-5-250-4 (Topag Lasertechnik GmbH) beam shaper requires 5 mm diameter (at $1/e^2$ level) input beam and produces the 4x4 mm^2 square top-hat beam from the Gaussian beam at the 250 mm distance. Optical setup used for testing of this beam shaper is provided in Fig. 12a. The shaper was put 250 mm before the DOE. The 4x4 mm square top-hat beam was formed on the DOE and transferred to the interference plane by the 4f-lens system. Tests were performed using the 1.5x and 6.67x demagnification 4f systems with the second harmonics (532 nm) of Atlantic HE laser. Output in the interference plane was captured using a beam profiling camera and by modification of thin Cr film on a glass substrate. The result is shown in Fig. 48.

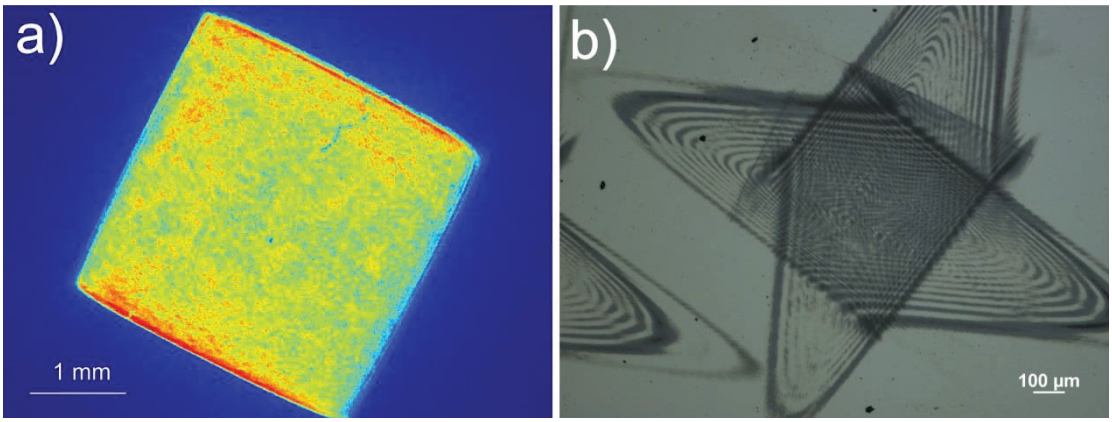

Fig. 48. Beam shaped using the Topag GTH-5-250-4 top-hat beam shaper and 1.5 (a) and 6.67 (b) demagnification interference systems. Picture a) was obtained using a beam profiling camera. Picture b) is an optical microscope image of the modification in thin Cr film induced using the shaped beam.

πShaper 6_6_532 (AdlOptica GmbH) beam shaper requires the 6.35 mm diameter (at $1/e^2$ level) input beam and produces the 5.8 mm diameter circular top-hat beam. Unlike the Gaussian beam, the propagating top-hat beam undergoes distortion of the intensity profile. The Topag GTH-5-250-4 shaper produces undistorted intensity profile only in the focal plane of the element.

Whereas, πShaper provides some distance in which the top-hat beam profile is preserved. That distance is directly proportional to the square of the beam diameter and inversely proportional to the wavelength. For the πShaper 6_6_532, the distance where distortions of the profile do not exceed 10 % is 200 – 300 mm [138]. Optical setup used for the test with πShaper 6_6_532 is provided in Fig. 12b. Tests were performed using the 4f system with 3x demagnification (L1=+150 mm, L2=+50 mm) with the second harmonics (532 nm) of the Atlantic HE laser. Intensity distributions at the output of πShaper and at the output of the interference system were captured using a beam profiling camera. Additionally, the performance of the shaped beam was compared to that of the Gaussian beam by ablating patterns in a thin Cr film on a glass substrate. Results are provided in Fig. 49. πShaper 6_6_532 provided uniform flat-top beam even with relatively high demagnification of the 4f system.

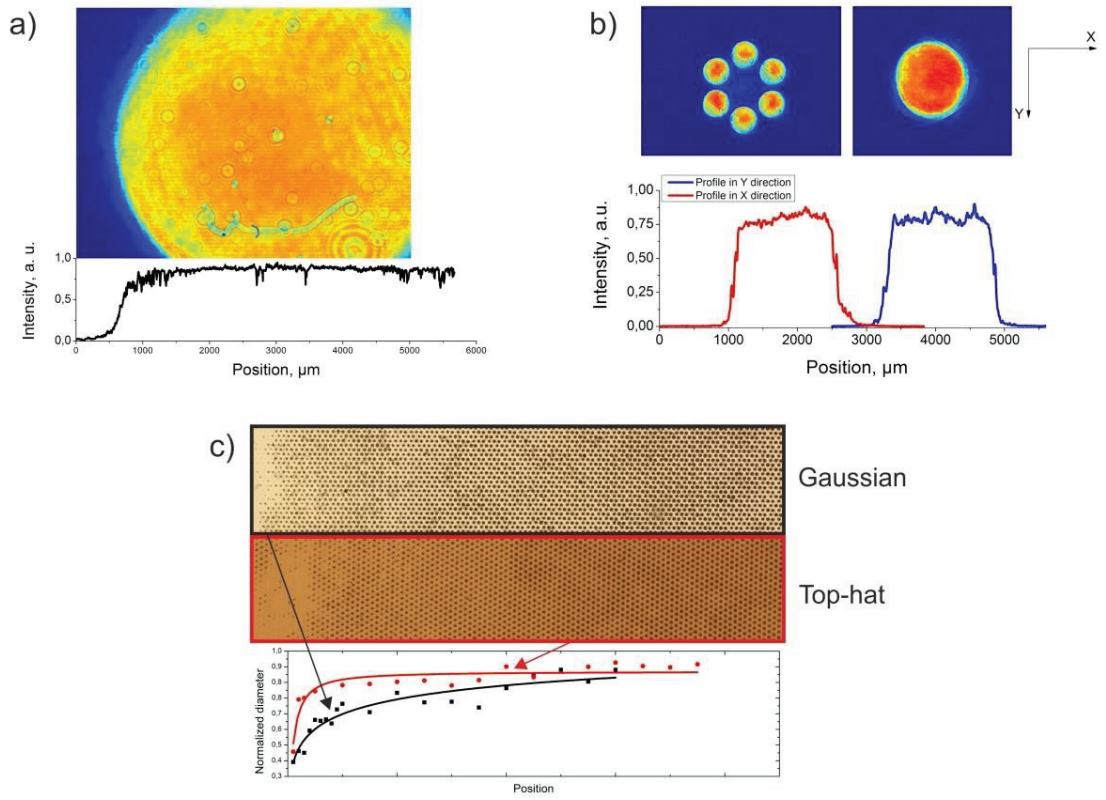

Fig. 49. The shaping of the interfering beams with πShaper 6_6_532 beam shaper. a) intensity distribution at the output of beam shaper; b) intensity distribution of 6 interfering beams; c) comparison of ablation of thin Cr film with Gaussian and top hat beams. The graph shows the

distribution of ablation crater diameters (normalised to unity) from the edge to the centre of the irradiated spot.

7.1.2 Beam scanning

Beam shaping using special optical elements provide increased pattern uniformity inside the interference spot. However, stitching of several interference spots is needed to increase the area of the uniform patterning further. Therefore, optical setup for beam scanning through the interference system was tested. The idea is visualised in Fig. 12d. Interfering beams are scanned by moving the optical setup with the sample with respect to the beam. By selecting appropriate overlap of the interference spots, the uniform texture is fabricated. This technique was tested with the 4-beam (3.4 μm period) and 6-beam (5.4 μm period) interference setups using the second harmonics (532 nm) of Atlantic HE and NL220 lasers. Size of the fabrication area is limited by the aperture of the optics and decreases with the structure period due to the demagnification of the 4f lens system. Also, the maximal size of pattern area using the beam scanning approach is limited by aberrations in the optical setup. With increasing pattern period (increasing ratio of lens focal lengths in the 4f system), aberration-free area decreases [104]. Using the 25.4 mm diameter lenses in the 4-beam interference setup to produce 3.4 μm pattern period, the patterning area was limited to 5x5 mm^2. Thin aluminium films (50 nm-thick) on silicon and sapphire substrates and Cr film on glass substrate were patterned. 86% interference spot overlap was found to be sufficient for the production of uniform pattern features in the entire pattern area. SEM and optical microscope images of the patterned regions are shown in Fig. 50.

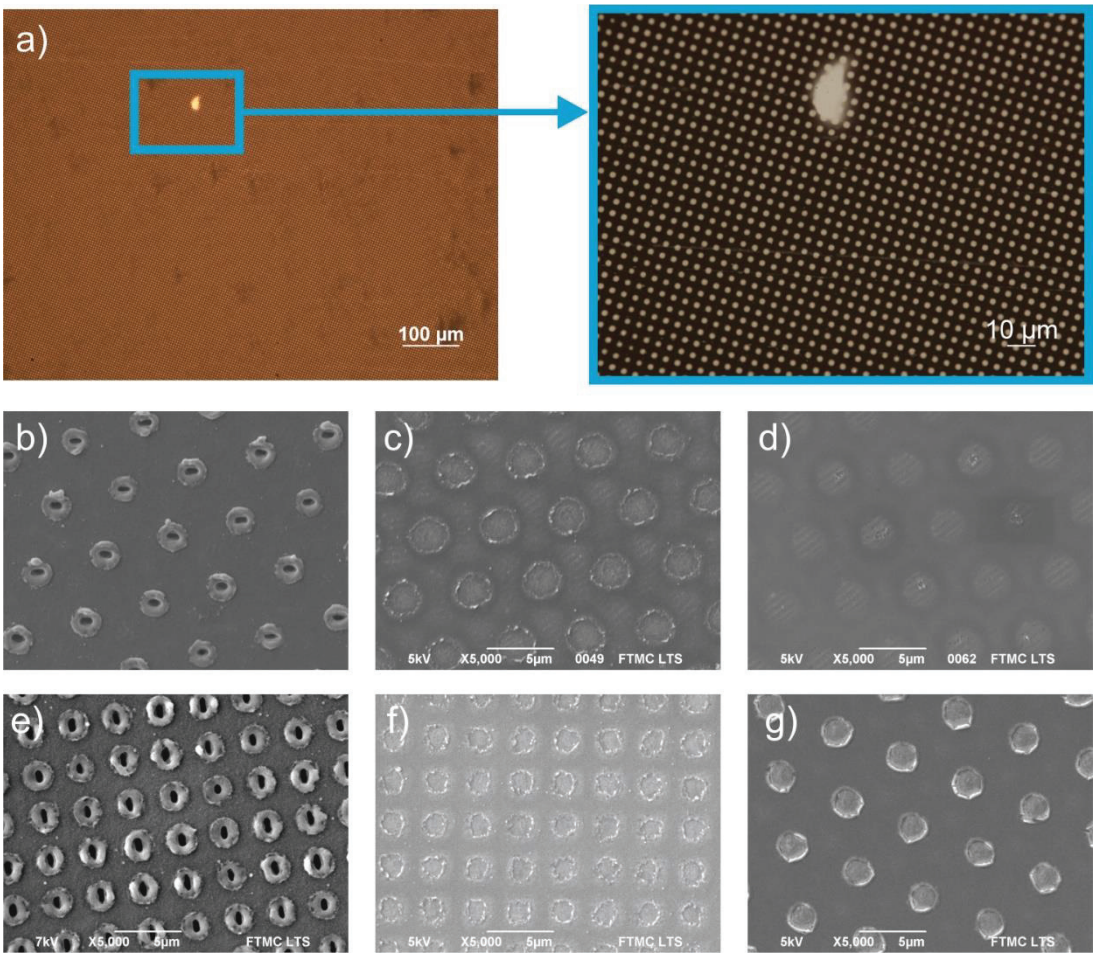

Fig. 50. Thin metal films patterned using interference spot scanning. a) – Cr film on glass substrate; b) Al film on silicon, 300 ps pulse duration; c) Al film on sapphire 300 ps pulse duration; d) Al film on sapphire 300 ps pulse duration; e) Al film on silicon 300 ps pulse duration; f) Al film on sapphire 300 ps pulse duration; g) Al film on sapphire 35 ns pulse duration;

Reflectance spectra of the 0^{th} diffraction order were measured (Fig. 51). Reflectance dips in the spectrum measured from the hole's array fabricated using the low pulse numbers per spot coincides with the theoretically calculated resonance peak wavelengths. These wavelengths were evaluated using expression [139]:

$$\lambda_{\max} = \frac{\Lambda \sqrt{\frac{\varepsilon_d + \varepsilon_m}{\varepsilon_d \varepsilon_m}}}{\sqrt{i^2 + j^2}} \qquad (10)$$

where Λ is the structure period, i and j are integers denoting SPP (Surface Plasmon Polariton) resonance mode. ε_m and ε_d are metal and dielectric permittivities, respectively.

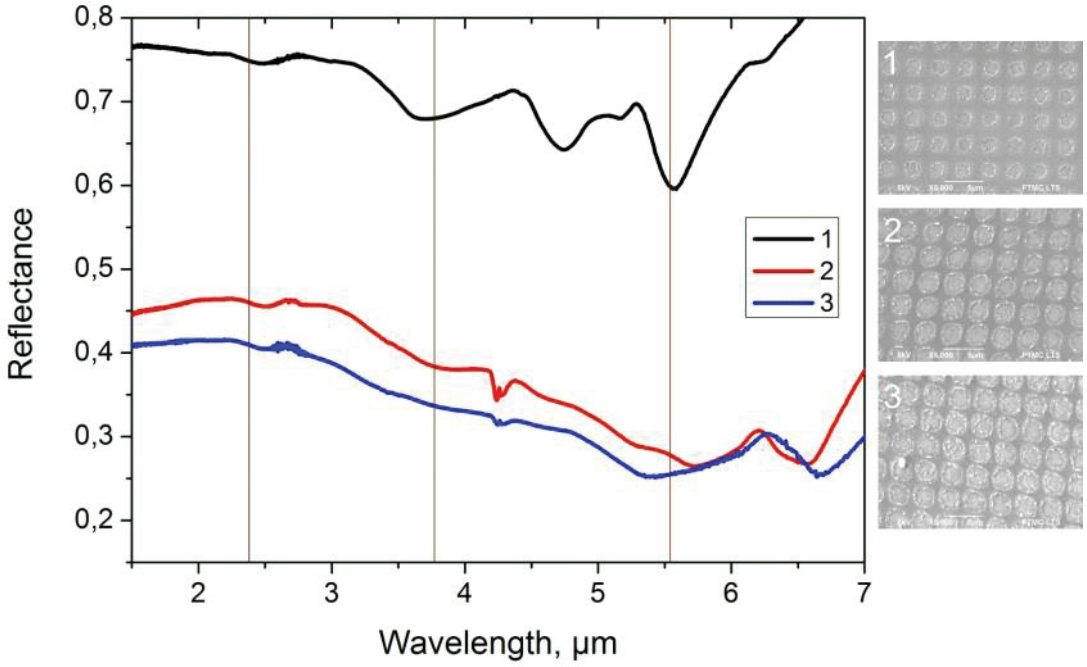

Fig. 51. Reflectance spectra of 3.4 μm period hole arrays in 50 nm Al film on the sapphire substrate. Vertical lines indicate theoretically evaluated resonance peak wavelengths. Curve 1 – 1 J/cm^2, 86% spot overlap, 1 pulse per spot; curve 2 – 1 J/cm^2, 86% spot overlap, 10 pulse per spot; curve 3 – 1 J/cm^2, 86% spot overlap, 25 pulse per spot. On the right, SEM images of corresponding hole arrays are shown.

Fabrication of large diameter hole arrays using 10 to 25 pulse numbers per spot resulted in the disappearance of the reflectance dips. This may be the result of the formation of disordered metal particles and corrugations in the ablation zone.

7.2 Polarization Control

In this chapter, experimental implementation of the confocal 6-beam interference setup with the polarisation control of each separate beam is discussed. Using this approach, a number of patterns that were obtained experimentally for the first time using the interference patterning technique are provided.

Experiments were conducted using the 6-beam interference setup and the second harmonics (532 nm) of sub-nanosecond laser Atlantic HE. The optical setup is shown in Fig. 12c. 6 laser beams were combined on the sample using a confocal imaging system, consisting of two 50.8 mm diameter lenses L1 and L2 with focal lengths 150 and 100 mm respectively. Control of the polarisation was accomplished by six half-wave plates (WP), (Eksma Optics) placed in the path of each of the 6 beams. The special 3D printed holder was produced to fix the plates with the possibility to rotate them by 360°. The polarization direction of each beam was adjustable by rotating the half-wave plate (initial laser beam was linearly polarized). The resulting intensity distributions were observed using beam profiler camera and compared to the computer simulated model created using Eq. (5).

Intensity patterns, generated in that way, were used to ablate periodic structures in the 20 nm-thick chromium film deposited on a glass substrate. SEM images of the fabricated structures were compared with the calculated patterns at a particular laser intensity level, taking into account the threshold nature of thin-film ablation.

Fig. 52 compares intensity distributions of various 6-beam polarisation configurations calculated and captured with the beam profiler camera, as well as corresponding patterns ablated in the chromium film. In the first column, the top view of the beam arrangement is shown as the bold red arrows. Thin blue arrows indicate the polarisation direction of a corresponding beam.

Second and third columns contain calculated intensity distributions and intensity distributions at specific threshold values (the black colour marks non-ablated material, white - ablated material), to make a comparison with ablated structures more convenient. The fourth column contains SEM images of patterns ablated in a chromium film using the provided intensity distributions. In the fifth column, the intensity distributions captured with the beam profiler camera are provided.

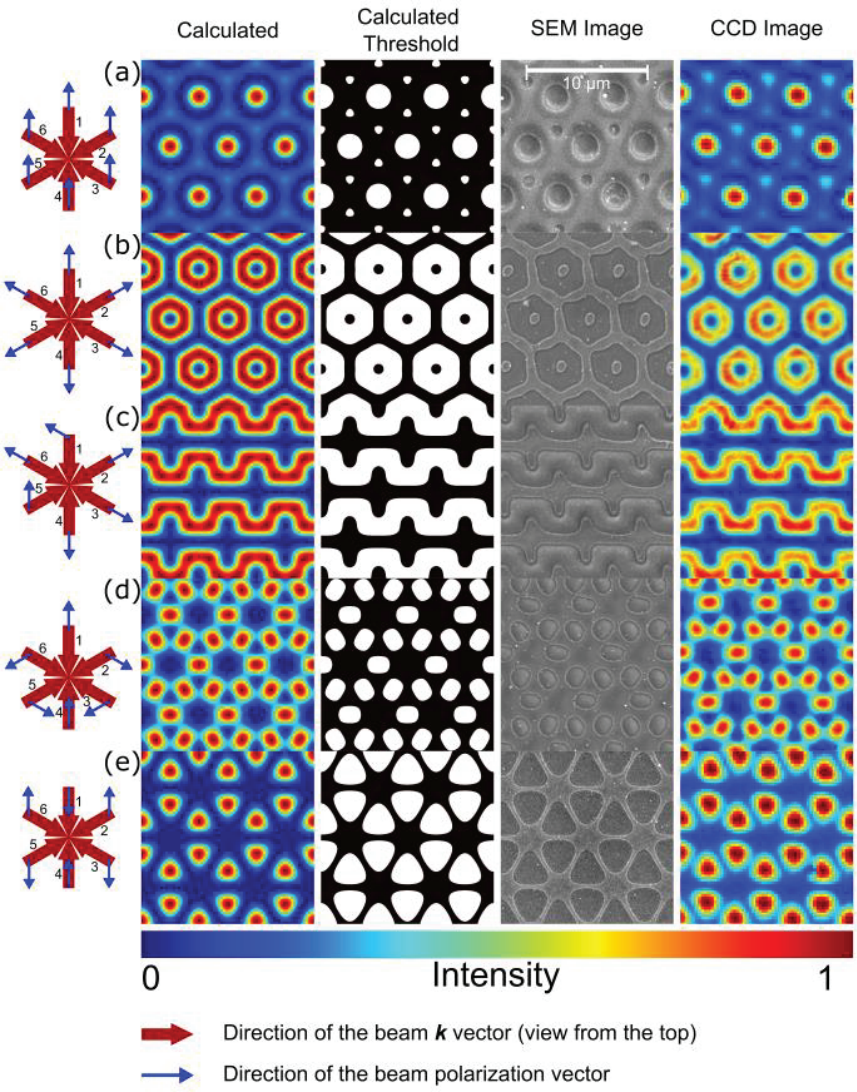

Fig. 52. Comparison of calculated interference intensity distributions with the images obtained with the beam profiler camera and SEM images of the structures ablated in the thin Cr film. Fabrication parameters: (a) – 0.4 J/cm^2, 1 pulse per exposition; (b) – 0.6 J/cm^2, 1 pulse; (c) – 0.6 J/cm^2, 3 pulses; (d) – 0.2 J/cm^2, 1 pulse; (e) – 1.8 J/cm^2, 1 pulse. In all cases, fluence corresponds to the fluence on the sample surface in the peaks of interference intensity distribution.

Excellent match between calculated and experimentally obtained images is apparent. Pattern uniformity was retained in the entire structured areas (aside from the effect of the Gaussian beam shape (Fig. 53).

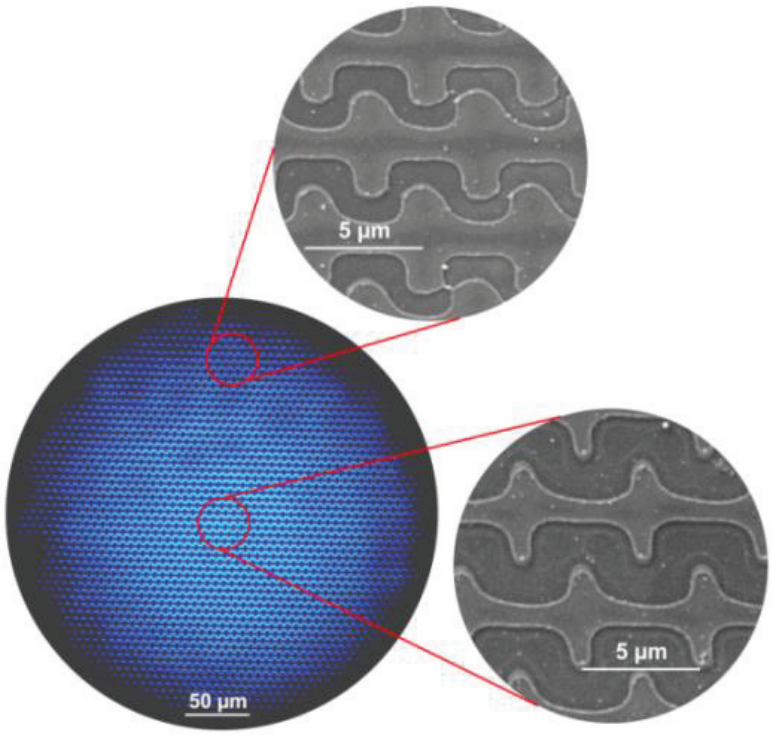

Fig. 53. Full-size interference irradiation spot, corresponding to the Fig. 52c.

Fig. 52a shows the "conventional" 6-beam interference pattern. Here all beams have the same polarisation direction. To demonstrate the flexibility of the approach, the doughnut-shaped apertures (Fig. 52b), zigzag apertures (Fig. 52c), overlapping rings of apertures (Fig. 52d) and "star" shape (Fig. 52e) were fabricated by selecting the appropriate direction of the polarisation vector for each beam.

The variety of pattern shapes can be further increased by blocking some of the beams. By blocking two beams and choosing certain directions of polarisation vectors for the remaining beams, the dot and rod structure (Fig. 54a), paired hole structure (Fig. 54b) and "Millipede" structure (Fig. 54c) were obtained.

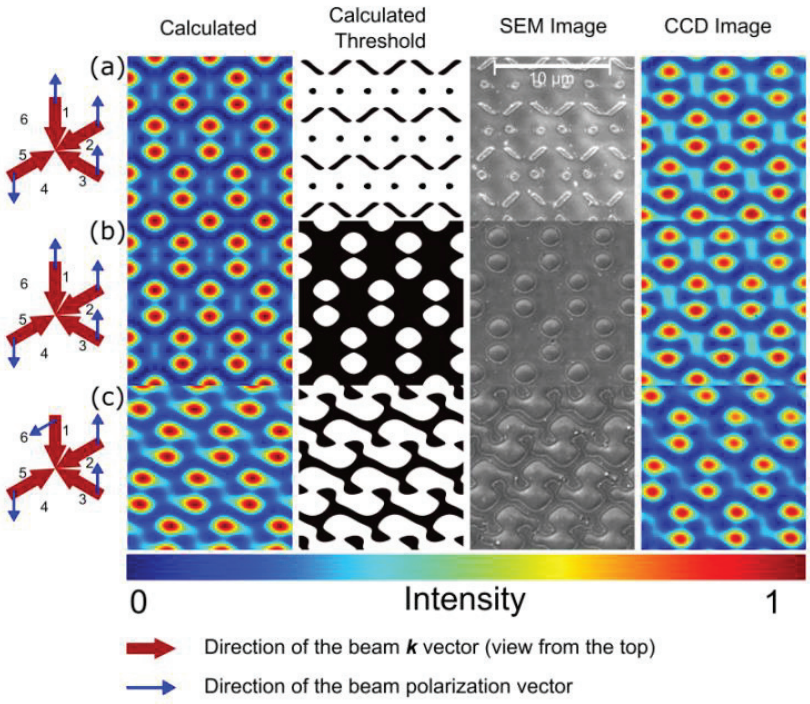

Fig. 54. Comparison of calculated interference intensity distributions with the images obtained with the beam profiler camera and SEM images of the structures ablated in Cr thin film. Fabrication parameters: (a) – 1.9 J/cm^2, 4 pulses per exposition; (b) – 0.6 J/cm^2, 5 pulses; (c) – 1.3 J/cm^2, 4 pulses. In all cases, fluence corresponds to the fluence on the sample surface at the peaks of interference intensity distribution.

To ensure easier and repeatable fabrication, motorised 6-beam polarisation control unit was designed. The sketch of the unit is provided in Fig. 55.

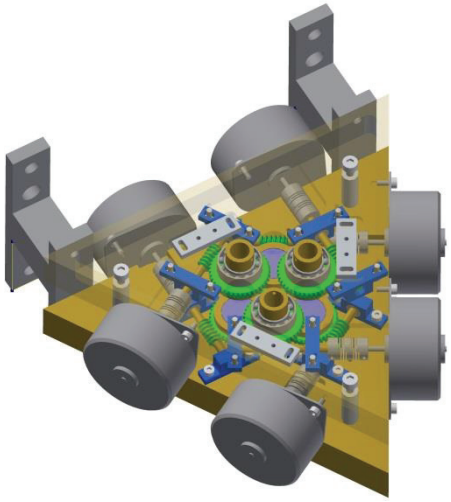

Fig. 55. Sketch of the motorised 6-beam polarisation control unit.

7.3 Influence of Angle between the Interfering beams on Intensity Pattern Modulation Depth and Shape in Polarization Control Setup

When the angle between the interfering beams becomes large, vertical components of polarisation vectors become significant. Then the resulting pattern depends on the angle between the interfering beams, even when all other parameters are kept constant. When the angle between the interfering beams is large, not only the modulation depth but also the shape of the intensity pattern depends on the polarisation arrangement. Influence of the angle between the interfering beams on the intensity distribution modulation depth and pattern shape was examined. Specific beam polarisation configurations were investigated numerically and by capturing the interference distributions experimentally using the beam profiler camera.

Interference intensity distributions were calculated using Eq. (5). In the simulations, all beams were symmetrically arranged (elevation angles were equal for all beams). The 532 nm wavelength was used in all simulations. Electric field amplitudes and phases were set as equal for all beams in all simulations. If the modulus of the electric field for a certain beam is *E,* then electric field components for this beam are:

$$\begin{aligned} E_x &= E\cos\Theta_2\cos\gamma \\ E_y &= E\cos\Theta_2\sin\gamma \\ E_z &= E\sin\Theta_2\cos\xi, \end{aligned} \tag{11}$$

where γ is an angle between the projection of the electric field vector **E** to the XY-plane and the x-direction of the coordinate system, Θ_2 is the half angle between the beams, ξ is the angle between the projections of the **k** and **E** vectors in the XY-plane (Fig. 56).

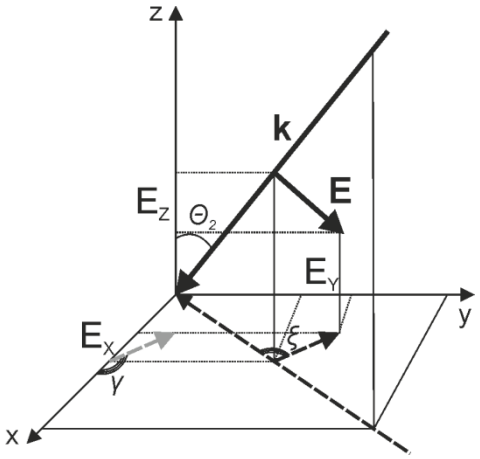

Fig. 56. Components and projection to the XY-plane of the electric field vector E.

Changes in the intensity patterns using different angles between the interfering beams may be attributed to the increasing impact of the vertical (z) component of the polarisation vector. When beams are converging at a small angle, the vertical component is negligible, and Eq. (5) for the two beams, both polarised in the x-direction ($E_x=E$; $E_y=0$; $E_z\equiv 0$) can be reduced to:

$$I(x,y,z) \cong E^2 + E^2 \cdot \cos\left((\mathbf{k}_1 - \mathbf{k}_2)\mathbf{r}\right) \tag{12}$$

When the vertical component cannot be ignored ($E_x=E\cos\Theta_2$; $E_y=0$, $E_z=E\sin\Theta_2$), Eq. (5) for the two identically polarised beams becomes:

$$\begin{aligned} &I(x,y,z) \cong E_x^2 + E_z^2 + \left(E_x^2 - E_z^2\right) \cdot \cos\left((\mathbf{k}_1 - \mathbf{k}_2)\mathbf{r}\right); \\ &E_x = E\cos\Theta_2; \\ &E_z = E\sin\Theta_2; \end{aligned} \tag{13}$$

where E is an absolute value of the electric field vector **E**. So, in the case of interference of two p-polarized identical beams, an increase of the angle Θ_2 reduces the modulation depth of the intensity pattern. The angle Θ_2, at which E_z component becomes relevant, can be defined as 13°. At this angle, the modulation depth of the 2-beam (p-polarized) intensity pattern decreases by 10%.

For s-polarized beams, Eq. (5) is:

$$\begin{aligned} &I(x,y,z) \cong E_y^2 + E_y^2 \cdot \cos\left((\mathbf{k}_1 - \mathbf{k}_2)\mathbf{r}\right); \\ &E_y = E\cos\Theta_2; \end{aligned} \tag{14}$$

and there is no influence of the angle Θ_2 on the modulation depth since there are no E_z components.

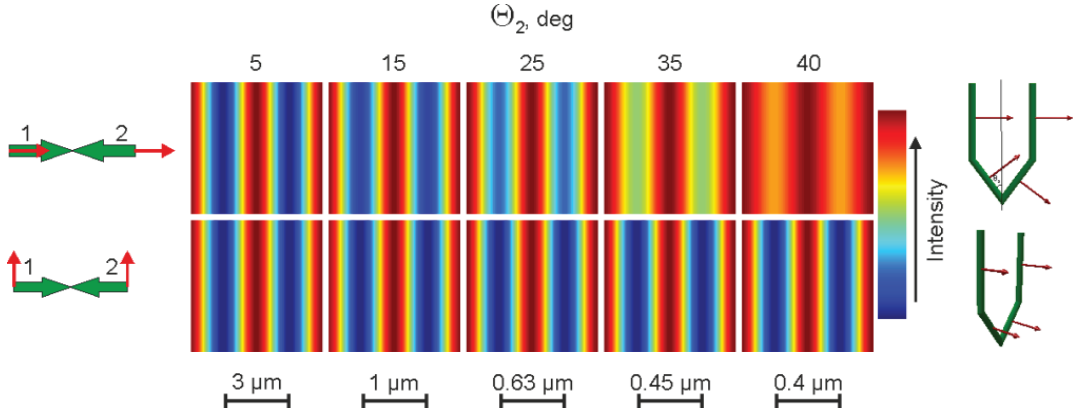

Fig. 57. Simulated 2-beam interference intensity distributions for different half angles between the beams Θ_2 and different polarisation arrangements. Scheme on the left shows the layout of the laser beams from the top (thick arrows) and directions of polarisation vectors (thin arrows). Scheme on the right shows the 3D layout of the laser beams (green) and polarisation vectors (red).

Fig. 57 shows a simulation of two-beam interference using various half-angles between the beams and two different polarisation arrangements. It is evident that for the p-polarization a modulation depth of the intensity pattern decreases with the growing angle Θ_2. However, for the s-polarization, there is no influence of the angle Θ_2 on the intensity pattern.

Fig. 58 shows profiles of the intensity distributions obtained using beam profiler camera for two s- and p- polarised interfering beams.

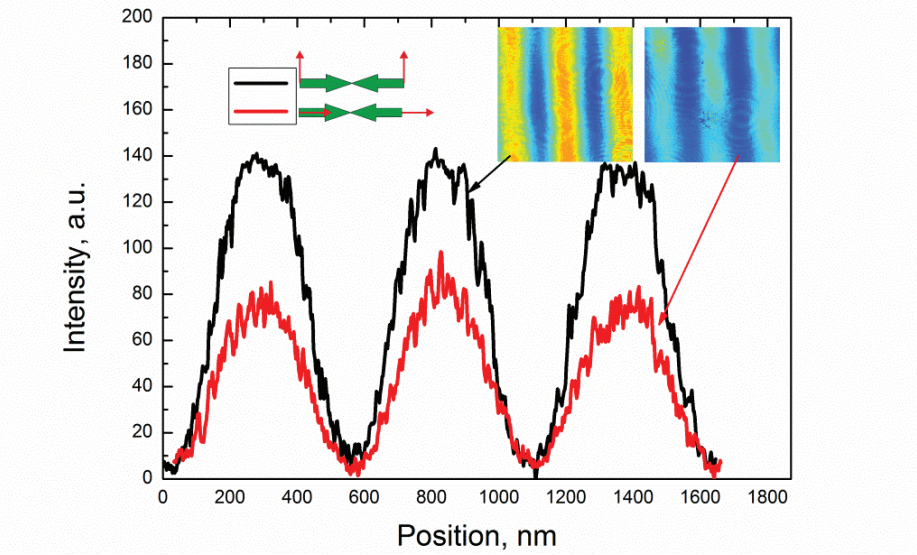

Fig. 58. 2-beam interference intensity profiles for two polarisation states. Line pattern period is 660 nm; the half angle between the beams is 20.7 °.

The same approach can be used to investigate the influence of the angle Θ_2 on the modulation depth on the pattern of three interfering beams. In the case of 3 identical interfering beams, polarised in the x-direction, the modulation depth also decreases with the increasing angle, only slower than in the case of 2 beams:

$$I(x,y,z) \cong 1\frac{1}{2}E_x^{\,2} + \frac{3}{4}E_z^{\,2} + \left(E_x^{\,2} - \frac{1}{2}E_z^{\,2}\right)\cdot\cos\left((\mathbf{k}_1 - \mathbf{k}_2)\mathbf{r}\right) + \\ + \left(E_x^{\,2} - \frac{1}{2}E_z^{\,2}\right)\cdot\cos\left((\mathbf{k}_1 - \mathbf{k}_3)\mathbf{r}\right) + \left(E_x^{\,2} + \frac{1}{4}E_z^{\,2}\right)\cdot\cos\left((\mathbf{k}_2 - \mathbf{k}_3)\mathbf{r}\right); \qquad (15)$$
$$E_x = E\cos\Theta_2;$$
$$E_z = E\sin\Theta_2;$$

In this case, terms for the beam pairs 1,2 and 1,3 (Fig. 59) differ from the term for beam pair 2,3. This difference grows with increasing E_z component (increasing angle Θ_2). Therefore, asymmetry is induced in the pattern at the large angles (Fig. 59a).

However, when the beam polarisations directions are diverse, more drastic changes in the intensity distribution arise. Polarization vectors of three interfering beams can be arranged at 120° angles to provide inverted intensity pattern (Fig. 59b). In this case, the influence of the E_z components is more significant:

$$I(x,y,z) \cong \frac{3}{4}E_x^{\,2} + E_y^{\,2} + \frac{3}{2}E_z^{\,2} + \left(E_z^{\,2} - \frac{1}{2}E_x^{\,2}\right)\cdot\cos\left((\mathbf{k}_1 - \mathbf{k}_2)\mathbf{r}\right) +$$
$$+\left(E_z^{\,2} - \frac{1}{2}E_x^{\,2}\right)\cdot\cos\left((\mathbf{k}_1 - \mathbf{k}_3)\mathbf{r}\right) + \left(E_z^{\,2} - \frac{1}{2}E_x^{\,2}\right)\cdot\cos\left((\mathbf{k}_2 - \mathbf{k}_3)\mathbf{r}\right); \qquad (16)$$
$$E_x = E\cos\Theta_2;$$
$$E_y = \tfrac{\sqrt{3}}{2}E\cos\Theta_2;$$
$$E_z = E\sin\Theta_2;$$

Coefficients at the cosine terms are equal; therefore, in this case, there is no asymmetry when the angle between the interfering beams is large. However, an increase of Θ_2 significantly reduces the modulation depth.

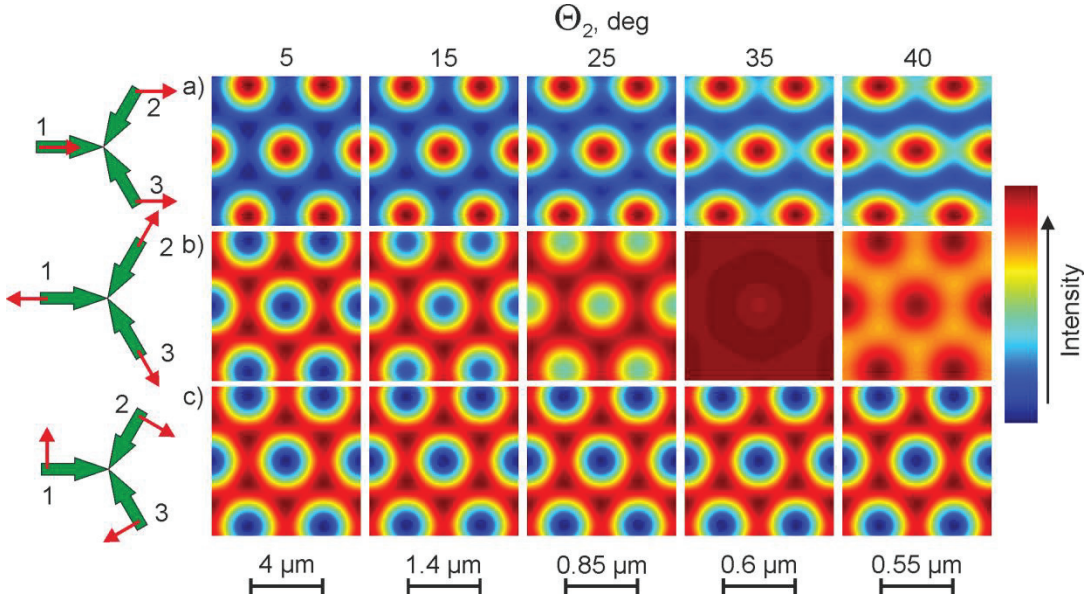

Fig. 59. Simulated 3-beam interference intensity distributions for different polarisation arrangements.

However, if the polarisation vectors are oriented as shown in Fig. 59c, identical patterns for all angles Θ_2 can be obtained. In such arrangement electric field components E_z equals to zero for all beams:

$$I(x,y,z) \cong E_x^{\,2} + \frac{3}{4}E_y^{\,2} - \frac{1}{2}E_y^{\,2}\cdot\cos\left((\mathbf{k}_1 - \mathbf{k}_2)\mathbf{r}\right) - \frac{1}{2}E_y^{\,2}\cdot\cos\left((\mathbf{k}_1 - \mathbf{k}_3)\mathbf{r}\right) -$$
$$-\frac{1}{2}E_y^{\,2}\cdot\cos\left((\mathbf{k}_2 - \mathbf{k}_3)\mathbf{r}\right); \qquad (17)$$
$$E_x = \tfrac{\sqrt{3}}{2}E\cos\Theta_2;$$
$$E_y = E\cos\Theta_2.$$

Fig. 60 shows an experimental illustration of the influence of the angle between the interfering beams on the modulation depth in the case of three

interfering beams. There is no difference between modulation depths of regular and inverted 3-beam intensity pattern when $\Theta_2 = 7.5$ (Fig. 60a). However, when Θ_2 is increased to 20.7 °, the modulation depth of the inverted pattern decreases compared to the regular pattern (Fig. 60b). Modulation depth difference between the regular patterns at different angles Θ_2 is about 17 %. These results are in good agreement with the simulation.

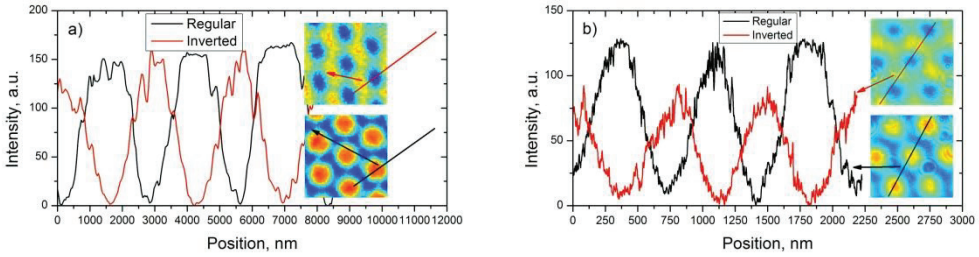

Fig. 60. 3-beam interference intensity profiles, measured using beam profiler camera. a) pattern period 2.7 µm (half angle between the beams 7.5), b) – 0.88 µm (half angle between the beams 20.7 °).

In the case of 4-beam interference, Eq. (5) becomes:

$$\begin{aligned} &I(x,y,z) \cong 2E_y^{\,2} + E_z^{\,2} + E_y^{\,2} \cdot \cos\left((\mathbf{k}_1 - \mathbf{k}_2)\mathbf{r}\right) + E_y^{\,2} \cdot \cos\left((\mathbf{k}_1 - \mathbf{k}_3)\mathbf{r}\right) + \\ &+ E_y^{\,2} \cos\left((\mathbf{k}_1 - \mathbf{k}_4)\mathbf{r}\right) + E_y^{\,2} \cos\left((\mathbf{k}_2 - \mathbf{k}_3)\mathbf{r}\right) + \left(E_y^{\,2} - E_z^{\,2}\right)\cos\left((\mathbf{k}_2 - \mathbf{k}_4)\mathbf{r}\right) + \\ &+ E_y^{\,2} \cos\left((\mathbf{k}_3 - \mathbf{k}_4)\mathbf{r}\right); \\ &E_y = E\cos\Theta_2; \\ &E_z = E\sin\Theta_2; \end{aligned} \tag{18}$$

Therefore, if z components are non-negligible, asymmetry arises in the direction of polarisation vectors (Fig. 61a). However, in such case, asymmetry is small and virtually does not exist up to Θ_2=25°.

If beam pairs have orthogonal polarisations, the well-known check-board pattern can be formed. This pattern is much more susceptible to the influence of E_z components. In this case, Θ_2=15° is enough to observe the change in the pattern (Fig. 61b). For this configuration, Eq. (5) becomes:

$$\begin{aligned} &I(x,y,z) \cong E_x^{\,2} + E_y^{\,2} + 2E_z^{\,2} - E_z^{\,2}\cos\left((\mathbf{k}_1 - \mathbf{k}_2)\mathbf{r}\right) + \left(E_x^{\,2} - E_z^{\,2}\right)\cos\left((\mathbf{k}_1 - \mathbf{k}_3)\mathbf{r}\right) + \\ &+ E_z^{\,2} \cos\left((\mathbf{k}_1 - \mathbf{k}_4)\mathbf{r}\right) + E_z^{\,2} \cos\left((\mathbf{k}_2 - \mathbf{k}_3)\mathbf{r}\right) + \left(E_y^{\,2} - E_z^{\,2}\right)\cos\left((\mathbf{k}_2 - \mathbf{k}_4)\mathbf{r}\right) - \\ &- E_z^{\,2} \cos\left((\mathbf{k}_3 - \mathbf{k}_4)\mathbf{r}\right); \\ &E_x = E\cos\Theta_2; \\ &E_y = E\cos\Theta_2; \\ &E_z = E\sin\Theta_2; \end{aligned} \tag{19}$$

In this case, the influence of the E_z component at large angle Θ_2 is significant. The 4-beam interference configuration also provides an opportunity to avoid pattern distortion when the angle between the interfering beams is large. The 4-beam pattern is a combination of two pairs of interfering beams. Therefore, if polarisation vectors are orthogonal to the plane containing a beam pair, vertical (z) component of the electric field vector is equal to zero. If polarisation vectors in both beam pairs are arranged in such a way (Fig. 61c), a pattern does not change with increasing angle between the beams. For such arrangement, Eq. (5) is:

$$\begin{aligned} &I(x,y,z) \cong E_x^{\,2} + E_y^{\,2} + E_y^{\,2}\cos((\mathbf{k}_1 - \mathbf{k}_3)\mathbf{r}) + E_x^{\,2}\cos((\mathbf{k}_2 - \mathbf{k}_4)\mathbf{r}); \\ &E_x = E\cos\Theta_2; \\ &E_y = E\cos\Theta_2; \end{aligned} \qquad (20)$$

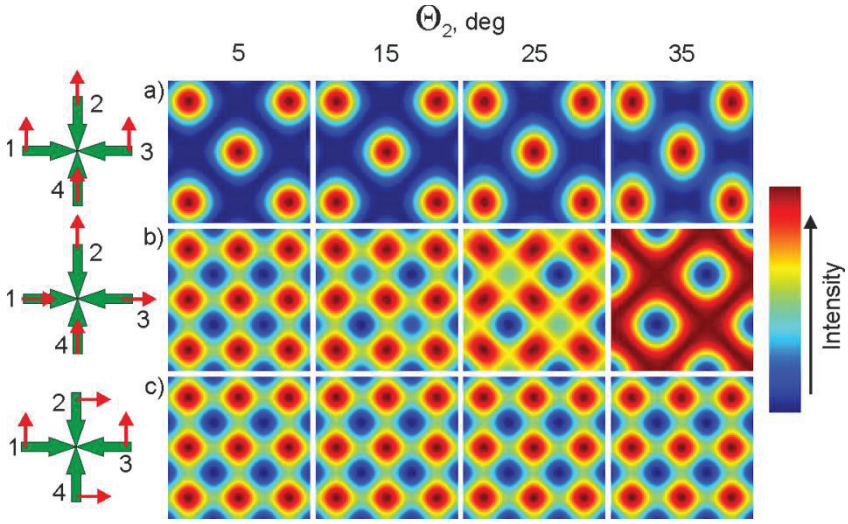

Fig. 61. Simulated 4-beam interference intensity distributions for different polarisation states.

Similarly, in the 6-beam setup, the significance of pattern distortions depends on the directions of each polarisation vector. Patterns obtained using the same polarisation angle or when angles between polarisation vectors are 0 or 180 degrees are susceptible to only small distortions (Fig. 62a; Fig. 62b). With increasing polarisation vector orientation diversity, distortion of the patterns become more expressed (Fig. 62c,d). In some cases, pattern distortions can be avoided by selecting appropriate polarisation directions. For example,

hexagonal ring structure can be highly distorted (Fig. 62d) or not distorted at all (Fig. 62e) depending on the arrangement of polarisation vectors.

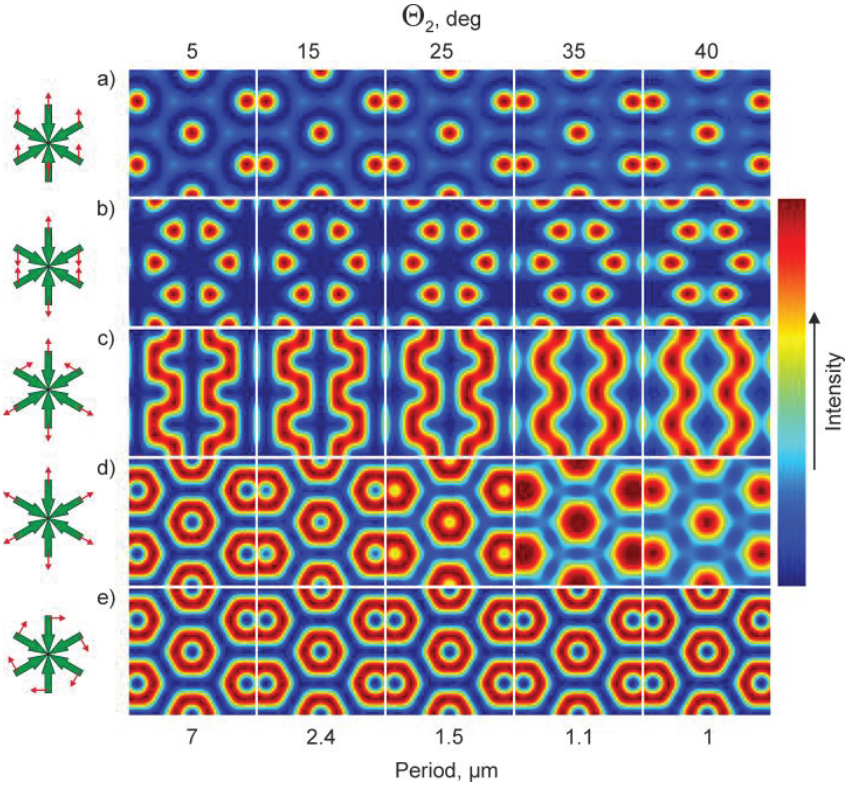

Fig. 62. Simulated 6-beam interference intensity distributions for different polarization states.

7.4 Adaptation of the Interference Setup for a High-Pulse-Energy Ultrashort Pulse Laser

To better exploit the capability of the interference patterning technique, high pulse energy laser sources are needed. At the same time, if the goal is a fabrication of sub-micrometre periodic patterns, femtosecond laser pulses are necessary for a good quality texturing. Therefore, modification of the interference patterning setup was tested with the high-pulse-energy (15 mJ@1030 nm) 200 fs pulse duration laser source provided by AmpLight KG. Characteristics of the laser pulse at the input and output of the interference system were investigated using Frequency-Resolved Optical Gating (FROG), spectrometer, beam profiler camera and ablation of silicon

and thin Cr film on glass substrate. The experimental setup is displayed in Fig. 13.

Input laser beam diameter was over 4 mm. However, beam diameter on the front surface of the second objective was smaller. This resulted in the manifestation of the non-linear optical effects. The effect was strong enough to see it with the eye as the generation of broad spectrum (including visible) radiation in the fused silica objective L2 (Fig. 13).

However, the spectrum of the irradiation reaching the interference plane did not shown significant alteration (Fig. 63).

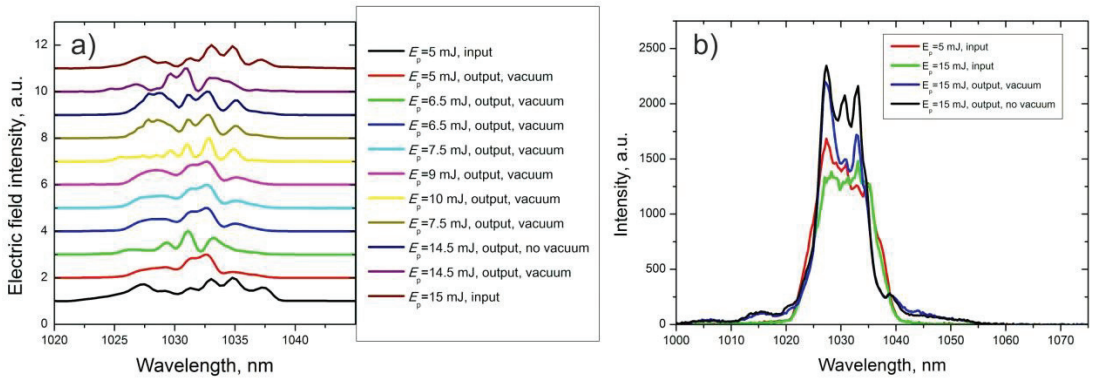

Fig. 63. a) – Electric field intensity spectra for different pulse energies E_p and vacuum conditions at the input and output of the optical setup, measured using FROG; b) electric field intensity spectra at the input and output of the optical setup, measured using the spectrometer.

Whereas, the impact of the optical system to the pulse duration is indisputable. Fig. 64a shows temporal pulse spectra obtained using FROG. Fig. 64b provides dependence of the pulse duration τ_p (calculated from the FROG spectra) on the pulse energy E_p. At the input of the optical setup, pulse duration remains constant for all pulse energies. At the output of the setup, the pulse duration shortens about 20 % if the pulse energy increases from 5 mJ to 12.5 mJ.

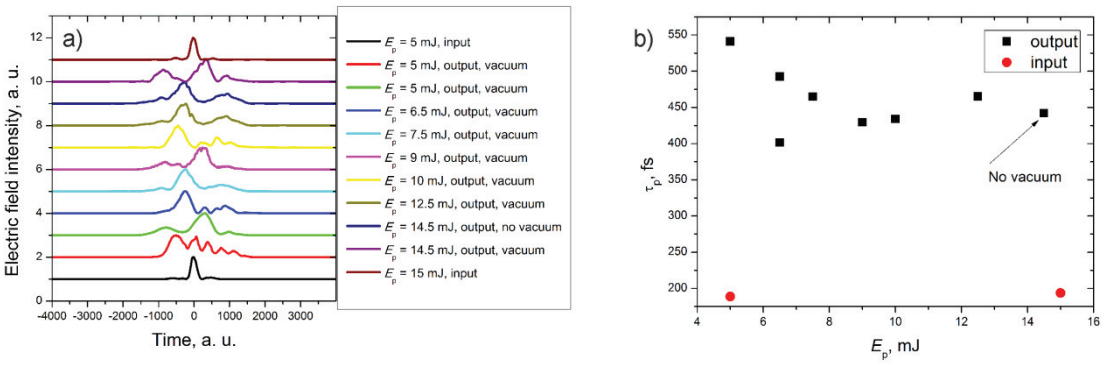

Fig. 64. a) – Electric field intensity temporal spectra, obtained by FROG; b) dependence of pulse duration τ_p on the pulse energy E_p at the optical setup input (red dots) and output (black squares).

Most importantly, pulse duration at the output doubles compared to the input. There was no significant impact on the pulse duration when there was no vacuum in the setup (Fig. 64b). However, a vacuum can help to avoid pulse energy fluctuations that may arise due to plasma generation in the air at the focal plane of the first objective.

The pulse duration of the laser source could be changed by tuning the pulse compressor. Influence of the pulse duration on the nonlinear effects and on the quality of the DLIP ablation was investigated. Strong nonlinear effects in the second objective were not observed anymore when input pulse duration was increased to 400 fs.

SEM images of periodic structures produced on the crystalline silicon samples using various pulse durations are shown in Fig. 65.

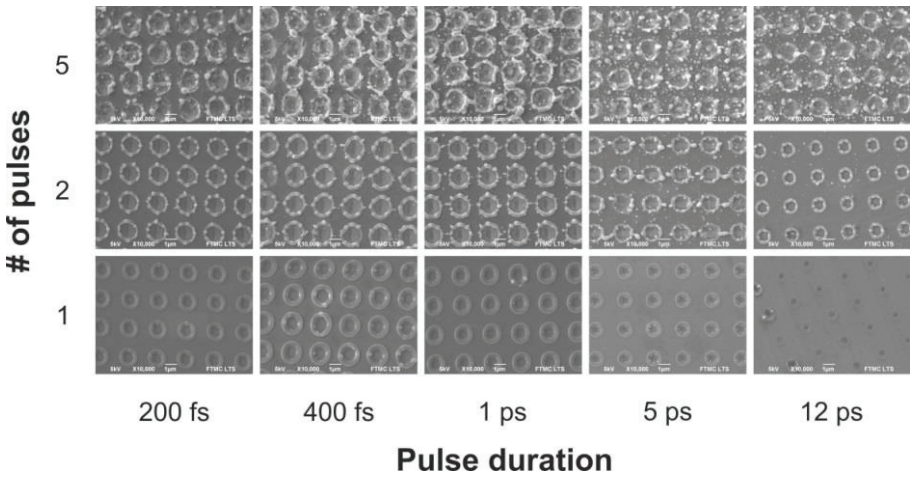

Fig. 65. SEM images of 2.5 µm period structure fabricated on crystalline silicon using DLIP with 15 mJ pulse energy and various pulse durations and pulse numbers per spot.

400 fs pulse duration provided the larger diameter of the ablated dips than 200 fs pulse, probably due to avoided energy loses due to the generation of a broad spectrum in the fused silica. There was no additional influence from the non-linear effects in the second objective to the patterning quality. However, prolonged usage of the objective in such conditions could result in the damage to the objective. Longer than 400 fs pulse durations provided reduced pattern quality due to material spallation (Fig. 65 5 pulses per spot) and smaller diameter of the dips due to the increased ablation threshold for the longer pulses.

Results presented in this chapter were obtained using fused silica objectives. Fused silica is, probably, the most widely used material for the optical components for the ultra-short laser pulses. However, usage of shorter than 400 fs laser pulses could be feasible if the different material for the objectives in the interference setup is selected. For example, calcium fluoride or magnesium fluoride glasses have lower nonlinear refractive index than fused silica [140]. Therefore, nonlinear effects in these materials should manifest at shorter pulse duration than in fused silica.

7.5 Conclusions

1. Interference patterning setup can be used to fabricate relatively large uniform pattern areas using beam shaping or beam scanning techniques.
2. The ability to modify interference intensity distribution using polarisation control technique enables tailoring of the periodical pattern for the desired application.
3. Interference patterns obtained using identical polarisation vector directions for all beams were found slightly susceptible to the shape change, dependent on the angle between the interfering beams. The most significant shape change was observed in the patterns formed by beams with non-identical polarization directions. Change in the pattern shape can be avoided if all beams are s-polarized.
4. The 4-beam interference setup induces widening of the 15 mJ energy femtosecond laser pulse from 200 fs to 400 fs due to the non-linear effects in one of the fused silica objectives. The strong non-linear effect in the objective disappeared when input pulse duration was set to 400 fs. Different optical glass materials with lower nonlinear refractive index may be used to avoid such phenomena.

List of Conclusions

1. DLIP processing using laser irradiation fluence in the interference intensity maxima below the silicon nitride ablation threshold induces periodically arranged silicon oxide/ oxy-nitride islands in the passivating silicon nitride layer.
2. Silicon oxide/ oxy-nitride islands act as a refractive grating, and it facilitates light absorption in the solar cell.
3. The efficiency of the laser processed solar cells was increased by 1±0.6%.
4. Using DLIP in the air and anisotropic wet chemical etching, the structure of periodically inverted pyramids can be fabricated in silicon. Oxidation of silicon surface due to laser irradiation is a crucial factor in the fabrication process.
5. Silicon oxide layer is formed on silicon due to the effect of laser interference irradiation. Depending on the irradiation conditions, this layer is created only at the maximum fluence regions or in the entire irradiated area including the minimum fluence regions. Certain irradiation conditions (multi-pulse regime) result in the absence of the oxide layer at the maximum fluence regions.
6. The oxide layer acts as an etching mask and positively affects the formation of inverted pyramid pattern if it is formed on the entire irradiated area except for the maximum fluence regions. A multi-pulse regime with no less than 10 pulses per spot was found to be the most suitable for the fabrication of inverted pyramid pattern.
7. A dimple structure fabricated in the multicrystalline silicon using DLIP with 300 ps laser pulses and isotropic wet chemical etching allows obtaining as low as 17.5% reflectance in the 700 – 1000 nm spectral region.

8. Various period dimple structures were fabricated in the multicrystalline silicon using DLIP with 300 ps laser pulses. Sub-micrometre dimple structures provided higher reflectance than the 1 μm or 2 μm period structures. This result can be explained by the relatively small depth of the structure (when laser fabrication parameters still allow producing orderly periodic structure) caused by the formation of melt due to the relatively long duration (300 ps) of laser pulses.
9. Experiments and numerical simulations show that femtosecond or sub-picosecond pulses are required to increase the depth of the sub-micrometre periodic structure. The depth of the 600 nm period DLIP fabricated dimple structure (maintaining the same dimple diameter) can be increased 2 times if the pulse duration is reduced from 300 ps to 300 fs.
10. Interference patterning setup can be used to fabricate relatively large uniform pattern areas using beam shaping or beam scanning techniques.
11. The ability to modify interference intensity distribution using polarisation control technique enables tailoring of the periodical pattern for the desired application.
12. Interference patterns obtained using identical polarisation vector directions for all beams were found slightly susceptible to the shape change, dependent on the angle between the interfering beams. The most significant shape change was observed in the patterns formed by beams with non-identical polarization directions. Change in the pattern shape can be avoided if all beams are s-polarized.
13. The 4-beam interference setup induces widening of the 15 mJ energy femtosecond laser pulse from 200 fs to 400 fs due to the non-linear effects in one of the fused silica objectives. The strong non-linear effect in the objective disappeared when input pulse duration was set to 400 fs. Different optical glass materials with lower nonlinear refractive index may be used to avoid such phenomena.

Summary

In this PhD thesis, application of patterning with interfering laser beams for the fabrication of light harvesting structures for the photovoltaic elements was investigated. Interference patterning technique was used to pattern antireflective silicon nitride layer on silicon solar cells and crystalline or multicrystalline silicon substrates.

Antireflective silicon nitride layer was patterned using nanosecond and picosecond laser pulses and the 2 μm period 4 beam interference intensity distribution. Using the irradiation fluence exceeding the ablation threshold, the silicon nitride layer was removed in the periodical arrangement. However, the electric characteristics of the patterned solar cell deteriorated due to laser-induced recombination centres. Using the irradiation fluence below the ablation threshold, silicon nitride was locally converted to silicon oxide/oxy-nitride. In this manner, silicon nitride/oxy-nitride grating was produced. Such grating increased absorption of the element in the 500 – 1000 nm range and resulted in the improved electric characteristics of the solar cell (efficiency increase of 1%).

Interference patterning technique combined with anisotropic wet chemical etching was used for the fabrication of the inverted pyramid pattern in crystalline silicon. The optimal irradiation conditions for the 532 and 355 nm irradiation wavelengths were determined. It was found that during the interference patterning process in the ambient air silicon oxide layer can be formed between the maximum intensity spots. Such layer acts as an etching mask and helps to produce good quality inverted pyramid pattern.

Multicrystalline silicon wafers were textured using interference patterning technique and isotropic wet chemical etching. Optimal irradiation and etching conditions were determined. Fabrication of the 2 μm period pattern resulted in as low as 17.5 % reflectance of the textures silicon substrate. Sub-micrometre patterns were also fabricated. In this case, heat diffusion in the volume between

the maximal intensity spots plays a significant role. A three-dimensional model for heat diffusion simulation was introduced. Simulations and experimental results show that good patterning quality requires femtosecond laser pulses.

In the last chapter of the thesis, improvements of the interference patterning setup are discussed. Methods to ensure large area uniform fabrication to produce plasmonic structures in thin metal films were tested experimentally. Interference patterning setup was adapted for the high-pulse-energy femtosecond laser. Means to increase interference patterning flexibility using polarisation control was investigated experimentally and using simulations. Influence of the angle between the interfering beams on the shape of the interference intensity pattern was investigated.

APPENDIX A

Laser beam reaching the surface of the material is partially reflected and partially transmitted into the material. Inside the material laser radiation is absorbed and later converted to heat. The temperature distribution in three dimensions and in time can be described by the three-dimensional heat transfer equation [141]:

$$\left[\rho C_p + L_m \delta(T - T_m) + L_v \delta(T - T_v)\right]\frac{\partial T}{\partial t} = \nabla \cdot (\kappa \nabla T) + Q \ , \tag{21}$$

where ρ is the material density, C_p is the specific heat; L_m is the latent heat of melting, L_v is the latent heat of vaporisation, T_v is the boiling point, t is time, κ is the thermal conductivity, Q is the absorbed laser power per unit volume.

Q can be defined as:

$$Q = (1 - R_\lambda)\alpha\, I(x, y, t)\exp(-\alpha z) \tag{22}$$

Where R_λ is the reflectivity, α is the absorption coefficient, $I(x,y,t)$ is the laser radiation intensity. Laser radiation intensity for 4-beam interference distribution can be defined as [142]:

$$I(x, y, t) = \frac{1}{\tau_p} \cdot rect(t - t_p) \cdot \frac{4 \cdot 2 \cdot E_p}{\pi w_0^{\,2}} \left[\cos^2\left(\frac{\pi(x - y)}{2\Lambda_4}\right) + \cos^2\left(\frac{\pi(x + y)}{2\Lambda_4}\right) - 1 \right]^2 , \tag{23}$$

where τ_p is laser pulse duration, E_p is the laser pulse energy, w_0 is the interference spot size radius, Λ_4 is the 4-beam interference intensity distribution period.

The terms $L_{\mathrm{m,v}}\delta(T\text{-}T_{\mathrm{m,v}})$ allow simulation of the solid-liquid and liquid-vapour interfaces. The δ function was approximated by [141]:

$$\delta(T - T_{m,v}, \Delta_{m,v}) = \frac{1}{\sqrt{2\pi}\Delta_{m,v}} \exp\left(- \frac{(T - T_{m,v})^2}{2\Delta_{m,v}^{\,2}} \right) , \tag{24}$$

where the parameter Δ is in the range of 100–200 K depending on the temperature gradient.

Silicon properties and computation parameters used in the simulation are given in Table 5.

Table 5. Silicon material parameters [143, 144] and simulation parameters.

Parameter	Quantity	Unit
ρ	$\rho(T) = \begin{cases} 2.311\cdot10^{3} - 2.63\cdot10^{-2}\left(T - T_m\right); & T \le T_m \\ 2.580\cdot10^{3} - 0.171\left(T - T_m\right) - 1.61\cdot10^{-2}\left(T - T_m\right)^2; & T > T_m \end{cases}$	kg/m^3
C_p	$C_p(T) = \begin{cases} \left(\frac{10^6}{\rho(T)}\right)\left(1.4743 + \frac{0.17066\cdot T}{300}\right); & T \le T_m \\ \frac{2.432\cdot10^6}{\rho(T)}; & T > T_m \end{cases}$	J/(kg·K)
L_m	$1.79\cdot10^6$	J/Kg
T_m	1687	K
L_v	$1.28\cdot10^7$	J/Kg
T_v	3538	K
κ	$\kappa(T) = \frac{29900}{T-99}$	W/(m·K)
R_λ	$R_\lambda(T) = \begin{cases} 0.367 + 429\cdot10^{-5}\cdot T + 2.691\cdot10^{-15}\cdot T^4; & T \le 3019\ \mathrm{K} \\ 0.72; & T > 3019\ \mathrm{K} \end{cases}$	–
α	$1.2233\cdot10^6$	m^{-1}
τ_p	0.3; 300; $35\cdot10^3$	ps
E_p	2	mJ
w_0	250	μm
Λ_4	600	nm
Δ_m	100	K
Δ_v	200	K

APPENDIX B

A Gaussian beam at its waist can be approximated as a plane wave:

$$E_G = E_0 e^{i(\mathbf{kr}-\varpi t)}, \tag{25}$$

Where E_0 is the electric field amplitude, t is time, and ϖ is the optical angular frequency. The intensity of such wave is proportional to ${E_0}^2$.

If this wave is divided into two waves with equal intensities I_1 and I_2, their electric field amplitudes E_1 and E_2 are:

$$\begin{aligned} &I_{1,2} \cong \tfrac{1}{2}{E_0}^2; \\ &E_{1,2} = \tfrac{1}{\sqrt{2}} E_0. \end{aligned} \tag{26}$$

Then, if these two waves interfere, the resulting intensity is:

$$I_{II} \cong \left| \tfrac{1}{\sqrt{2}}{E_0}^2 e^{i(\mathbf{k}_1\mathbf{r}-\varpi t)} + \tfrac{1}{\sqrt{2}}{E_0}^2 e^{i(\mathbf{k}_2\mathbf{r}-\varpi t)} \right|^2 = {E_0}^2 + {E_0}^2 \cos\left((\mathbf{k}_1 - \mathbf{k}_2)\mathbf{r}\right). \tag{27}$$

The intensity in the peak of the interference band is two times greater than in the initial plane wave (or peak of the Gaussian beam). Similarly, it can be shown, that if the initial wave is divided into three and then these three waves interfere, the resulting intensity is:

$$\begin{aligned} &I_{II} \cong \left| \tfrac{1}{\sqrt{3}}{E_0}^2 e^{i(\mathbf{k}_1\mathbf{r}-\varpi t)} + \tfrac{1}{\sqrt{3}}{E_0}^2 e^{i(\mathbf{k}_2\mathbf{r}-\varpi t)} + \tfrac{1}{\sqrt{3}}{E_0}^2 e^{i(\mathbf{k}_3\mathbf{r}-\varpi t)} \right|^2 = \\ &= {E_0}^2 + \tfrac{2}{3}{E_0}^2 \cos\left((\mathbf{k}_1 - \mathbf{k}_2)\mathbf{r}\right) + \tfrac{2}{3}{E_0}^2 \cos\left((\mathbf{k}_1 - \mathbf{k}_3)\mathbf{r}\right) + \tfrac{2}{3}{E_0}^2 \cos\left((\mathbf{k}_2 - \mathbf{k}_3)\mathbf{r}\right). \end{aligned} \tag{28}$$

The intensity in the interference peak will be 3 times greater than in the initial plane wave (or peak of the Gaussian beam).

Peak fluence and peak intensity are linearly related. Therefore, peak fluence of the laser beam, modulated due to the interference, may be calculated using the well-known formula for the peak fluence, multiplied by the number of interfering beams N:

$$F_0 = N \frac{2E_p}{\pi {\omega_0}^2} \tag{29}$$

REFERENCES

[1]. G. Gomard, R. Peretti, E. Drouard, X. Meng and C. Seassal, Photonic crystals and optical mode engineering for thin film photovoltaics. *Opt. Express* **21**, A515-A527 (2013).

[2]. K. S. Cho, P. Mandal, K. Kim, et al., Improved efficiency in GaAs solar cells by 1D and 2D nanopatterns fabricated by laser interference lithography. *Opt. Commun.* **284**, 2608-2612 (2011).

[3]. N. Wang, Y. Zhu, W. Wei, J. Chen, P. Li and Y. Wen, Conversion efficiency enhanced photovoltaic device with nanohole arrays in antireflection coating layer. *Opt. Commun.* **284**, 4773-4777 (2011).

[4]. H. A. Atwater and A. Polman, Plasmonics for improved photovoltaic devices. *Nat Mater* **9**, 205-213 (2010).

[5]. P. Spinelli, V. E. Ferry, J. van de Groep, et al., Plasmonic light trapping in thin-film Si solar cells. *J. Opt.* **14**, 024002 (2012).

[6]. H. Sai, T. Matsui, K. Matsubara, M. Kondo and I. Yoshida, 11.0%-Efficient Thin-Film Microcrystalline Silicon Solar Cells with Honeycomb Textured Substrates. *IEEE J. Photovolt.* **4**, 1349-1353 (2014).

[7]. L. Müller-Meskamp, Y. H. Kim, T. Roch, et al., Efficiency Enhancement of Organic Solar Cells by Fabricating Periodic Surface Textures using Direct Laser Interference Patterning. *Adv. Mater.* **24**, 906-910 (2012).

[8]. Y. Nakata, Interference laser processing. *Advanced Optical Technologies* **5**, 29-38 (2016).

[9]. EIA International Energy Outlook 2016 (DOE/EIA-0484(2016)). Retrieved from U.S. Energy Information Administration website: https://www.eia.gov/outlooks/ieo/pdf/0484(2016).pdf (2016).

[10]. RENEWABLES 2016 GLOBAL STATUS REPORT. Retrieved from Renewable Energy Policy Network for the 21st Century (REN21) website: http://www.ren21.net/wp-content/uploads/2016/06/GSR_2016_Full_Report.pdf (2016).

[11]. Why We Need More Solar Companies to Fail. (August 09, 2017). Retrieved from: https://www.technologyreview.com/s/512516/why-we-need-more-solar-companies-to-fail/.

[12]. THE POWER TO CHANGE: SOLAR AND WIND COST REDUCTION POTENTIAL TO 2025. Retrieved from International Renewable Energy Agency (IRENA) website: http://www.irena.org/DocumentDownloads/Publications/IRENA_Power_to_Change_2016.pdf (2016).

[13]. Overcapacity: How low can module prices go? (August 09, 2017). Retrieved from: https://www.pv-tech.org/editors-blog/overcapacity-how-low-can-module-prices-go.

[14]. A. Smets, K. Jäger, O. Isabella, M. Zeman and R. van Swaaij, *Solar Energy: The Physics and Engineering of Photovoltaic Conversion, Technologies and Systems.* (UIT Cambridge, 2016).

[15]. A. McEvoy, L. Castaner and T. Markvart, *Solar Cells: Materials, Manufacture and Operation.* (Elsevier Science, 2012).
[16]. L. M. Fraas and L. D. Partain, *Solar Cells and Their Applications.* (Wiley, 2010).
[17]. A. Cuevas, The Recombination Parameter J0. *Energy Procedia* **55**, 53-62 (2014).
[18]. A. G. Aberle, Surface passivation of crystalline silicon solar cells: a review. *Prog. Photovoltaics Res. Appl.* **8**, 473-487 (2000).
[19]. K. R. McIntosh and L. P. Johnson, Recombination at textured silicon surfaces passivated with silicon dioxide. *J. Appl. Phys.* **105**, 124520 (2009).
[20]. R. M. Swanson, Approaching the 29% limit efficiency of silicon solar cells. *Conference Record of the Thirty-first IEEE Photovoltaic Specialists Conference*, 889-894 (2005).
[21]. K. Yoshikawa, H. Kawasaki, W. Yoshida, et al., Silicon heterojunction solar cell with interdigitated back contacts for a photoconversion efficiency over 26%. *Nat. Energy.* **2**, 17032 (2017).
[22]. A. Reinders, P. Verlinden, A. Freundlich and W. van Sark, *Photovoltaic Solar Energy: From Fundamentals to Applications.* (Wiley, 2017).
[23]. Maximizing cell performance how REC's use of Passivated Emitter Rear Cell technology improves the capture of light and optimizes cell performance. Retrieved from Renewable Energy Corporation (REC) website: http://www.recgroup.com/sites/default/files/documents/whitepaper_perc.pdf (2014).
[24]. S. De Wolf, A. Descoeudres, C. Holman Zachary and C. Ballif, High-efficiency Silicon Heterojunction Solar Cells: A Review. *Green* **2**, 7 (2012).
[25]. K. Masuko, M. Shigematsu, T. Hashiguchi, et al., Achievement of More Than 25% Conversion Efficiency With Crystalline Silicon Heterojunction Solar Cell. *IEEE J. Photovolt.* **4**, 1433-1435 (2014).
[26]. J. Gjessing, A. S. Sudbø and E. S. Marstein, Comparison of periodic light-trapping structures in thin crystalline silicon solar cells. *J. Appl. Phys.* **110**, 033104 (2011).
[27]. T. Tiedje, E. Yablonovitch, G. D. Cody and B. G. Brooks, Limiting efficiency of silicon solar cells. *IEEE Trans. Electron Devices* **31**, 711-716 (1984).
[28]. A. Shah, *Thin-Film Silicon Solar Cells.* (EFPL Press, 2010).
[29]. T. Matsui, H. Sai, K. Saito and M. Kondo, High-efficiency thin-film silicon solar cells with improved light-soaking stability. *Prog. Photovoltaics Res. Appl.* **21**, 1363-1369 (2013).
[30]. M. A. Green, A. Ho-Baillie and H. J. Snaith, The emergence of perovskite solar cells. *Nat Photon* **8**, 506-514 (2014).

[31]. J. H. Noh, S. H. Im, J. H. Heo, T. N. Mandal and S. I. Seok, Chemical Management for Colorful, Efficient, and Stable Inorganic-Organic Hybrid Nanostructured Solar Cells. *Nano Lett.* **13**, 1764-1769 (2013).
[32]. J. Werner, C.-H. Weng, A. Walter, et al., Efficient Monolithic Perovskite/Silicon Tandem Solar Cell with Cell Area >1 cm^2. *J. Phys. Chem. Lett.* **7**, 161-166 (2016).
[33]. M. A. Green, K. Emery, Y. Hishikawa, W. Warta and E. D. Dunlop, Solar cell efficiency tables (Version 45). *Prog. Photovoltaics Res. Appl.* **23**, 1-9 (2015).
[34]. P. Jackson, R. Wuerz, D. Hariskos, E. Lotter, W. Witte and M. Powalla, Effects of heavy alkali elements in $Cu(In,Ga)Se_2$ solar cells with efficiencies up to 22.6%. *Phys. Status Solidi Rapid Res. Lett.* **10**, 583-586 (2016).
[35]. T. Feurer, P. Reinhard, E. Avancini, et al., Progress in thin-film CIGS photovoltaics – Research and development, manufacturing, and applications. *Prog. Photovoltaics Res. Appl.* **25**, 645-667 (2017).
[36]. S. Saeed, E. M. de Jong, K. Dohnalova and T. Gregorkiewicz, Efficient optical extraction of hot-carrier energy. *Nat. Commun.* **5**, 4665 (2014).
[37]. P. D. Paulson, R. W. Birkmire and W. N. Shafarman, Optical characterization of $CuIn_{1-x}Ga_xSe_2$ alloy thin films by spectroscopic ellipsometry. *J. Appl. Phys.* **94**, 879-888 (2003).
[38]. M. A. Green, Self-consistent optical parameters of intrinsic silicon at 300K including temperature coefficients. *Sol. Energy Mater. Sol. Cells* **92**, 1305-1310 (2008).
[39]. E. D. Palik, *Handbook of Optical Constants of Solids.* (Academic Press, Boston, 1985).
[40]. D. E. Aspnes, S. M. Kelso, R. A. Logan and R. Bhat, Optical properties of AlxGa1−x As. *J. Appl. Phys.* **60**, 754-767 (1986).
[41]. D. T. F. Marple, Refractive Index of ZnSe, ZnTe, and CdTe. *J. Appl. Phys.* **35**, 539-542 (1964).
[42]. A. M. A. Leguy, Y. Hu, M. Campoy-Quiles, et al., Reversible Hydration of $CH_3NH_3PbI_3$ in Films, Single Crystals, and Solar Cells. *Chem. Mater.* **27**, 3397-3407 (2015).
[43]. R. B. Wehrspohn, U. Rau and A. Gombert, *Photon Management in Solar Cells.* (Wiley, 2015).
[44]. K.-S. Han, J.-H. Shin, W.-Y. Yoon and H. Lee, Enhanced performance of solar cells with anti-reflection layer fabricated by nano-imprint lithography. *Sol. Energy Mater. Sol. Cells* **95**, 288-291 (2011).
[45]. H. K. Raut, S. S. Dinachali, Y. C. Loke, et al., Multiscale ommatidial arrays with broadband and omnidirectional antireflection and antifogging properties by sacrificial layer mediated nanoimprinting. *ACS Nano* **9**, 1305-14 (2015).

[46]. P. Campbell and M. A. Green, Light trapping properties of pyramidally textured surfaces. *J. Appl. Phys.* **62**, 243 (1987).
[47]. Y. Fan, P. Han, P. Liang, Y. Xing, Z. Ye and S. Hu, Differences in etching characteristics of TMAH and KOH on preparing inverted pyramids for silicon solar cells. *Appl. Surf. Sci.* **264**, 761-766 (2013).
[48]. E. Vazsonyi, K. De Clercq, R. Einhaus, et al., Improved anisotropic etching process for industrial texturing of silicon solar cells. *Sol. Energy Mater. Sol. Cells* **57**, 179-188 (1999).
[49]. S.-Y. Lien, Y.-S. Cho, Y. Shao, et al., Influence of Surface Morphology on the Effective Lifetime and Performance of Silicon Heterojunction Solar Cell. *Int. J. Photoenergy* **2015**, 1-8 (2015).
[50]. J. Zhao, A. Wang, M. A. Green and F. Ferrazza, 19.8% efficient "honeycomb" textured multicrystalline and 24.4% monocrystalline silicon solar cells. *Appl. Phys. Lett.* **73**, 1991-1993 (1998).
[51]. S. C. Baker-Finch and K. R. McIntosh, Reflection of normally incident light from silicon solar cells with pyramidal texture. *Prog. Photovoltaics Res. Appl.* **19**, 406-416 (2011).
[52]. D. H. Macdonald, A. Cuevas, M. J. Kerr, C. Samundsett, D. Ruby, S. Winderbaum and A. Leo, Texturing industrial multicrystalline silicon solar cells. *Sol. Energy* **76**, 277-283 (2004).
[53]. R. Einhaus, E. Vazsonyi, J. Szlufcik, J. Nijs and R. Mertens, Isotropic texturing of multicrystalline silicon wafers with acidic texturing solutions. *Conference Record of the Twenty-Sixth IEEE Photovoltaic Specialists Conference*, 167-170 (1997).
[54]. U. Gangopadhyay, S. K. Dhungel, K. Kim, et al., Novel low cost chemical texturing for very large area industrial multi-crystalline silicon solar cells. *Semicond. Sci. Technol.* **20**, 938 (2005).
[55]. J.-M. Shim, H.-W. Lee, K.-Y. Cho, et al., 17.6% Conversion Efficiency Multicrystalline Silicon Solar Cells Using the Reactive Ion Etching with the Damage Removal Etching. *Int. J. Photoenergy* **2012**, 6 (2012).
[56]. B. M. Damiani, R. Ludemann, D. S. Ruby, S. H. Zaidi and A. Rohatgi, Development of RIE-textured silicon solar cells. *Conference Record of the Twenty-Eighth IEEE Photovoltaic Specialists Conference*, 371-374 (2000).
[57]. L. Dobrzañski, A. Drygta, P. Panek, M. Lipiñski and P. Ziêba, Development of the laser method of multicrystalline silicon surface texturization. *Arch. Mater. Sci. Eng.* **38**, 5-11 (2009).
[58]. K.-R. Kim, T.-H. Kim, H.-A. Park, S.-Y. Kim, S.-H. Cho, J. Yi and B.-D. Choi, UV laser direct texturing for high efficiency multicrystalline silicon solar cell. *Appl. Surf. Sci.* **264**, 404-409 (2013).
[59]. M. David, F. Takashi and M. Hiroyuki, Determination of Minority-Carrier Lifetime in Multicrystalline Silicon Solar Cells using Current Transient Behaviors. *Jpn. J. Appl. Phys.* **38**, 1408 (1999).

[60]. S. E. Han, A. Mavrokefalos, M. S. Branham and G. Chen, Efficient light-trapping nanostructures in thin silicon solar cells. *Proc. SPIE 8031, Micro- and Nanotechnology Sensors, Systems, and Applications III*, 80310T (2011).
[61]. S. Fonash, *Introduction to Light Trapping in Solar Cell and Photo-detector Devices.* (Elsevier Science, 2014).
[62]. Z. Yu, A. Raman and S. Fan, Fundamental limit of nanophotonic light trapping in solar cells. *Proc. Nat. Acad. Sci. U.S.A.* **107**, 17491-17496 (2010).
[63]. X. Liu, P. R. Coxon, M. Peters, B. Hoex, J. M. Cole and D. J. Fray, Black silicon: fabrication methods, properties and solar energy applications. *Energy Environ. Sci.* **7**, 3223-3263 (2014).
[64]. O. Martin, A. Michael, B. Howard, et al., Black Silicon Photovoltaics. *Adv. Opt. Mater.* **3**, 147-164 (2015).
[65]. H. Savin, P. Repo, G. von Gastrow, P. Ortega, E. Calle, M. Garín and R. Alcubilla, Black silicon solar cells with interdigitated back-contacts achieve 22.1% efficiency. *Nat. Nanotechnol.* **10**, 624 (2015).
[66]. G. Gomard, R. Peretti, S. Callard, et al., Blue light absorption enhancement based on vertically channelling modes in nano-holes arrays. *Appl. Phys. Lett.* **104**, 051119 (2014).
[67]. K. X. Wang, Z. Yu, V. Liu, Y. Cui and S. Fan, Absorption Enhancement in Ultrathin Crystalline Silicon Solar Cells with Antireflection and Light-Trapping Nanocone Gratings. *Nano Lett.* **12**, 1616-1619 (2012).
[68]. X. Chen, B. Jia, J. K. Saha, et al., Broadband enhancement in thin-film amorphous silicon solar cells enabled by nucleated silver nanoparticles. *Nano Lett* **12**, 2187-92 (2012).
[69]. R. A. Pala, J. S. Q. Liu, E. S. Barnard, D. Askarov, E. C. Garnett, S. Fan and M. L. Brongersma, Optimization of non-periodic plasmonic light-trapping layers for thin-film solar cells. *Nat. Commun.* **4**, 2095 (2013).
[70]. Y. Nishijima, L. Rosa and S. Juodkazis, Surface plasmon resonances in periodic and random patterns of gold nano-disks for broadband light harvesting. *Opt. Express* **20**, 11466-11477 (2012).
[71]. P. Spinelli, M. Hebbink, R. de Waele, L. Black, F. Lenzmann and A. Polman, Optical Impedance Matching Using Coupled Plasmonic Nanoparticle Arrays. *Nano Lett.* **11**, 1760-1765 (2011).
[72]. Y. A. Akimov, W. S. Koh, S. Y. Sian and S. Ren, Nanoparticle-enhanced thin film solar cells: Metallic or dielectric nanoparticles? *Appl. Phys. Lett.* **96**, 073111 (2010).
[73]. Y. A. Akimov, W. S. Koh and K. Ostrikov, Enhancement of optical absorption in thin-film solar cells through the excitation of higher-order nanoparticle plasmon modes. *Opt. Express* **17**, 10195-10205 (2009).
[74]. S. Seal, V. Budhraja, L. Ji and V. V. Varadan, Enhanced Light Trapping in Thin Film Solar Cells Using a Plasmonic Fishnet Structure. *Int. J. Photoenergy* **2015**, 8 (2015).

[75]. N. Healy, S. Mailis, N. M. Bulgakova, et al., Extreme electronic bandgap modification in laser-crystallized silicon optical fibres. *Nat Mater* **13**, 1122-7 (2014).
[76]. A. Rämer, O. Osmani and B. Rethfeld, Laser damage in silicon: Energy absorption, relaxation, and transport. *J. Appl. Phys.* **116**, 053508 (2014).
[77]. E. J. Yoffa, Dynamics of dense laser-induced plasmas. *Phys. Rev. B* **21**, 2415-2425 (1980).
[78]. J. R. Goldman and J. A. Prybyla, Ultrafast dynamics of laser-excited electron distributions in silicon. *Phys Rev Lett* **72**, 1364-1367 (1994).
[79]. T. Sjodin, H. Petek and H.-L. Dai, Ultrafast Carrier Dynamics in Silicon: A Two-Color Transient Reflection Grating Study on a (111) Surface. *Phys. Rev. Lett.* **81**, 5664-5667 (1998).
[80]. S. Jeong, H. Zacharias and J. Bokor, Ultrafast carrier dynamics on the Si(100)2×1 surface. *Phys. Rev. B* **54**, R17300-R17303 (1996).
[81]. J. Bonse, S. Baudach, J. Krüger, W. Kautek and M. Lenzner, Femtosecond laser ablation of silicon-modification thresholds and morphology. *Appl. Phys. A* **74**, 19-25 (2002).
[82]. B. N. Chichkov, C. Momma, S. Nolte, F. Alvensleben and A. Tünnermann, Femtosecond, picosecond and nanosecond laser ablation of solids. *Appl. Phys. A* **63**, 109-115 (1996).
[83]. B. Neuenschwander, G. F. Bucher, C. Nussbaum, B. Joss, M. Muralt, U. W. Hunziker and P. Schuetz, Processing of metals and dielectric materials with ps-laser pulses: results, strategies, limitations and needs. *Proc. SPIE 7584, Laser Applications in Microelectronic and Optoelectronic Manufacturing XV*, 75840R (2010).
[84]. B. Neuenschwander, B. Jaeggi, M. Zimmermann, et al., Laser surface structuring with 100 W of average power and sub-ps pulses. *J. Laser Appl.* **28**, 022506 (2016).
[85]. F. Bauer, A. Michalowski, T. Kiedrowski and S. Nolte, Heat accumulation in ultra-short pulsed scanning laser ablation of metals. *Opt. Express* **23**, 1035-1043 (2015).
[86]. A. Lasagni, T. Roch, M. Bieda, D. Benke and E. Beyer, High speed surface functionalization using direct laser interference patterning, towards 1 m^2/min fabrication speed with sub-μm resolution. *Proc. SPIE 8968, Laser-based Micro- and Nanoprocessing VIII*, 89680A (2014).
[87]. B. Yang and M. Lee, Fabrication of honeycomb texture on poly-Si by laser interference and chemical etching. *Appl. Surf. Sci.* **284**, 565-568 (2013).
[88]. Y. Nakata, K. Murakawa, N. Miyanaga and K. Momoo, Interfering Ultraviolet Femtosecond Laser Processing of Gold Thin Film and Prospect of Shortest Period. *Appl. Phys. Express* **5**, 102703 (2012).
[89]. A. Lasagni, C. Holzapfel, T. Weirich and F. Mücklich, Laser interference metallurgy: A new method for periodic surface microstructure

design on multilayered metallic thin films. *Appl. Surf. Sci.* **253**, 8070-8074 (2007).
[90]. F. Beinhorn, J. Ihlemann, P. Simon, et al., Sub-micron grating formation in Ta2O5-waveguides by femtosecond UV-laser ablation. *Appl. Surf. Sci.* **138**, 107-110 (1999).
[91]. B. Bläsi, H. Hauser, O. Höhn, V. Kübler, M. Peters and A. J. Wolf, Photon Management Structures Originated by Interference Lithography. *Energy Procedia* **8**, 712-718 (2011).
[92]. H. Misawa, T. Kondo, S. Juodkazis, V. Mizeikis and S. Matsuo, Holographic lithography of periodic two- and three-dimensional microstructures in photoresist SU-8. *Opt. Express* **14**, 7943 (2006).
[93]. L. Z. Cai, X. L. Yang and Y. R. Wang, All fourteen Bravais lattices can be formed by interference of four noncoplanar beams. *Opt. Lett.* **27**, 900-902 (2002).
[94]. S. Indrišiūnas, B. Voisiat, M. Gedvilas and G. Račiukaitis, Two complementary ways of thin-metal-film patterning using laser beam interference and direct ablation. *J. Micromech. Microeng.* **23**, 095034 (2013).
[95]. Y. Nakata, K. Murakawa, K. Sonoda, K. Momoo and N. Miyanaga, Design of interference using coherent beams configured as a six-sided pyramid. *Appl. Opt.* **51**, 5004-5010 (2012).
[96]. M. Ellman, A. Rodríguez, N. Pérez, et al., High-power laser interference lithography process on photoresist: Effect of laser fluence and polarisation. *Appl. Surf. Sci.* **255**, 5537-5541 (2009).
[97]. S. Beckemper, J. Huang, A. Gillner and K. Wang, Generation of Periodic Micro- and Nano-structures by Parameter-Controlled Three-beam Laser Interference Technique. *J. Laser Micro/Nanoeng.* **6**, 49-53 (2011).
[98]. J. L. Stay, G. M. Burrow and T. K. Gaylord, Three-beam interference lithography methodology. *Rev. Sci. Instrum.* **82**, 023115 (2011).
[99]. B. Johannes de, G. Nadine, V. W. Jörg, G. Ulrich and S. Volker, Sub-100 nm silicon nanowires by laser interference lithography and metal-assisted etching. *Nanotechnology* **21**, 095302 (2010).
[100]. A. A. Maznev, T. F. Crimmins and K. A. Nelson, How to make femtosecond pulses overlap. *Opt. Lett.* **23**, 1378-1380 (1998).
[101]. T. Roch, D. Benke and A. F. Lasagni, Method and arrangement for forming a structuring on surfaces of components by means of a laser beam, Fraunhofer Gesellschaft zur Forderung der Angewandten Forschung, (US9764424B2, 2017)
[102]. H. C. Guo, D. Nau, A. Radke, et al., Large-area metallic photonic crystal fabrication with interference lithography and dry etching. *Applied Physics B* **81**, 271-275 (2005).
[103]. J. de Boor, N. Geyer, U. Gösele and V. Schmidt, Three-beam interference lithography: upgrading a Lloyd's interferometer for single-exposure hexagonal patterning. *Opt. Lett.* **34**, 1783-1785 (2009).

[104]. B. Voisiat (2015). Formation of Frequency Selective Surfaces Using Laser Ablation Methods and Characterisation of Their Properties (Doctoral dissertation).
[105]. E. Stankevicius, T. Gertus, M. Rutkauskas, et al., Fabrication of micro-tube arrays in photopolymer SZ2080 by using three different methods of a direct laser polymerization technique. *J. Micromech. Microeng.* **22**, 065022 (2012).
[106]. Y. Nakata, K. Murakawa, K. Sonoda, K. Momoo, N. Miyanaga and T. Hiromoto, Designing of interference pattern in ultra-short pulse laser processing. *Appl. Phys. A* **112**, 191-196 (2013).
[107]. A. Fernandez and D. W. Phillion, Effects of phase shifts on four-beam interference patterns. *Appl. Opt.* **37**, 473-478 (1998).
[108]. B. Voisiat, M. Gedvilas, S. Indrišiūnas and G. Račiukaitis, Picosecond-Laser 4-Beam-Interference Ablation as a Flexible Tool for Thin Film Microstructuring. *Phys. Proc.* **12**, 116-124 (2011).
[109]. Y. Yang, Q. Li and G. P. Wang, Design and fabrication of diverse metamaterial structures by holographic lithography. *Opt. Express* **16**, 11275-11280 (2008).
[110]. D. Wang, Z. Wang, Z. Zhang, Y. Yue, D. Li and C. Maple, Effects of polarization on four-beam laser interference lithography. *Appl. Phys. Lett.* **102**, 081903 (2013).
[111]. H. Jintang, B. Stefan, G. Arnold and W. Keyi, Tunable surface texturing by polarization-controlled three-beam interference. *J. Micromech. Microeng.* **20**, 095004 (2010).
[112]. J. Xu, Z. Wang, Z. Zhang, D. Wang and Z. Weng, Fabrication of moth-eye structures on silicon by direct six-beam laser interference lithography. *J. Appl. Phys.* **115**, 203101 (2014).
[113]. X. Zhu, C. Vannahme, E. Højlund-Nielsen, N. A. Mortensen and A. Kristensen, Plasmonic colour laser printing. *Nat Nano* **11**, 325-329 (2016).
[114]. M. Weiler, S. B. Quint, S. Klenk and C. Pacholski, Bottom-up fabrication of nanohole arrays loaded with gold nanoparticles: extraordinary plasmonic sensors. *Chem. Commun.* **50**, 15419-15422 (2014).
[115]. S. Indrišiūnas, B. Voisiat, M. Gedvilas and G. Račiukaitis, New opportunities for custom-shape patterning using polarization control in confocal laser beam interference setup. *J. Laser Appl.* **29**, 011501 (2017).
[116]. L. Z. Cai, X. L. Yang and Y. R. Wang, Interference of three noncoplanar beams: patterns, contrast and polarization optimization. *J. Mod. Opt.* **49**, 1663-1672 (2002).
[117]. H. M. Su, Y. C. Zhong, X. Wang, X. G. Zheng, J. F. Xu and H. Z. Wang, Effects of polarization on laser holography for microstructure fabrication. *Phys. Rev. E* **67**, 056619 (2003).
[118]. http://www.spectroscopyonline.com/characterization-amorphous-and-microcrystalline-silicon-using-raman-spectroscopy?id=&sk=&date=&%0A%09%09%09&pageID=2.

[119]. J. M. Liu, Simple technique for measurements of pulsed Gaussian-beam spot sizes. *Opt. Lett.* **7**, 196-8 (1982).
[120]. L. V. Mercaldo, E. M. Esposito, P. D. Veneri, G. Fameli, S. Mirabella and G. Nicotra, First and second-order Raman scattering in Si nanostructures within silicon nitride. *Appl. Phys. Lett.* **97**, 153112 (2010).
[121]. J. Etchepare, M. Merian and L. Smetankine, Vibrational normal modes of SiO_2. I. α and β quartz. *J. Chem. Phys.* **60**, 1873-1876 (1974).
[122]. H. G. Hecht, The Interpretation of Diffuse Reflectance Spectra. *J. Res. Natl. Bur. Stand., Sect. A* **80A**, 567-583 (1976).
[123]. W. Pfleging, A. Ludwig, K. Seemann, R. Preu, H. Mäckel and S. W. Glunz, Laser micromachining for applications in thin film technology. *Appl. Surf. Sci.* **154–155**, 633-639 (2000).
[124]. C. S. Neckermann K, Andrä G, Bähr M, Lossen J, Ose E, Local structuring of dielectric layers on silicon for improved solar cell metallization. *Proceedings of the 22th European photovoltaic solar energy conference*, (2007).
[125]. J. Zhao, A. Wang, P. Altermatt and M. A. Green, Twenty‐four percent efficient silicon solar cells with double layer antireflection coatings and reduced resistance loss. *Appl. Phys. Lett.* **66**, 3636-3638 (1995).
[126]. B. Yang and M. Lee, Laser interference-driven fabrication of regular inverted-pyramid texture on mono-crystalline Si. *Microelectron. Eng.* **130**, 52-56 (2014).
[127]. J.-W. Lin, E.-T. Liu, C.-H. Wu, I.-J. Hsieh and T.-S. Chao, Formation of Inverted-Pyramid Structure by Modifying Laser Processing Parameters and Acid Etching Time. *ECS Trans.* **35**, 67-72 (2011).
[128]. A. Kiani, K. Venkatakrishnan and B. Tan, Micro/nano scale amorphization of silicon by femtosecond laser irradiation. *Opt. Express* **17**, 16518-16526 (2009).
[129]. F. Micheli and I. W. Boyd, Photon-controlled oxidation of silicon. *Appl. Phys. Lett.* **51**, 1149-1151 (1987).
[130]. H. Seidel, L. Csepregi, A. Heuberger and H. Baumgärtel, Anisotropic Etching of Crystalline Silicon in Alkaline Solutions: I . Orientation Dependence and Behavior of Passivation Layers. *J. Electrochem. Soc.* **137**, 3612-3626 (1990).
[131]. K. Noritaka, M. Noboru, Y. Shigeru, T. Noboru, O. Tatsuo and A. Kiwamu, Etch stop of silicon surface induced by tribo-nanolithography. *Nanotechnology* **16**, 1411-1414 (2005).
[132]. J. Bonse, K. W. Brzezinka and A. J. Meixner, Modifying single-crystalline silicon by femtosecond laser pulses: an analysis by micro Raman spectroscopy, scanning laser microscopy and atomic force microscopy. *Appl. Surf. Sci.* **221**, 215-230 (2004).
[133]. *Plasmonics From Basics to Advanced Topics.* (Springer-Verlag Berlin Heidelberg, 2012).

[134]. T. Tavera, N. Pérez, A. Rodríguez, P. Yurrita, S. M. Olaizola and E. Castaño, Periodic patterning of silicon by direct nanosecond laser interference ablation. *Appl. Surf. Sci.* **258**, 1175-1180 (2011).
[135]. S. Zhang, W. Fan, N. Panoiu, K. Malloy, R. Osgood and S. Brueck, Experimental Demonstration of Near-Infrared Negative-Index Metamaterials. *Phys. Rev. Lett.* **95**, (2005).
[136]. J. Henzie, J. Lee, M. H. Lee, W. Hasan and T. W. Odom, Nanofabrication of plasmonic structures. *Annu Rev Phys Chem* **60**, 147-165 (2009).
[137]. G. Vecchi, V. Giannini and J. Gomez Rivas, Shaping the fluorescent emission by lattice resonances in plasmonic crystals of nanoantennas. *Phys Rev Lett* **102**, 146807 (2009).
[138]. A. Laskin and V. Laskin, Collimating beam shaper for holography and interferometry. *Proc. SPIE 8644, Practical Holography XXVII: Materials and Applications*, 864406 (2013).
[139]. H. F. Ghaemi, T. Thio, D. E. Grupp, T. W. Ebbesen and H. J. Lezec, Surface plasmons enhance optical transmission through subwavelength holes. *Phys. Rev. B* **58**, 6779-6782 (1998).
[140]. R. Adair, L. L. Chase and S. A. Payne, Nonlinear refractive index of optical crystals. *Phys. Rev. B* **39**, 3337-3350 (1989).
[141]. N. M. Bulgakova, A. V. Bulgakov and L. P. Babich, Energy balance of pulsed laser ablation: thermal model revised. *Appl. Phys. A* **79**, 1323-1326 (2004).
[142]. M. Gedvilas, B. Voisiat, S. Indrišiūnas, et al., Thermo-chemical microstructuring of thin metal films using multi-beam interference by short (nano- & picosecond) laser pulses. *Thin Solid Films* **634**, 134-140 (2017).
[143]. D. E. Aspnes and A. A. Studna, Dielectric functions and optical parameters of Si, Ge, GaP, GaAs, GaSb, InP, InAs, and InSb from 1.5 to 6.0 eV. *Phys. Rev. B* **27**, 985-1009 (1983).
[144]. V. Tangwarodomnukun, J. Wang, C. Z. Huang and H. T. Zhu, Heating and material removal process in hybrid laser-waterjet ablation of silicon substrates. *Int. J. Mach. Tools Manuf* **79**, 1-16 (2014).